The Association of Sigmoidal Features and Transequatorial Interconnecting Loops with Eruptive Solar Activity.

Alexandra Hannah Glover

Mullard Space Science Laboratory
Department of Space and Climate Physics
University College London

A thesis submitted to the University of London
for the degree of Doctor of Philosophy.

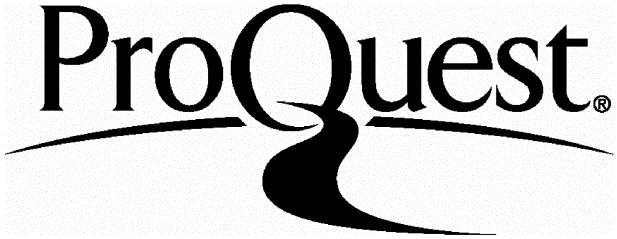

Abstract

This thesis examines sigmoidal solar X-ray features and transequatorial-interconnecting loops. Recent studies have suggested that both features exhibit a high probability of eruption to produce a coronal mass ejection (CME). The thesis begins with an introduction to the solar atmosphere and the physics governing its behaviour. The physics involved in flaring and CME onset will then be introduced and difficulties in our understanding of the relationship between these events highlighted.

Solar instrumentation and data analysis techniques used throughout this thesis is also introduced together with a discussion of capabilities and limitations.

Although many authors have referred to 'sigmoidal' features in the corona, observations have not yet confirmed the nature of such features. Sigmoidal active regions previously observed using Yohkoh/SXT alone form the basis of a multi-wavelength study incorporating SOHO/LASCO, EIT and MDI observations, together with ground-based H-alpha data. Regions previously classified as 'sigmoidal' are frequently found to comprise several shorter loops, the overall projection of which appears to form a single S (or reverse-S) shaped feature.

An example of a non-active region sigmoid is studied in terms of its morphology, CME and flaring activity over three solar rotations. This study is the first to consider a sigmoidal feature unconfined by a single active region in detail. The region's flaring and CME activity is studied and the relative timing of eruptive activity and sigmoid appearance is considered.

Previous studies have shown transequatorial loop systems (TLS), connecting active regions in opposite hemispheres to disappear in association with CME onset. This thesis describes a number of TLS in terms of their formation, morphology and associated CME and flaring activity. TLS are found to exhibit a variety of responses to CME onset including both brightening and dimming. Loops extending over a wide range in latitude appear more likely to be associated with CME onset.

Contents

List of Figures

List of Tables

1.Introduction

This thesis describes three new studies, each of which focuses on solar features previously shown to occur prior to the ejection of a coronal mass ejection (CME) [e.g. Canfield, Hudson & McKenzie, 1999; Khan & Hudson, 2000]. The studies described in this thesis focus on sigmoidal (S or reverse-S shaped) soft X-ray features observed on the solar disk and transequatorial loops connecting regions of the corona in either solar hemisphere.

The thesis begins with an introduction to the relevant solar physics background and instrumentation. This is followed by a description of the studies themselves. Final conclusions are then drawn from all three studies in the final chapter.

1.1 The Solar Atmosphere

Traditionally, the solar atmosphere is divided into layers in accordance with the temperature of the emitting plasma, as shown in Figure 1.1.

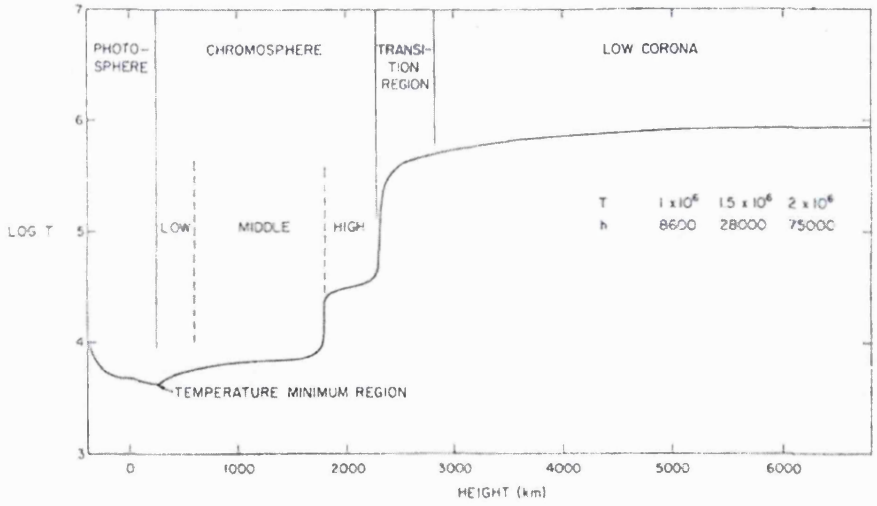

Figure 1.1: Temperature structure of the solar atmosphere. A dramatic rise in temperature is shown to occur over the narrow transition region. This region divides the chromosphere and the $>10^6$ K corona [Athay, 1976].

The atmospheric layers illustrated in Figure 1.1 are the photosphere, chromosphere, transition region and corona. These layers form the basis of the plane-parallel atmosphere model.

1.1.1 The Photosphere

The photosphere forms the visible "surface" of the Sun. It is a very thin layer of plasma, which is defined either as the region of approximately 550 km thickness extending from $\tau_{5000}=1$ up to the temperature minimum of 4300 K or as the region of about 100 km thickness centred on $\tau_{5000}=1$ and from which most of the Sun's light is emitted.

Large scale convection is visible at the photosphere in the form of supergranulation. Supergranule cells have typical dimensions 30,000 km (40") and may last for 1 to 2 days. A weak upflow of material is observed at the centre of the cell (velocity approximately 0.1 kms^{-1}) and a horizontal flow of approximately 0.4 kms^{-1} transports material outwards towards cell boundaries where a downward velocity of about 0.1 kms^{-1} is observed. These supergranules outline a network of convection cells with magnetic fields concentrated at the boundaries [Gabriel, 1976; Schrijver et al., 1999].

The magnetic field at the photosphere can be measured through use of the Zeeman effect. This effect is produced by the influence of a magnetic field on a spectral line emitted by an atom and is a result of the current produced by orbiting electrons. This current will have an associated magnetic field that will interact with the external field causing an addition or subtraction of the normal energy carried. The resulting spectral line is then split into a number of components, the separation in wavelength being dependent on external field strength.

1.1.2 The Chromosphere

The chromosphere is defined as the region existing between the temperature minimum and the corona. It extends from approximately 550 km to 2300 km above the base of the

photosphere. Over this range in height the temperature increases from approximately 4300 K to 30,000 K, as illustrated in Figure 1.1.

One of the most striking features observed at chromospheric temperatures is called a "prominence" or "filament". Observed for many years during eclipse observations of the corona, these features appear as bright red patches suspended above the solar limb. Prominences are termed filaments when seen on the solar disk. In these observations, they appear as long dark channels of material an order of magnitude denser than the surrounding corona at approximately $10^{11\text{-}12}$ cm^{-3}. This material is suspended in the hot corona above a neutral line (locus of points where the magnetic field passes through zero) by the action of surrounding magnetic fields. Several configurations have been proposed in order to explain prominence support [e.g. Kippenhahn & Schlüter, 1957; Kuperus & Raadu 1974]. All of these configurations assume that the magnetic tension force provides support for the prominence material, although the topologies of the support structures differ. The origin of the suspended material is still uncertain; it may be siphoned up from the chromosphere below or alternatively, it may condense from nearby coronal material to form the prominence [e.g. Anzer, 1989; Low, 1996].

The narrow transition region exists between the chromosphere and the corona. This name defines a region where the temperature rises rapidly from a few thousand degrees to more than 10^6 K.

1.1.3 The Corona

The corona is an extremely hot, tenuous layer extending from the Sun's transition region out beyond the Earth's orbit and into the heliosphere. During a solar eclipse, it can be observed as a bluish-white halo surrounding the Sun. This halo has an intensity of approximately one millionth of the photosphere.

The white light corona consists of scattered photospheric light. Scattering takes place both from free electrons and from dust grains in the corona. This gives rise to two main components: the K-corona and the F-corona. Both K and F coronae decrease in brightness with increasing distance from the Sun, as shown in Figure 1.2.

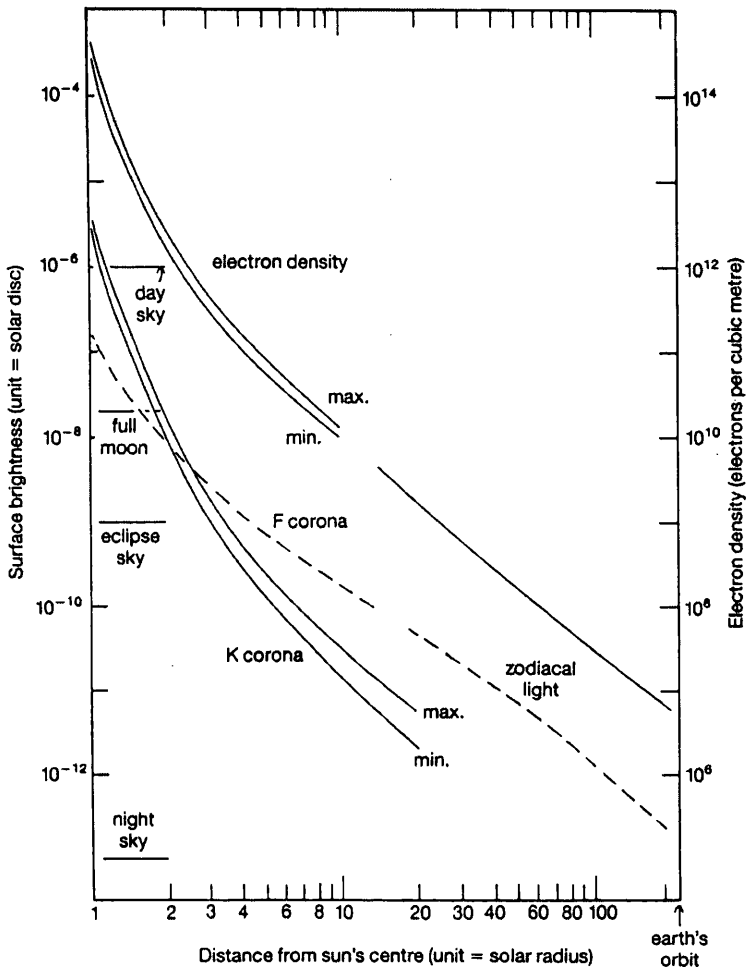

Figure 1.2: Variation of coronal surface brightness and electron density with distance from the Sun's centre out to the Earth's orbit. The K corona surface brightness is shown for solar maximum and minimum as is electron density (from Phillips [1992]).

The electron scattered K-corona is the most intense of these two components between the photosphere and approximately 2 solar radii. The spectrum consists of a continuum, similar to that of the photosphere, but without the strong Fraunhöfer lines. These lines are Doppler broadened to such an extent that they become unrecognisable owing to the presence of high-speed coronal electrons (~10,000 kms^{-1}).

Beyond approximately 2 ½ solar radii, the F-corona becomes more intense than the K-corona. This radiation is produced by sunlight scattered from dust particles in interplanetary space. These particles form a disk-like structure around the Sun close to the ecliptic plane. The orbital velocities of these particles are much slower than those of the coronal electrons. Hence, the Fraunhöfer lines are not significantly broadened and are observed in the spectrum of the F-corona.

The first evidence of the extreme temperatures present in the corona was provided when Edlén [1942] first identified the coronal 'green' (wavelength 530.3 nm) and 'red' (wavelength 637.5 nm) lines as corresponding to the forbidden transitions of Fe XIV and Fe X respectively. The observation of Fe XIV implied an extremely high coronal temperature of approximately $2x10^6$ K. These "forbidden" states are metastable, and if undisturbed by collision may exist for several days. Thus, the observation of these transitions also implied very low coronal densities. A high density would result in a greater probability of de-excitation from these states by collision with free electrons.

Due to the high temperature of the corona, emission is dominated by lines characteristic of highly ionised species and thermal bremsstrahlung ('braking radiation'). Bremsstrahlung occurs when an electron passes close to a positive ion and strong electric forces cause the electron trajectory to change. Deceleration of the electron causes it to radiate electromagnetic energy.

Short wavelength solar emissions such as X-ray and Extreme Ultraviolet radiation are unable to penetrate the Earth's atmosphere. Therefore, observation of the hot coronal emissions must be made from space based observatories. To date, observatories launched with this aim have included X-ray telescopes launched on a series of sounding rockets, the Orbiting Solar Observatory (OSO) and Orbiting Geophysical Observatory (OGO) series, Skylab, the Geostationary Operational Environment Satellites (GOES), P78-1, the Solar Maximum Mission (SMM), Hinotori, Yohkoh, SOHO, TRACE and RHESSI.

Early sounding rocket measurements indicated that the corona could be separated into three distinct regions. These were defined as (a) the polar regions, characterised by their reduced soft X-ray emission, (b) the quiet corona and (c) localised regions of bright emission associated with sunspots. These regions were later termed "active regions".

The first grazing incidence telescope to observe the corona was the X-ray spectrographic telescope (S-054) flown on Skylab in 1973. This telescope produced high-resolution soft X-ray images of the corona [Vaiana et al., 1973], illustrating for the first time that the corona was highly structured and composed of numerous bright loops. These bright, X-ray structures trace out the form of the coronal magnetic field as a collection of closed loops, with footpoints rooted at the photosphere.

1.2 Coronal Structure

This section introduces some of the expressions that are commonly used to define the structure of the corona. Under the assumptions that the plasma is continuous, length scales of typical coronal structures greatly exceed those of typical internal plasma lengths, time scales far exceed collision times and length scales are much longer than the particles' mean free path, the plasma may be represented by the equations of magnetohyrodynamics (MHD) [e.g. Priest, 1982].

1.2.1 Magnetic Pressure and the Induction Equation

In the ideal MHD limit, Ampère's law can be written as follows:

$$\underline{\nabla} \times \underline{B} = \mu . \underline{j} \qquad \text{-(1.1)}$$

where $\underline{B}$ denotes magnetic induction, $\underline{j}$ the current density and μ the magnetic permeability of the plasma. Under the conditions of electrical neutrality, the equation of motion for a plasma can be written:

$$\rho\left(\frac{D\underline{v}}{Dt}\right) = -\underline{\nabla} p + \underline{j} \times \underline{B} + \underline{F} \qquad \text{-(1.2)}$$

where ρ is the mass density and p is the plasma pressure (scalar). In addition, the material is subject to a pressure gradient ∇p, a Lorentz force $\underline{j}$ x $\underline{B}$ per unit volume and an additional force $\underline{F}$, which represents the combined effects of gravity and viscosity. Substituting Ampère's law from Equation 1.1 into the expression for the Lorentz force gives

$$\underline{j}\times\underline{B}=\frac{1}{\mu}(\underline{\nabla}\times\underline{B})\times\underline{B}=-\underline{\nabla}B^2/2\mu+(\underline{B}\bullet\underline{\nabla})\underline{B}/\mu \qquad \text{-(1.3)}$$

Comparison of the right hand sides of Equations 1.2 and 1.3 shows that the gradient of $(B^2/2\mu)$ can be grouped with the negative plasma pressure gradient such that this term constitutes a *magnetic pressure*:

$$P_B = B^2/2\mu \qquad \text{-(1.4)}$$

The ratio of plasma pressure to magnetic pressure is known as the plasma-β:

$$\beta = p/\left(B^2/2\mu\right) \qquad \text{-(1.5)}$$

This ratio provides a measure of the extent to which the magnetic field influences the plasma. The tenuous corona has low density and therefore low plasma pressure. As a result, the magnetic pressure will dominate the plasma motion and $\beta<<1$. Conversely, in the low chromosphere and photosphere, the plasma density is much higher and the plasma pressure will dominate the magnetic field. In this case $\beta\geq 1$.

Plasma moving with a velocity v through a magnetic field B, under the above assumptions will be governed by Maxwell's equations in the ideal MHD limit. Combining Faraday's Law, Ampere's Law and Ohm's Law gives the *Magnetic Induction* equation.

$$\frac{\partial \underline{B}}{\partial t} = \underline{\nabla} \times (\underline{v} \times \underline{B}) + \eta \nabla^2 \underline{B} \qquad \text{-(1.6)}$$

where $\eta = 1/(\mu\sigma)$, the *magnetic diffusivity*. The first term on the right hand side is the advection term, defining the advection of magnetic field lines carried by plasma motions. The second term describes diffusion of the plasma through the magnetic field. The ratio of these two terms gives the magnetic Reynolds number. This value provides a measure of the coupling of the magnetic field and plasma motion.

$$R_m = \frac{l_o V_o}{\eta} \qquad \text{-(1.7)}$$

where l_o and V_o are typical length and velocity scales. In the corona the magnetic Reynolds number is much greater than unity ($R_m = 10^6$-10^{12}) and consequently, the coupling is strong.

In the perfectly conducting limit, as is assumed to be the case for most coronal structures, the diffusion term can be ignored and magnetic field lines will behave as if they move with the plasma. Field lines are then considered to be *frozen into* the plasma.

Under the above assumptions, in the low plasma-β corona ($\beta << 1$), the magnetic field both contains and defines the plasma. Thus the bright loop-like structures observed in soft X-ray images of the corona can be interpreted as tracing out magnetic field lines. This allows the orientation of the magnetic field to be inferred by comparison with line-of-sight magnetogram data indicating the magnetic field at the photosphere.

The frozen-in flux assumption also holds in the higher plasma-β chromosphere and photosphere. In this case, the increased density and resulting increased influence of the plasma over the magnetic field, has the effect of dragging the magnetic field through the convective and differential motions of the photosphere.

1.2.2 Magnetic Reconnection

Initially proposed as an energy release mechanism for solar flares by Sweet [1958] and Parker [1957], further developed by Petschek [1964] and many authors since, magnetic reconnection is commonly thought to be the mechanism through which stored magnetic energy is converted into thermal and kinetic energy in the corona. This mechanism is commonly used to account for impulsive energy release in the corona over a wide variety of scales [e.g. Shibata, 1996; Shibata, 1999; Priest, 2000]. These size scales range from small-scale nanoflares [Parker, 1988; Yokoyama & Shibata, 1995] through to large scale solar flares, during which energies in excess of 10^{25} J may be liberated.

Reconnection is defined as a change in connectivity of plasma elements in a magnetic field. The process can be visualised as the breaking of two anti-parallel magnetic field lines. The broken ends of each line connect with parts of the adjacent line as illustrated in Figure 1.3. Magnetic reconnection acts to remove stored energy from the magnetic field, causing the system to evolve through a series of equilibria until a minimum energy state is reached. In an ideal case, this final state would be a potential field with no stored energy.

Under normal conditions in the solar corona, the magnetic Reynolds number (Equation 1.7) will be large ($R_m >> 1$) and coupling between the magnetic field and plasma will be strong

For reconnection to occur, the magnetic field must be able to diffuse through the plasma. Equation 1.7 shows that this can occur for regions where the length scale is extremely small and where the resistivity of the plasma becomes locally enhanced. These conditions form where magnetic fields of opposite polarity are brought together. At this location, an X-type magnetic neutral point and current sheet will form. In the coordinate system of Figure 1.3, the current will act along the Z-direction. Reconnection is self-propagating and will continue between adjacent field lines until an energy minimum is reached. Energy balance shows that there will be a flow of magnetic field and plasma into the reconnection site (due to magnetic pressure) and a flow of field and plasma out of the

reconnection site (due to magnetic tension). The outflowing plasma will travel at the Alfvén speed (~1000 kms^{-1} in the corona).

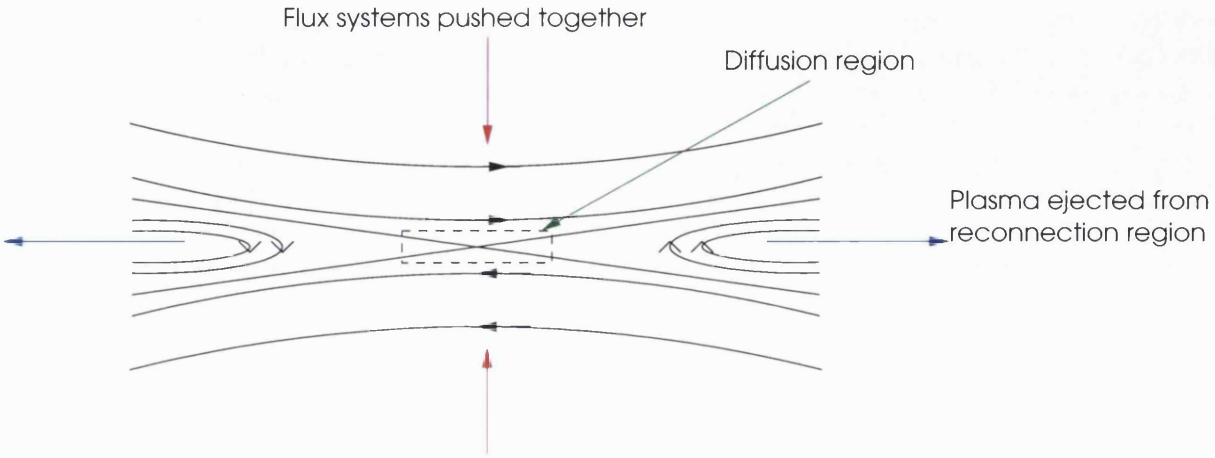

Figure 1.3: Reconnection scenario illustrating a magnetic X-point in 2-D. Plasma motion pushes two sets of field lines towards the diffusion region where reconnection is able to occur. Newly reconnected lines are then pushed away from the diffusion region. In this scenario, current would flow along the Z-axis (acting out of the paper).

1.2.3 Magnetic Flux Tubes in the Corona

One of the clearest examples of magnetic flux tube presence is the sunspot. These features form as a portion of the Sun's internal field emerges through the photosphere. The sunspot may be formed by a single flux tube or a collection of flux tubes, the combined flux density of which leads to a localised depression in convection. This gives the sunspot its characteristic dark appearance in white light observations.

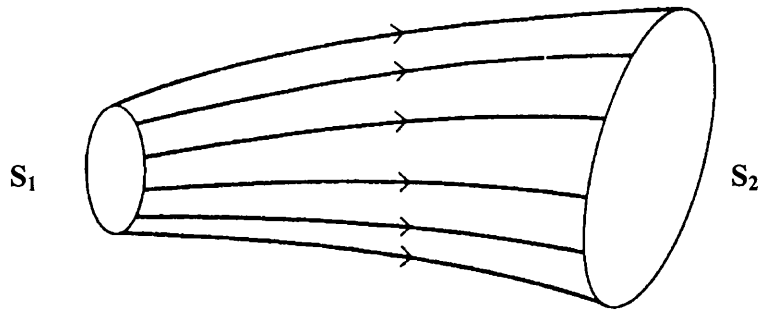

Figure 1.4: Schematic illustration of a flux tube (from Priest, 1982). The total flux crossing surface S_1 is equal to that crossing S_2

Consider any surface S_1 in the plasma not parallel to the lines of force. The frozen-in-flux condition states that the total magnetic flux crossing that surface will remain constant. The field lines are tied to the plasma such that if the surface were to shrink or expand, the field would be strengthened or weakened respectively, thus maintaining a constant flux through the surface. Following the field lines along their length maps out a spatial volume referred to as a flux tube, as illustrated in Figure 1.4. The strength of a flux tube is defined as the amount of flux crossing any cross-section along the length of the tube.

$$F = \int_S \underline{B} \cdot \underline{dS} \qquad \text{-(1.8)}$$

The frozen in flux condition, therefore, implies that all particles initially tied to a flux tube will remain linked along that flux tube unless other processes, such as reconnection, lead to a change in the field line connectivity.

Sigmoidal features observed on the solar disk are frequently interpreted as the projected appearance of helically twisted flux tubes [Rust & Kumar, 1996]. Flux tubes will be referred to in this context throughout this thesis.

1.2.4 Force-Free Fields

Comparing the size of each term in the equation of motion (Equation 1.2) illustrates that the terms on the left hand side can be neglected if the flow speed is much smaller than the sound speed, the Alfvén speed and the gravitational free-fall speed for a vertical scale length. Thus the equation of motion reduces to a magnetohydrostatic balance between the pressure gradient, the Lorentz force and the gravitational force:

$$0 = -\nabla p + \underline{j} \times \underline{B} + \underline{F} \qquad \text{-(1.9)}$$

In the low-β coronal plasma, the Lorentz force will dominate both the additional forces if the vertical extent being considered is much smaller than Λ/β, where Λ represents the scale height of the medium. This would be the case above an active region. Consequently, the force balance will reduce to

$$\underline{j} \times \underline{B} = 0 \qquad \text{-(1.10)}$$

This indicates that electric currents will only flow *along* field lines. Substituting for Equation 1.1 (Ampère's Law), this can be rewritten:

$$\underline{\nabla} \times \underline{B} = \alpha \underline{B} \qquad \text{-(1.11)}$$

where α is a function of position, remaining constant along field lines, which describes twist. If α takes the same value on each field line, a *linear* or *constant-α* force-free field results and the curl of Equation 1.11 reduces to

$$\left(\nabla^2 + \alpha^2\right)\underline{B} = 0 \qquad \text{-(1.12)}$$

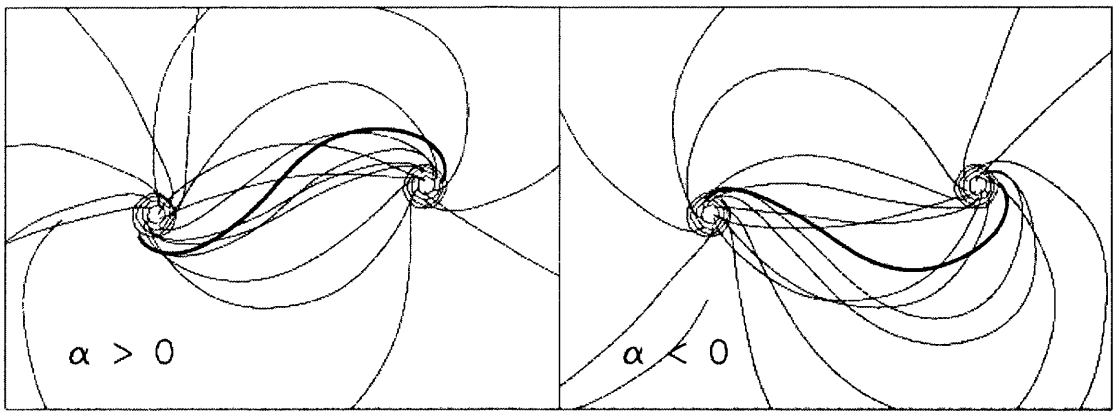

Figure 1.5: This figure shows model bipolar linear force-free fields computed for positive and negative α. Contours show vertical magnetic field strength. Magnetic field lines are projected onto the horizontal plane. A field line near the central part of the dipole is shown with a heavy line to demonstrate the sense of twist (i.e., S for positive and reverse-S for negative). From Pevtsov, Canfield and McClymont [1997].

The presence of field-aligned currents indicates that the simplest form of a constant-α closed surface would be a torus on which the line of force spirals. The sign of α will then determine the orientation of the spiral. Figure 1.5 illustrates differing field configurations that might arise in the corona for positive and negative constant-α fields. This property of twist, when observed in coronal fields is often referred to as handedness or *chirality* and depends on whether the field lines twist as a left or right-handed screw. Positive α fields tend to produce a right handed twist and result in S-shaped loops in the corona, whereas negative α fields produce a left handed twist and are associated with reverse-S shaped loops in the corona. Several studies have shown a slight tendency for positive chirality fields to be present in the southern hemisphere and negative in the north [e.g. Canfield, Hudson & Pevtsov, 2001]. Approximately 60-70% of active regions in each hemisphere exhibit a preferred chirality. Recent research into large scale loops that interconnect active regions in the corona has shown that these interconnecting loops are more likely to form between active regions whose fields possess the same chirality [Canfield, Pevtsov & McClymont, 1997].

1.2.5 Magnetic Helicity

Magnetic helicity is defined in 3-D as the extent to which field lines wrap and coil around one another. Viewed in projection against the solar disk, S- or reverse-S shaped soft X-ray features have been interpreted as helically twisted flux ropes [Rust & Kumar, 1996]. The chirality of these features is thought to indicate whether the flux rope is in possession of positive or negative magnetic helicity [Pevtsov, Canfield & McClymont, 1997].

Observations of magnetic clouds at 1AU have been linked to the disappearance of quiescent filaments seen on the solar disk [e.g. Webb, 1992]. Further studies have shown that these magnetic clouds often exhibit the same chirality as the underlying eruptive feature [Bothmer & Schwenn, 1994]. Consequently, if the erupting CME field and its associated helicity are disconnected entirely from the photosphere, the CME can be interpreted as a means by which embedded flux, and thereby helicity, can be carried away from the low corona and into interplanetary space. This would lead to removal of the twisted embedded flux observed in soft X-ray data in agreement with the observed "sigmoid-to-arcade" scenario that will be discussed in detail in Chapter 4.

In order to visualise the topological influence of magnetic helicity on a system, the helicity of a closed flux tube, H, can be expressed as the sum of two terms:

$$H = \Phi^2(Tw + Wr) \qquad \text{-(1.13)}$$

These terms are defined as the ***Twist*** of magnetic field lines about the flux tube axis and the ***Writhe*** undergone by the flux tube axis itself. The second, *writhe*, term represents kink-like deformations undergone by the axis. The multiple Φ then refers to the magnetic flux contained within the tube. Individually, the two terms are defined:

$$Tw = \frac{1}{2\pi}\oint q(l)dl \qquad \text{-(1.14)}$$

$$Wr = \frac{1}{4\pi}\oint dl \oint dl' \frac{\hat{l} \times \hat{l}' \cdot (x - x')}{|x - x'|^3} \qquad \text{-(1.15)}$$

where $x=x(l)$ and $x'= x'(l')$ are the distance along each of the two linked flux tube axes and $q(l)$ is the twist per unit length. Conservation of helicity states that magnetic helicity H will be conserved in the corona under ideal motions [Berger, 1999]. Therefore a change in writhe experienced by the flux tube axis must be offset by a change in magnetic field line twist having opposite sign. Figure 1.6 illustrates of the principle of helicity conservation. If a left-handed deformation (writhe) were applied to a flux tube, the field lines would respond by gaining an equal and opposite right-handed twist about the axis.

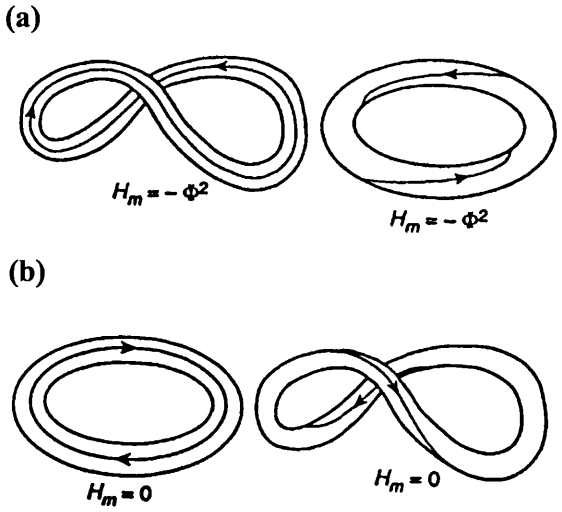

Figure 1.6: Magnetic topology and helicity conservation. Figure (a) illustrates that a kinked flux rope can be flattened out, but the resulting toroid will possess an equal and opposite twist to the initial writhe. Figure (b) shows that an initially untwisted and unwrithed toroid can be distorted to exhibit twist helicity equal and opposite to its writhing helicity (adapted from Rust, 1997).

1.3 Coronal Activity

This section introduces the concept of the 11-year solar activity cycle and gives an overview of the current understanding of solar flares and CMEs.

1.3.1 The 11 year Cycle

The presence of an 11-year cycle in solar activity was initially proposed by Heinrich Schwabe in 1859 from an analysis of Maunder's sunspot observations [1922]. However, the model commonly employed to explain the characteristics of the solar cycle is that of Babcock [1961].

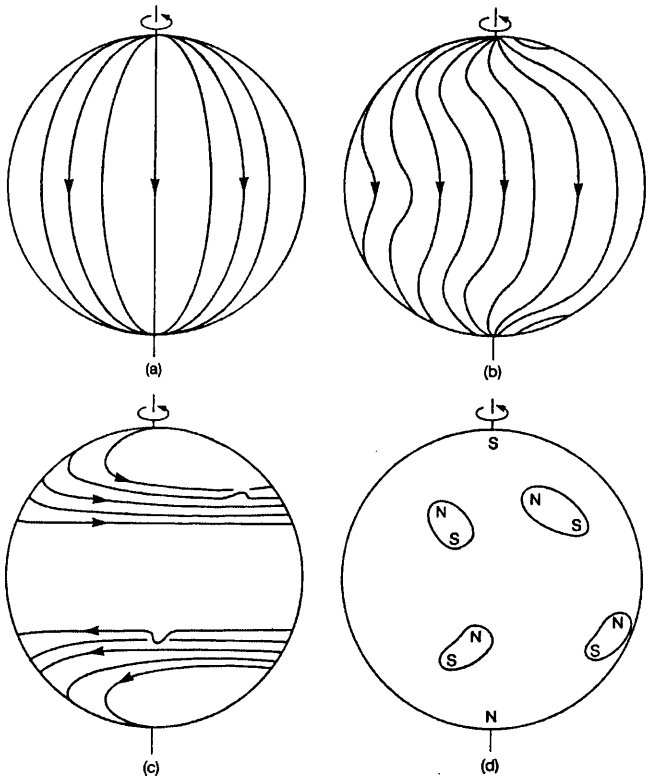

Figure 1.7: The 11-year solar cycle (adapted from Babcock, 1961). Figure (a) shows an initial bipolar configuration consistent with the start of the solar cycle at solar minimum. The action of differential rotation causes the equatorial regions to rotate faster than the poles. As a result, the field is wrapped around the Sun (b), until it approaches a toroidal configuration (c). Sunspots are thought to originate from the toroidal field bands (d) through the action of convection on submerged fields.

The Sun is known to rotate differentially. Sunspot observations, and more recently Doppler measurements, have shown that equatorial regions rotate with a period

of approximately 26 days while polar latitudes rotate in approximately 36 days. Thus, the action of solar differential rotation on plasma and its associated frozen-in field in the dense interior, will result in the field nearer the equator rotating faster than the field near the poles. This differential rotation is thought to create a dynamo effect. The field strength is increased in a similar manner to an electromagnet through winding of the frozen-in field about the equator. Figure 1.7 illustrates the main stages of the solar cycle model proposed by Babcock [1961].

The Babcock model is divided into five stages. During the initial stage, the solar field is said to be approximated by an axi-symmetric dipole, as illustrated in Figure 1.7a. The action of differential rotation on the dipolar field results in the field lines being drawn out in longitude. A period of approximately 3 years leads to field lines being wrapped around the Sun 5 times in a toroidal configuration. Sunspots are thought to emerge from these twisted toroidal field bands, the action of convection on the submerged field lines twisting them into long flux ropes.

As the solar cycle continues, the action of differential rotation continues to twist the internal field, drawing the toroidal component closer to the equator.

Solar activity reaches a peak after approximately 5 years. Following this, the number of sunspot regions will decrease and the field will return to a dipolar configuration. This configuration is similar to the initial state, but field polarity will be reversed. The regeneration of a poloidal field is attributed to the observation that sunspot groups are tilted with respect to the lines of latitude. Leading spots in each hemisphere have opposite polarities and neutralise as they drift towards the equator. Similarly, following polarities will migrate towards the poles, eventually neutralising the remaining bipolar component and replacing it with a poloidal field of opposite polarity to the initial field. This process is repeated in a 22-year cycle of activity.

Despite the ability of the dynamo model to accurately reproduce many features of the solar cycle, several uncertainties remain.

One of these arises in the mechanism by which small-scale bipolar regions combine to form a larger scale field towards the end of the solar cycle.

Here transequatorial loop systems may play an important role, since they connect regions of opposite polarity across the equator. Moreno-Insertis [1986] illustrated that flux is likely to emerge separately in either hemisphere, forming transequatorial connections in the corona. Therefore, if these structures are indeed shown to be eruptive, they could provide an important mechanism by which the solar field is able to regain its poloidal configuration at solar minimum.

1.3.2 Solar Flares

Solar flares are sudden and rapid releases of magnetic energy in the solar atmosphere. During a flare, energy is explosively released in various forms including particle acceleration, plasma heating, acceleration of plasma and enhanced radiation fields. Flares can last for a few minutes to several hours. The amount of energy released is of the order of 10^{25}J. Smaller events are termed 'microflares' or 'nanoflares' [e.g. Hudson, 1991].

Flares are most commonly observed in areas of strong and complex magnetic fields. As a result, the frequency with which flaring occurs is observed to vary with the solar cycle.

1.3.2.1 Classification

Because flares occur over a range of orders of magnitude, they are classified according to two main schemes. These are Hα importance and soft X-ray class. This thesis will refer to solar flare magnitude in terms of the X-ray classification scheme. This scheme is based on the integrated total output of soft X-rays detected from the Sun in the wavelength range 1-8 Å. X-ray levels are monitored by the Geostationary Operational Environment Monitors (GOES) series of satellites. These satellites each carry a full Sun soft X-ray monitor, and together provide continuous coverage of solar soft X-ray flux from their locations in geostationary orbit. Flare strength is measured by the peak intensity in Wm^{-2} within the 1-8 Å range. The letters, A, B, C, M and X are used to represent increasing intensities in order of magnitude steps e.g. a C-class flare would have a peak intensity of

10^{-6} Wm^{-2}. Each order of magnitude is further divided into increments, such that a flare having peak emission $4x10^{-6}$ Wm^{-2} would be classified at the C4 level.

1.3.2.2 Solar Flare Models

Numerous models have been proposed to explain the characteristics of solar flares [see reviews by Shibata, 1996; Shibata, 1999; Priest, 2000]. However, to date, none have reproduced every aspect of the observations successfully and many important questions regarding the nature of solar flares have yet to be answered.

Solar flares may be divided into two main classes. These are:

(1) *Confined or 'impulsive' flares* and
(2) *two-ribbon flares,* also termed *long duration events* (LDEs).

The second class of events is understood to arise from the eruption of an overlying filament [e.g. Priest, 1982]. This type of event is frequently associated with coronal mass ejection onset and numerous models exist which relate the onset of a two-ribbon flare to that of a CME [e.g. Illing & Hundhausen, 1985; Low, 1996; Gosling, Birn & Hesse, 1995; Gosling, 1999]. Confined flares, also known as "impulsive flares", are much shorter lived than two-ribbon events. However, the physics governing reconnection itself (see Section 1.2.2) is thought to be common to both types of flare [Shibata, 1999].

The "standard model" for two-ribbon flares has been developed over many years by a number of authors including Carmichael [1964], Sturrock [1968], Hirayama [1974] and Kopp and Pneuman [1976]. This model will be referred to here as the CSHKP model. The schematic illustration in Figure 1.8, provides a cross-section of the two-ribbon flare. This aspect of the CSHKP model proposes that flaring begins with the sudden opening of previously closed magnetic field lines in the corona [Kopp & Pneuman, 1976].

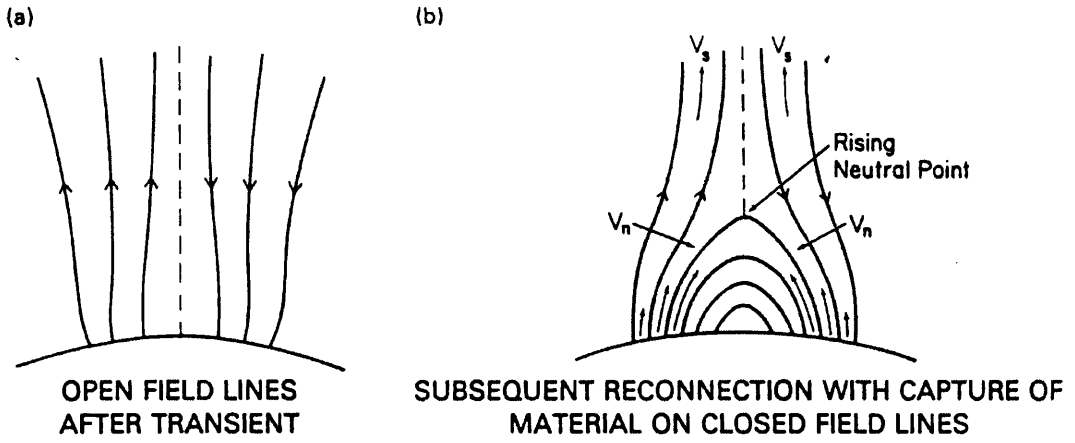

Figure 1.8: Field configuration following ejection of prominence material. Figure (a) shows a bipolar open field configuration with neutral sheet produced by the force of the ejected transient. Figure (b) illustrates a rising loop system during the reconnection phase. V_s denotes solar wind velocity along the open field lines while V_n denotes velocity of field lines moving towards the neutral sheet (from Kopp & Pneuman, 1976).

Prior to destabilisation, the material is thought to be of high density, with pressure, gravitational, inertial and magnetic forces in balance. Through the sudden release of mass and energy associated with a filament eruption, field lines will form an open configuration similar to that shown in Figure 1.8a. Solar wind expansion acts to further reduce the plasma pressure within the region. The resulting loss will reduce the plasma pressure to levels below those that existed prior to eruption. As a result, an inward magnetic (Lorentz) force arises which can no longer be balanced by pressure forces. The Lorentz force drives field lines of opposite polarity towards the neutral sheet and reconnection will begin, acting upwards from the coronal base (Figure 1.8b). The terminology "two ribbon flare" originates from Hα observations made at the time that this process is taking place. Reconnection is thought to involve acceleration of electrons which then travel along magnetic field lines, away from the reconnection site and down towards the chromosphere. Here they cause heating and an increase in emission near the loop footpoints. This emission is often observed as two bright 'ribbons' of Hα emission located to either side of the neutral line.

Figure 1.9 shows a more detailed 2-D schematic representation of some of the main features thought to occur in association with reconnection in a solar flare.

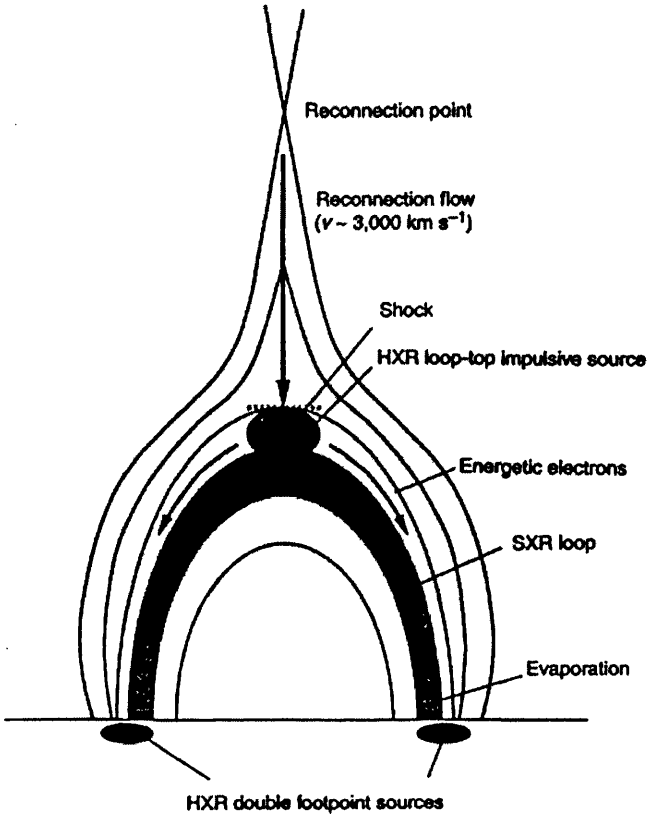

Figure 1.9: Magnetic geometry for reconnection in a solar flare. Elongated anti-parallel magnetic field lines exist above an arcade of loops, a current sheet forms between them and anti-parallel lines reconnect. An outflow or 'jet' from the reconnection site then impinges on the underlying closed loop and forms a shock, resulting in the formation of a high temperature (T_e~$2x10^8$ K) region just above the closed loop (from Masuda et al., 1994).

This figure is strictly a cross-sectional model produced to explain observations of compact solar flares, although the key properties illustrated are also thought to be present in the two-ribbon case [Shibata, 1999]. Accelerated electrons travel down the loops and impinge on dense chromospheric material. This results in two main observational effects:

1. Hard X-ray bremsstrahlung emission caused by deceleration of the energetic electrons as they come into contact with chromospheric material and
2. Chromospheric evaporation arising from explosive heating of the chromosphere.

In the latter case, energy carried by the accelerated electrons is transferred to the chromospheric material. This heated material then expands and is transported upwards along the newly reconnected field lines where it emits thermally at soft X-ray temperatures, eventually cooling to emit in the EUV temperature range and below [Neupert, 1968].

One way in which impulsive flares differ from long duration events is in the appearance of reconnected field lines. In the impulsive model, a short burst of reconnection lasting for some tens of minutes leads to the appearance of a bright soft X-ray loop above which the reconnection site is thought to be located at a distance of 5"-10" [Masuda et al., 1994]. This differs from the LDE case where reconnection may take place over a period of several hours, leading to the appearance of a soft X-ray cusp or arcade [Tsuneta et al., 1992].

As mentioned at the start of this section, the standard model does not address all aspects of flares and many questions remain unanswered. A full description of these questions is beyond the scope of this thesis. However, two major topics of flare research that will be mentioned briefly here are the mechanism by which particles are accelerated during the flare and the method by which energy is stored in the corona prior to the flare taking place.

In order to produce typical hard X-ray fluxes via the thick-target, non-thermal bremsstrahlung model [e.g. Tandberg-Hanssen & Emslie, 1988], about 10^{37} electrons.s^{-1} would be needed. However, integrated over the hard X-ray burst, this accounts for more material than is available in a typical flaring loop. Additional material must, therefore, be supplied to the loop; the source of which is as yet unknown. It has been proposed that this material is replaced in real-time by return currents from the heated chromosphere. However, these have not yet been observed. In addition, the efficiency (i.e. ratio of magnetic energy existing prior to flaring to that converted into particle acceleration

during the flare) of the particle acceleration mechanism also appears to contradict laboratory measurements. Solar flare observations indicate a much more efficient electron acceleration mechanism (~50%) than laboratory measurements suggest (~5%). See e.g. Miller et al. [1997] and Sudan and Spicer [1996] for a more detailed discussion of these questions.

Another question is that of energy storage prior to flare onset. For example, if one footpoint of a coronal loop is twisted, this would cause the loop to expand outwards, thus lowering the energy density of the poloidal component of the field [Priest, 1982]. In this case, although magnetic energy is increasing, the magnetic energy density needed to drive the flare is decreasing rather than increasing as would be required. This problem can be avoided by the presence of an overlying prominence [Sudan & Spicer, 1996]. The increased gravitational force would limit the expansion of the underlying field. However, it is not yet known whether there is sufficient gravitational energy stored in a prominence for this to occur. An additional model that may account for this additional restraining force is that of the flux breakout model [Antiochos, DeVore & Klimchuk, 1999]. This model assumes that the magnetic energy driving eruption is stored within highly sheared core fields close to the neutral line. These fields are restrained by the magnetic tension force supplied by an unsheared, overlying arcade. Reconnection can take place between the overlying arcade and neighbouring systems, thus transferring the overlying field elsewhere and removing a fraction of the restraining field from the underlying sheared core. Consequently the underlying core is able to "break out" and erupt without causing complete opening of the overlying field.

The flux breakout model of a solar eruptive event was developed with an additional question in mind. The Aly-Sturrock open field energy limit [Aly, 1999 and Sturrock, 1991] suggests that a completely open field state cannot be reached from a force-free state by energy release since the open field configuration has the highest energy of all force-free configurations with the same boundary conditions. Furthermore, in addition to the energy required to overcome magnetic restraints, more energy would be required to overcome gravitational forces and eject material into the corona. Thus, a coronal loop system would need to gain energy in order to erupt in the style proposed by

Kopp and Pneuman [1976], illustrated in Figure 1.8. The flux breakout mechanism allows this restriction to be bypassed since only a partial eruption of the field takes place.

It is also possible that a sudden increase in twist leading to instability is caused by reconnection [Pevtsov, Canfield & Zirin, 1996]. It has been shown that a flux rope will become unstable if the twist exceeds a certain value [Hood & Priest, 1979]. Consequently, if the twist of the pre-reconnection fields is additive, the longer flux rope formed after reconnection may possess a value of twist in excess of the maximum value for stability and erupt.

Despite many open questions, the standard model will be considered throughout this thesis, since it accounts for many of the key features that will be discussed in the context of these studies. This model is of particular relevance for Chapters 4 and 5 which discuss sigmoidal solar features. Hudson et al. [1998] and several authors since have interpreted the "sigmoid-to-arcade" development as a possible on disk signature of the CSHKP model.

1.3.2.3 Moreton and EIT waves associated with flaring

A further phenomenon associated with the impulsive phase of flaring is termed a Moreton wave [Moreton, 1960; Athay & Moreton, 1961]. Referred to as a wave-like disturbance originating from the vicinity of a flare, these phenomena appear as either a bright front in the Hα centre-line or a dark front in the Hα wing. They propagate at constant velocities within the range 330-4200 kms^{-1}, forming an arc stretching away from the flare site and reaching distances up to and in excess of a solar radius. Uchida [1968] interpreted these phenomena as the intersection line between an expanding coronal wavefront and the chromosphere.

Recent observations made using the Extreme-Ultraviolet Imaging Telescope (EIT) onboard SOHO have illustrated the presence of large scale transient propagation across the solar disk in a similar manner to that of the Moreton wave seen in Hα.

Wills-Davey & Thompson [1999], through study of a single event, showed that Hα observations of a Moreton wave can be consistent with both the spatial extent and

velocity of a coronal disturbance seen in EUV data. However, in most cases, Moreton waves form an arc with angular extent not exceeding 160° whereas EIT waves frequently span 360° about the flare site. The observed range of EIT wave speeds extends up to a few hundred kms^{-1} [Klassen et al., 2000]. This compares with only the slowest observed Moreton waves. In addition, EIT wavefronts are often diffuse and do not display clear shock-like boundaries. These observations suggest that EIT waves may not always be shock-like in nature. It is therefore possible that these waves do not ordinarily form the coronal counterparts of chromospheric Moreton waves. The theory that they may represent the energy input to the corona following CME onset has also been proposed [Thompson et al., 1999].

1.3.3 Coronal Mass Ejections

Coronal mass ejections (CMEs) were discovered in the 1970s when space-borne coronagraphs began taking regular white light images of the solar corona. Historically, coronagraphs onboard the Orbiting Solar Observatory (OSO-7) [Tousey, 1973], Skylab [MacQueen et al., 1974], P78-1 [Howard et al., 1985] and the Solar Maximum Mission (SMM) [MacQueen et al., 1980] have all observed CMEs from space. At present, the LASCO coronagraphs onboard SOHO [see Chapter 2 for a description of SOHO and LASCO] monitor the corona between approximately 2-30R_o, providing a wealth of information about the frequency and properties of CMEs in the corona.

CMEs are observed in coronagraph data as bright features expanding outwards through the corona at speeds ranging from tens of kms^{-1} to 2000 kms^{-1}. These bright features represent erupting sections of the coronal magnetic field and associated plasma. CMEs lead to the expulsion of approximately 10^{15}-10^{16}g of solar material, liberating an average 10^{24}-10^{25} J in work done against the solar gravitational field as the eruption takes place.

CMEs take on a variety of appearances in the corona. These include enhancements of radial streamers, diffuse clouds and single loops. One of the apparently simplest structures is that of the three-part CME, initially observed by Illing & Hundhausen

[1985]. A CME exhibiting this three-part structure is illustrated in Figure 1.10. The structure comprises:

a) a bright filamentary core identifiable as an eruptive prominence [Webb & Hundhausen, 1987],
b) a dark cavity with a well defined boundary and
c) above and surrounding both, a leading high density shell having the appearance of a loop when viewed in projection.

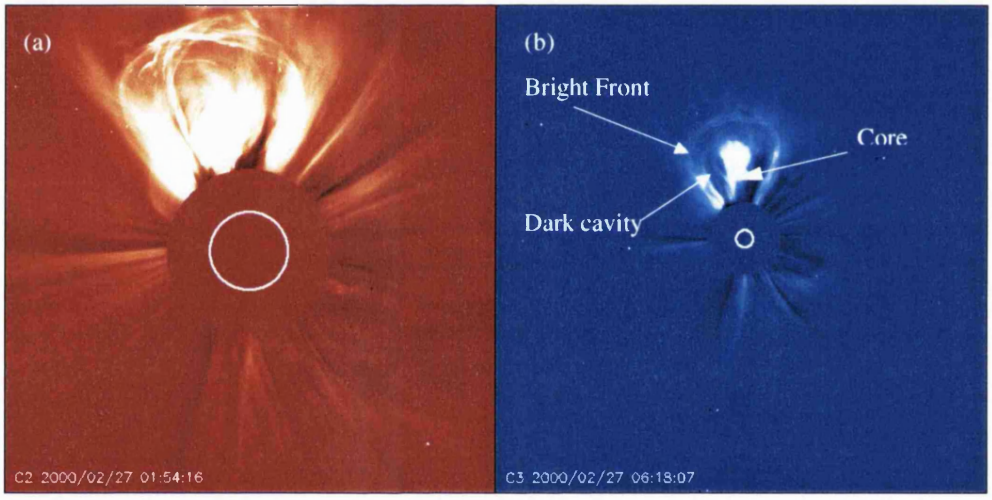

Figure 1.10: A Coronal Mass Ejection (CME) exhibiting a three-part structure, observed by the LASCO C2 (left) and C3 (right) coronagraphs. The CME appears complex as it crosses the C2 field of view (a) but develops a clear three-part structure in C3 (b). These images were produced using LASCO analysis software described in Chapter 3. The LASCO coronagraphs are described in more detail in Chapter 2.

The exact nature of CMEs is still uncertain. Howard et al. [1982] first suggested that the bright front observed in coronagraph data represents a bubble of material viewed in projection, rather than discrete loops. This observation was made using data from the SOLWIND coronagraph onboard the P78-1 satellite. These authors observed a bright "halo" of material expanding almost symmetrically about the occulting disk. Termed a

"halo" CME after its appearance, this CME led to strong geomagnetic activity three days after leaving the Sun.

It should be noted that coronagraph data is only able to provide information about the CME expansion in the plane of the sky, i.e. perpendicular to the line-of-sight. Brightness enhancements are caused by Thomson scattering of photospheric light off electrons in the corona [Hundhausen, 1993]. Thus, observation of a halo CME could indicate material moving towards or away from the observer. In order to determine whether the CME is approaching or receding, comparison is made with disk observations for possible onset signatures. These might include any or all of the following:

- formation of a soft X-ray arcade or cusp [Tsuneta et al., 1992],
- coronal dimming (X-ray or EUV) [Hudson & Webb, 1997; Thompson et al., 1999],
- coronal wave onset [Thompson et al., 1999]
- formation of Hα ribbons or post-flare loops [Munro et al., 1979].

In the case described by Howard et al. [1982], a flare was seen in Hα disk observations. This occurred at a time corresponding to the estimated onset time derived from CME measurements in the corona.

Recent studies [Dere et al., 1999; Chen et al., 1997; Low 1994] have interpreted the three-part CME structure to be the projected coronal appearance of an erupting magnetic flux rope. The bright front is thought to represent coronal streamer material pushed out ahead of the expanding flux rope and the dark cavity is interpreted as the complex field structures of the flux rope itself. At the trailing edge of the flux rope the erupting filamentary material is observed to emit strongly in Hα forming the CME 'core'.

The process by which a CME erupts is still uncertain, although it is generally accepted that CME onset is caused by a localised destabilisation of the magnetic field in the low corona.

The pre-CME structure is frequently associated with regions of quiet-Sun, specifically quiescent filaments which are often found at the base of a helmet streamer.

Helmet streamers comprise a high-density dome above which open field lines extend into the corona forming the bright radial streamers seen in coronagraph images. Below the dome a low-density cavity, and often an embedded prominence, are observed in a manner analogous to the three-part CME structure described above [Low, 1994; Hundhausen, 1999]. Illing & Hundhausen [1985] reported observation of a streamer expanding to a radial extent visible above the SMM coronagraph's occulting disk. Soon after its appearance at this height, the streamer erupted leading to CME onset.

Hundhausen [1993] proposed further evidence for a connection between CME onset and the distribution of helmet streamers in the corona. The distribution of CME onset latitudes is observed to vary systematically with solar cycle in a manner opposite to that of sunspots but similar to the observed distribution of quiescent prominences and helmet streamers. During solar minimum the distribution of CME onset latitudes is observed to peak near the equator. Hundhausen [1993] found the location of CME onset to be confined to a region extending ±30° of the heliomagnetic equator during the period surrounding solar minimum in 1985 and 1986. Similarly, this study also found that as the corona became more complex in the years approaching solar maximum, CMEs were observed to occur over a much wider distribution in latitude.

Initial theoretical studies suggested that a CME might be the coronal response to energy released through reconnection following a flare [e.g. Parker, 1961]. However, further observational studies have shown that whilst a strong correlation exists between flaring and CME onset, flaring is normally observed tens of minutes to an hour *after* CME onset [Harrison, 1986; 1991]. A strong correlation was also found between CME onset and filament eruption through studies of Skylab coronagraph data [Munro et al., 1979; Joselyn & McIntosh, 1981]. More recently Gilbert et al. [2000] found that 94% of eruptive prominences could be associated with CMEs observed in coronagraph data. The majority of these CMEs possessed a dense core in agreement with the three-part CME model. Studies providing comparison of CME leading edge and core expansion speeds from consecutive coronagraph images however, show that the filament frequently expands at a slower rate than the leading edge [Hundhausen, 1999; Plunkett et al., 2000]. It is, therefore, thought unlikely that the filament eruption drives the CME, although

filament activity is sometimes observed prior to CME onset [Low, 1997; Harrison & Lyons, 2000].

Recent studies have proposed that the destabilisation leading to CME onset is caused through the stressing of coronal fields. This might take place either through the action of large scale photospheric flows on emerged fields or reconnection of emerging flux with existing flux systems rendering them unstable and causing field lines to open in a manner similar to that described by Kopp and Pneuman [1976]. Feynman & Martin [1995] found a strong correlation between filament eruption and flux emergence within or in close proximity to the filament channel. This result can be linked to CME eruption through both the observational three-part structure described by Illing & Hundhausen [1985] (the inner part of the structure constituting erupting filament material), and the statistical connection found between CME onset and filament eruption [e.g. Gilbert et al., 2000; Munro et al., 1979]. This connection suggests that emerging flux might play a role in destabilising CME structures.

If CMEs can indeed be attributed to the eruption of magnetic flux ropes, the process by which they form in the corona remains a topic of intense debate. Rust [1994] suggested that filaments observed in the low corona form within magnetic flux ropes. Low [1994] interprets the dark cavity of a helmet streamer to represent a flux rope prior to eruption. However, other models [e.g. Gosling, 1999; Gosling Birn & Hesse, 1995] propose that the 3-part flux rope structure is formed through reconnection taking place *after* the initial eruption has occurred. Wood et al. [1999] provided observational evidence for flux rope formation taking place after the CME onset. These authors studied two CMEs. Both CMEs displayed magnetic flux rope characteristics but only one of these erupted with an associated filament. This led the authors to suggest that the flux rope structure did not exist prior to eruption in the case where no filament accompanied the CME: rather it was formed in the corona *after* the initial eruption had taken place.

A further uncertainty within CME models involves the question of whether the erupting CME detaches entirely from its base in the corona. Following eruption, radial coronal streamers frequently remain visible in coronagraph images. Corresponding to the remnants of the bright CME rim, these persist for a day or two giving the appearance of

'legs' where part of the CME may still remain connected to the lower corona. However, in order to maintain flux balance in the corona, theoretical studies have shown that CME flux should eventually be entirely disconnected from the photosphere [Kumar & Rust, 1996; DeVore, 2000].

1.4 CME Onset and the use of Proxies

As described in the preceding section, many aspects of the processes leading to CME onset are not yet well understood. Although the exact mechanism by which the CME erupts may not be known, a sequence of morphology changes might be common to some proportion of eruptive features, i.e. a certain type of coronal morphology might possess a high probability of eruption. Identification of these signatures and understanding the processes involved in their eruption may lead to the development of one or more 'proxies' with which CME onset can be inferred.

This thesis focuses on two such features, both commonly observed in soft X-ray data and each thought to possess a high probability of eruption. These are sigmoidal (S or reverse-S shaped) features and transequatorial loops.

1.4.1 Sigmoidal Solar Features

Highly sheared S and reverse-S shaped features have been observed in X-ray images of the solar corona since the Yohkoh soft X-ray telescope began taking regular images of the corona at temperatures of 2 MK and above [Sakurai et al., 1992].

Initially interpreted as the coronal manifestation of magnetic shear, recent studies have interpreted sigmoidal structures as the projected appearance of twisted magnetic flux tubes [Rust & Kumar, 1996].

S and reverse-S shaped soft X-ray features observed in the corona were initially associated with a high probability of eruption by Canfield, Hudson and McKenzie [1999]. This study focused on soft X-ray observations, using only a sigmoid-to-arcade/cusp proxy to infer CME onset. No comparison was made with white light coronagraph data or

EUV disk observations of coronal dimming or wave onset. Thus, whilst sigmoidal features could clearly be associated with a high probability of flaring in this study, the association with CME onset was not confirmed. Furthermore, these authors did not state whether S-shaped morphology would be observed preferentially prior to or following CME onset. If sigmoid eruption were to follow the model proposed by Rust and Kumar [1996], the S (or reverse-S) shaped feature should be observed prior to, or in the early stages of, eruption. This appears to have been the case for some well documented events [e.g. Sterling et al., 2000; Thompson et al., 1999; Hudson et al., 1998]. However, the results described in this thesis will indicate that eruptions involving sigmoidal features do not always follow this pattern.

Chapter 4 of this thesis begins with an extension of the Canfield, Hudson and McKenzie [1999] study. The list of sigmoidal and eruptive active regions studied by these authors is compared with coronagraph data and EUV disk observations from the SOHO satellite together with ground-based Hα images. These data are evaluated in order to determine the accuracy of the sigmoid-to-arcade proxy in CME onset detection. Two example eruptive regions are discussed in detail in order to examine the difference between the eruption of a sigmoidal region thought to consist of a single structure and a region thought to appear sigmoidal as a result of projection effects acting on more than one feature. The implications of this study for CME onset prediction using soft X-ray data are discussed.

The Canfield, Hudson and McKenzie [1999] study, together with other recent observational studies of sigmoidal features [e.g. Pevtsov, Canfield & Zirin, 1996; Aurass et al., 1999; Wang et al., 2000; van Driel-Gesztelyi et al, 2000; Gibson et al., 2002], focused primarily on active region sigmoids. To date, no detailed studies into the nature of large scale sigmoidal features, unconfined by a single active region, have been carried out. Typical active region loop lengths are of the order of 10-100,000 km [Priest, 1982]. However, non-active region sigmoids may be several times longer than this upper value and can exist within regions of quiet-Sun or in the vicinity of diffuse flux systems, previously classified as active regions. Chapter 5 describes the formation and evolution of a sigmoid that developed within the decayed remnants of an active region. The

appearance of this region is studied over the course of three rotations leading up to the formation of the large scale sigmoid. The region's CME and flaring activity is also considered. CME activity is found to continue through all three rotations, even though flaring activity has almost ceased prior to the appearance of the large scale sigmoidal feature.

1.4.2: Transequatorial Loops

Transequatorial loops were initially observed in Skylab images of the solar corona [Chase et al., 1976; Svestka et al., 1977; Svestka & Howard, 1981]. Through analysis of Yohkoh soft X-ray observations between 1992 and 1998 Pevtsov [2000] found transequatorial loop systems (TLS) to be a frequent feature of the soft X-ray corona. This study identified several classes of interconnecting loop. Observations included loops that appeared sheared in S (or reverse-S) configurations and loops that appeared to form a magnetic X-point separating active regions in either hemisphere and undergoing reconnection [Tsuneta, 1996].

The Pevtsov [2000] study focused primarily on the frequency and morphology of transequatorial loop systems, rather than a connection between these loops and CME or flaring activity. Khan & Hudson [2000] observed a series of homologous disappearances of a transequatorial loop system. Each disappearance was associated with flaring and CME onset.

The results described in Chapter 6 of this thesis form the first survey of transequatorial loops in terms of their eruptive character. This study follows on from the Khan and Hudson [2000] study that considered a single eruptive transequatorial loop system. The study described in Chapter 6 considers a sample of 18 transequatorial loop systems. Comparison of soft X-ray TLS observations with white light coronagraph and EUV Fe XII (195 Å) disk observations from the SOHO/LASCO and SOHO/EIT instruments is made in order to determine how frequently transequatorial loop systems are involved in CME onset. The results of this study are then discussed in terms of the implications for transequatorial loop systems in CME onset prediction.

1.5 Summary

This thesis describes three completely new studies which aim to advance the understanding of sigmoidal features and transequatorial loop systems observed in the corona and their association with eruptive solar activity. This is achieved by:

(1) A survey of sigmoidal solar features in terms of their probability of eruption and association with CME onset. This study complements the previous work of Canfield, Hudson and McKenzie [1999] which classified sigmoidal features as eruptive in terms of their appearance in soft X-ray data alone. The survey described in Chapter 4 incorporates data from both the Yohkoh Soft X-ray Telescope (SXT) and the Solar and Heliospheric Observatory (SOHO). Detailed studies of two sample eruptive sigmoidal features are also included in this chapter.

(2) A detailed study of the formation and evolution of a large scale sigmoidal feature observed to form in the decayed remnants of an active region following CME onset. This constitutes the first study of a feature of this kind, the Canfield, Hudson and McKenzie survey having considered only sigmoids that formed in young active regions, closely associated with strong magnetic fields.

(3) The first survey of transequatorial loop systems in terms of their association with CME onset. This survey extends the results of Khan & Hudson [2000]. These authors found transequatorial interconnecting loop systems to be associated with CME onset in a single case study. The study described in this thesis extends this result to a list of 18 transequatorial loop systems (TLS), providing comparison between Yohkoh SXT and SOHO data in order to determine what proportion of the TLS are associated with CME onset.

The following Chapters 2 and 3 describe the instrumentation and data extraction techniques employed throughout this thesis. A description of each study can be found in Chapters 4, 5 and 6 respectively, and final conclusions in Chapter 7.

Chapter 2:

Solar Instrumentation

2.1: The Yohkoh Satellite

Yohkoh was launched on 30th August 1991. The satellite returned scientific data for a period of more than 10 years, finally ceasing operation on 15th December 2001. The Yohkoh satellite was a mission of international collaboration between Japan, the United States of America and the United Kingdom.

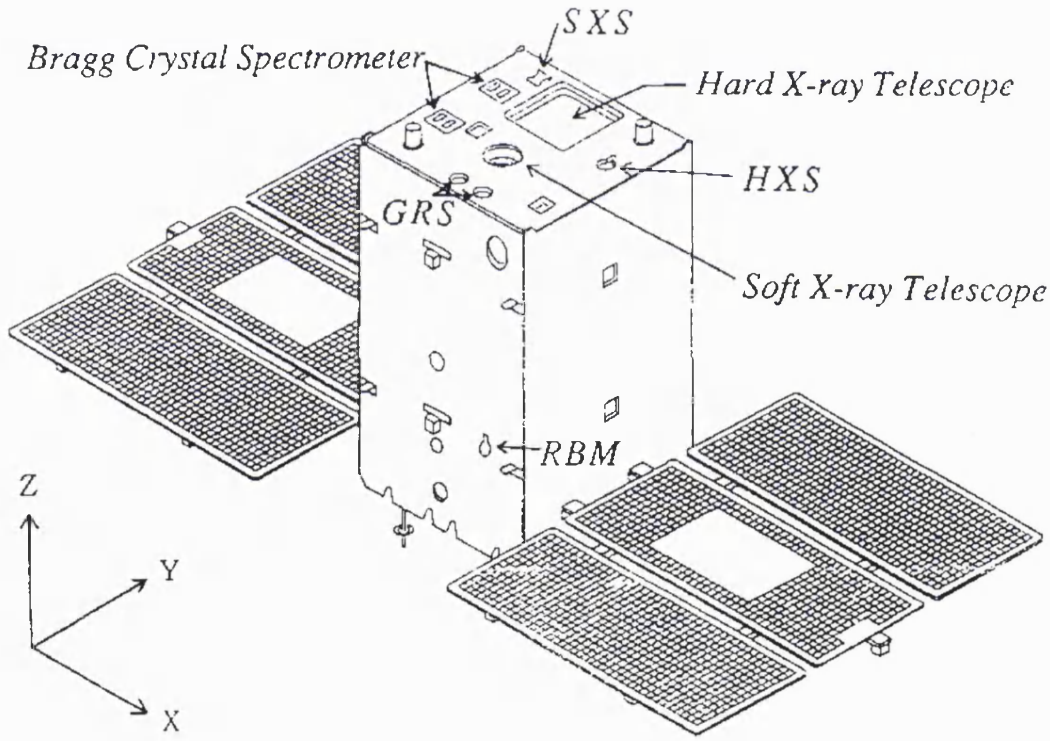

Figure 2.1: A schematic illustration of the Yohkoh spacecraft illustrating the orientation of each instrument. The Z-axis points in the sunward direction [Ogawara et al., 1991].

Yohkoh was primarily designed to study high-energy flare related phenomena through observations in the X-ray and γ-ray wavelength ranges. The scientific payload through which this was to be achieved consisted of four coordinated instruments:

- the Hard X-ray Telescope (HXT),
- the Soft X-ray Telescope (SXT),
- the Wide Band Spectrometer (WBS) and
- the Bragg Crystal Spectrometer (BCS).

The Soft X-ray telescope will be described in detail in Section 2.1.1. Figure 2.1 illustrates the orientation of these instruments with respect to the main body of the spacecraft.

Situated in an approximately circular orbit, with eccentricity 0.02, apogee 792 km and perigee 517 km during operation, the spacecraft orbited the Earth approximately 15 times per day with a period of 97 minutes. The low inclination of this orbit, at approximately 31°, resulted in the spacecraft spending about 40 minutes of each orbit in the Earth's shadow (referred to as spacecraft night throughout this thesis).

Further reduction in observing time arose from the passage of the Yohkoh spacecraft through the South Atlantic anomaly (SAA). Within this region, high densities of energetic particles are known to occur below 500 km. The WBS instrument onboard Yohkoh was equipped with a radiation belt monitor (RBM). Pointing perpendicular to the Sun-Earth line, this detected radiation levels in the vicinity of the spacecraft and was used to detect SAA crossings. During these crossings, high voltage supplies to the instruments were turned off in order to prevent damage.

Yohkoh was a 3-axis stabilised system. The coordinate system employed is illustrated in Figure 2.1: the Z-axis is directed towards the Sun with an estimated accuracy of 1" while the Y-axis points towards celestial north.

2.1.1 The Soft X-ray Telescope onboard Yohkoh

Designed to produce high-resolution images of the solar corona at X-ray wavelengths [Tsuneta et al., 1991], the Soft X-ray Telescope (SXT) was a glancing incidence telescope capable of producing X-ray images within the energy range 0.25 to 4.0 keV on a 1024x1024 CCD detector. Figure 2.2 illustrates the optical layout of SXT.

The telescope itself consisted of a sensor, a shutter, dual filter wheels and two co-aligned imaging elements: a mirror for X-rays and a lens for visible light.

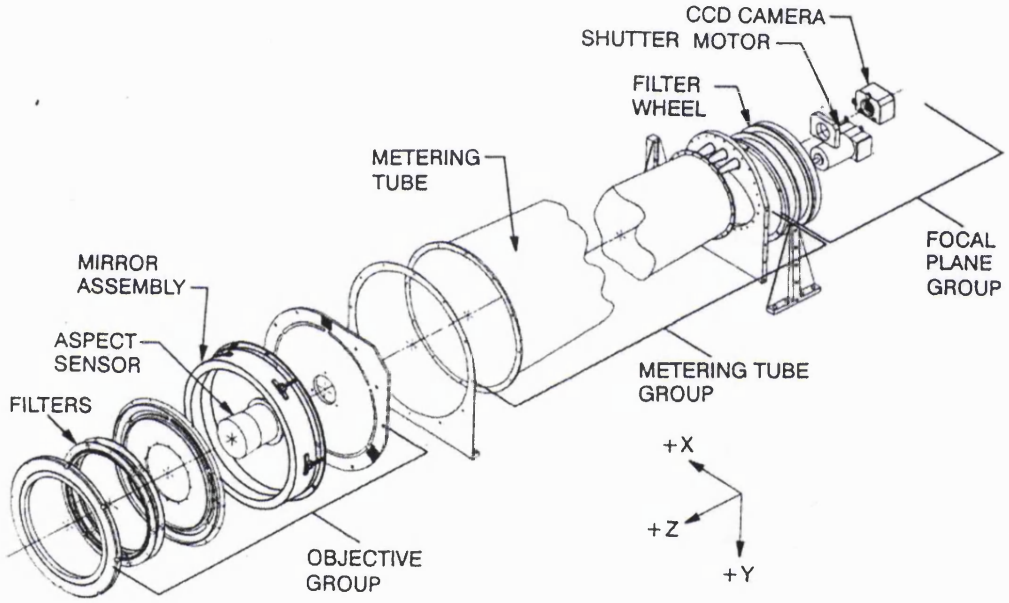

Figure 2.2: A Yohkoh/SXT exploded diagram illustrating the optical layout [Tsuneta et al., 1991].

The CCD detector pixel size corresponded to an angular size of 2".45. This was approximately equivalent to the angular resolution of the telescope. An angle of 42'x42' was subtended by the CCD, allowing full disk coverage in a single exposure. In order to conserve telemetry, on-chip pixel summation was frequently used. Angular resolution provided by each summation mode was 1x1 (2".45), 2x2 (4".9) and 4x4 (9".8). These are often referred to as full resolution, half resolution and quarter resolution respectively.

SXT data consists of two main types: full frame images (FFI) and partial frame images (PFI). Full frame images are usually available at a cadence of 2 to 10 minutes. Partial frame images (PFI) can comprise 64x64, 128x128 or 256x256 CCD pixels, depending on the level of on-chip summation used. Partial frames can be centred anywhere on the solar disk in order to observe flaring regions. During active periods, PFI data could be obtained at a maximum rate of 2 seconds per image.

Table 2.1: SXT filter wheel characteristics. The rear wheel held the X-ray analysis filters [Tsuneta et al., 1991].

Commanded Position	Front Wheel	Rear Wheel
1	Open	Open
2	30 Å at 4310 Å	Al 1265 Å
3	CCD flood lens	Al/Mg/Mn composite
4	Opal-glass diffuser	Be 119 μm
5	140 Å at 4580 Å	Al 11.6 μm
6	8.05% mesh	Mg 2.52 μm

Plasma temperature diagnostics are achieved through a selection of thin metallic filters. Located near the focal plane, these filters provided the ability to image different X-ray energies. Ordinarily, the front filter wheel would remain in the 'Open' position and the rear filter wheel would be rotated in accordance with a sequence table of observations loaded from the ground. Table 2.1 illustrates the possible filter settings for each of the two wheels. The rear wheel contained the X-ray analysis filters.

SXT images show solar plasma over a temperature range between approximately 2 and >50 MK. Figure 2.3a illustrates the SXT response in data numbers per second over this temperature range. Obtained by convolving the instrument response function with theoretical line spectra and continuum expressions, these curves assume an emission measure of 10^{44} cm^{-3}.

Charge read from the CCD detector pixels represents energy in photon flux integrated over exposure time rather than the actual number of photons (although if

photons were mono-energetic then these two values would be directly proportional). Charge is then converted into data numbers (DN). 1DN corresponds to detection of a single photon with wavelength 34 Å.

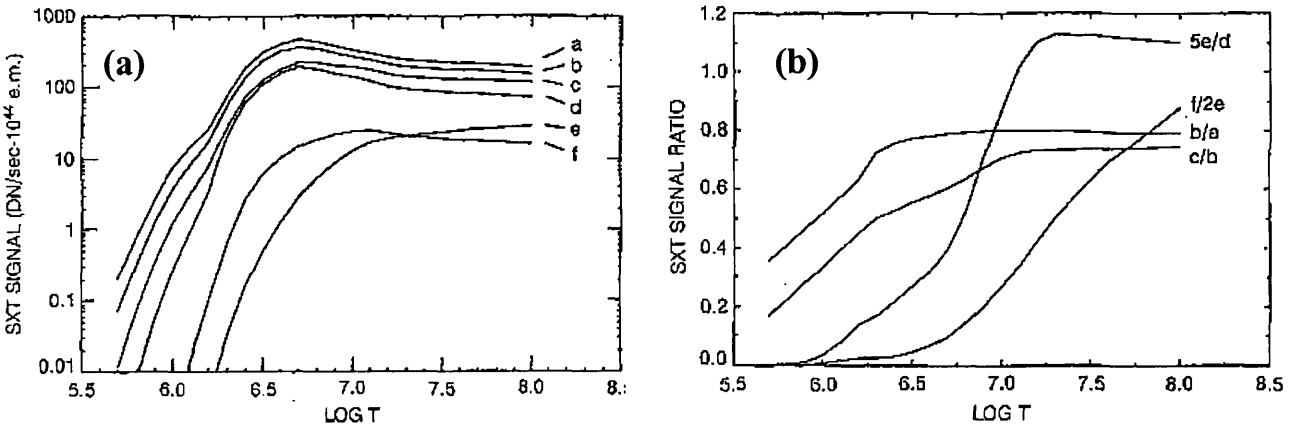

Figure 2.3a: Total signal is shown as a function of $\log_{10}T$ for the open filter case (a) and the SXT analysis filters (b) Al 1265 Å, (c)Al/Mg/Mn, (d) Mg 2.52 μm, (e) Al 11.6 μm, (f) Be 119 μm. **Figure 2.3b**: Ratio of the SXT response functions shown in Figure 2.3a. In cases (5e/d) and (f/2e), the signal measured using the Al 11.6 μm filter (e) must be multiplied by an additional factor of 5 or 2 to achieve the ratios illustrated here (Tsuneta et al., 1991).

Combining images taken using different SXT X-ray analysis filters allows derivation of temperature diagnostics [Hara, 1996]. Figure 2.3b illustrates filter signal ratios versus $\log_{10}T$ for selected pairs of analysis filters. A description of the technique used to derive temperature values from SXT filter pairs can be found in the following chapter.

Both Figures 2.3a and 2.3b illustrate that the filters can essentially be divided into three thin filters (Al 1256 Å, Al/Mg/Mn (referred to as AlMg throughout this thesis) and Mg 2.52 μm) and two thick filters (Al 11.6 μm and Be119 μm). Thicker filters are suited to analysis of flare temperature plasmas owing to their reduced sensitivity at lower

temperatures. Conversely, images taken using thinner filters are likely to show saturation in the event of a flare.

2.2 The Solar and Heliospheric Observatory (SOHO)

Launched on 2nd December 1995, SOHO [Domingo, Fleck & Poland, 1995] is a mission involving collaboration between ESA and NASA. The primary objectives of this mission centre around study of the solar interior, coronal heating mechanisms and the formation and acceleration of the solar wind.

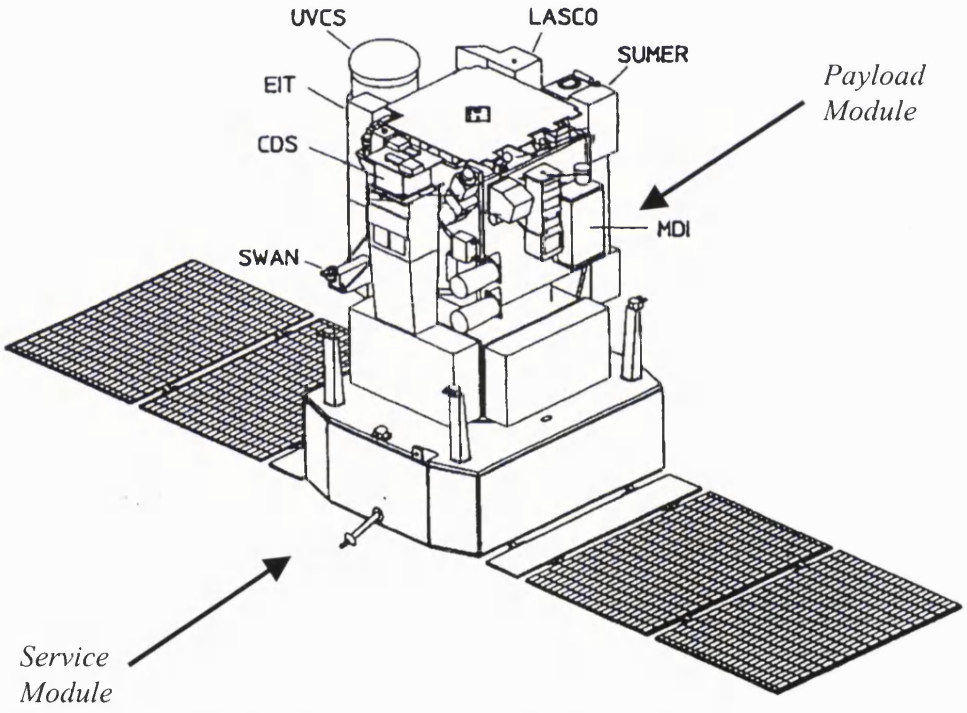

Figure 2.4: A schematic view of the SOHO spacecraft illustrating only the instruments dedicated to remote sensing of the solar atmosphere together with the SOI-MDI helioseismology investigation (adapted from Domingo, Fleck and Poland [1995]).

In order to achieve its objectives, the SOHO payload consists of twelve complementary instruments. These instruments are divided into three categories; helioseismology, solar atmosphere remote sensing and solar wind 'in situ' investigations.

A brief description of those dedicated towards remote sensing of the solar atmosphere can be found in Table 2.2.

Table 2.2: SOHO scientific instrumentation dedicated to remote sensing of the solar atmosphere, as illustrated in Figure 2.4.

Acronym	Investigation	Measurements
SUMER	Solar Ultraviolet Measurements of Emitted Radiation	Plasma flow characteristics of the chromosphere through to the corona.
CDS	Coronal Diagnostic Spectrometer	Temperature and density: transition region and corona
EIT	Extreme-ultraviolet Imaging Telescope	Evolution of chromospheric and coronal structures.
UVCS	UltraViolet Coronagraph Spectrometer	Electron and ion temperature, densities and velocities in the corona.
LASCO	Large Angle Spectroscopic COronagraph	Evolution of mass, momentum and energy transport in the corona.
SWAN	Solar Wind ANisotropies	Solar wind mass flux anisotropies and temporal variation
• SOI-MDI	Solar Oscillations Investigation – Michelson Doppler Interferometer	Primarily helioseismology. Also synoptic and high-resolution magnetograms.

- SOI-MDI is primarily dedicated towards helioseismology studies. A secondary objective is the production of regular high quality synoptic magnetograms. These provide an invaluable tool in understanding the structure and dynamics of the solar corona.

Data obtained by three of SOHO's twelve instruments (SOI-MDI, EIT and LASCO) will be used throughout this thesis. The following three subsections describe

each of these instruments in turn. Figure 2.4 illustrates the orientation of instruments onboard SOHO dedicated to remote sensing of the solar atmosphere along with the SOI-MDI helioseismology investigation.

The SOHO spacecraft is situated in a halo orbit about the Earth's L1 Lagrangian point (approximately 1.5×10^6 km upstream of the Earth). Figure 2.5 illustrates the SOHO orbit. The orbit has a period of 180 days with semi diameters of 200,000 km in the ecliptic plane in the Sun-Earth direction, 650,000 km in the ecliptic plane perpendicular to the Sun-Earth line and 200,000 km out of the ecliptic.

The L1 halo orbit is advantageous over Earth centred orbits as it affords a continuous, uninterrupted view of the Sun. It is also permanently outside the Earth's magnetosphere, thus allowing in situ solar wind measurements.

SOHO is 3-axis stabilised and pointing stability is better than 1" over 15 minute intervals.

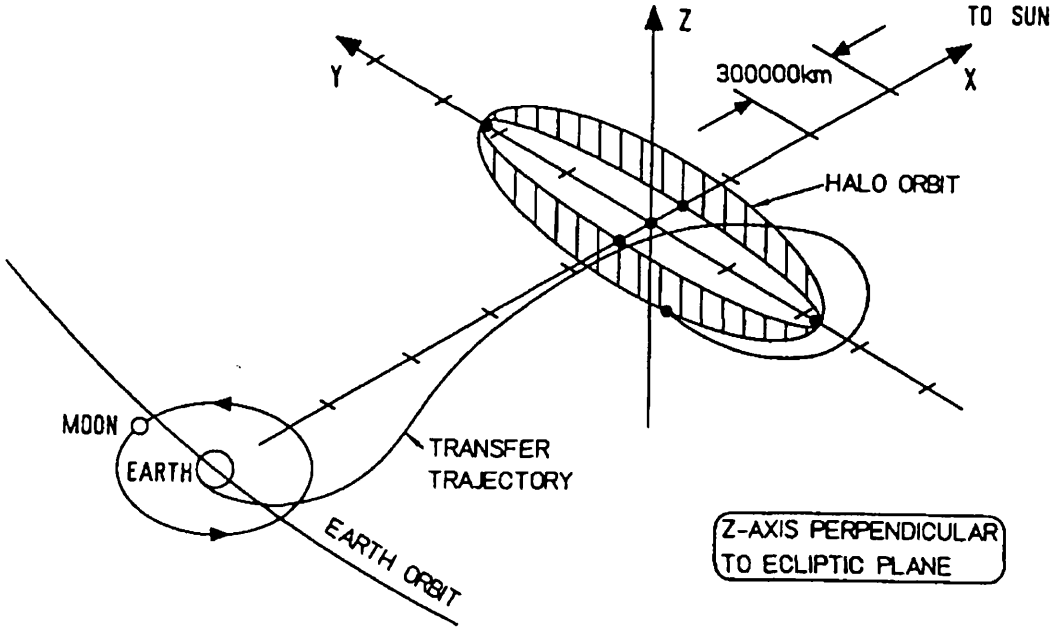

Figure 2.5: The SOHO halo orbit about the L1 Lagrangian point (from Domingo, Fleck and Poland [1995]).

2.2.1 The Solar Oscillations Investigation – Michelson Doppler Imager

The primary goals of the Solar Oscillations Investigation [Scherrer et al., 1995] centre around helioseismology measurements of the solar interior. However, the Michelson Doppler Imager (MDI) also makes non-helioseismic measurements of the line-of-sight magnetic field. This thesis will incorporate only the line-of-sight magnetic field measurements.

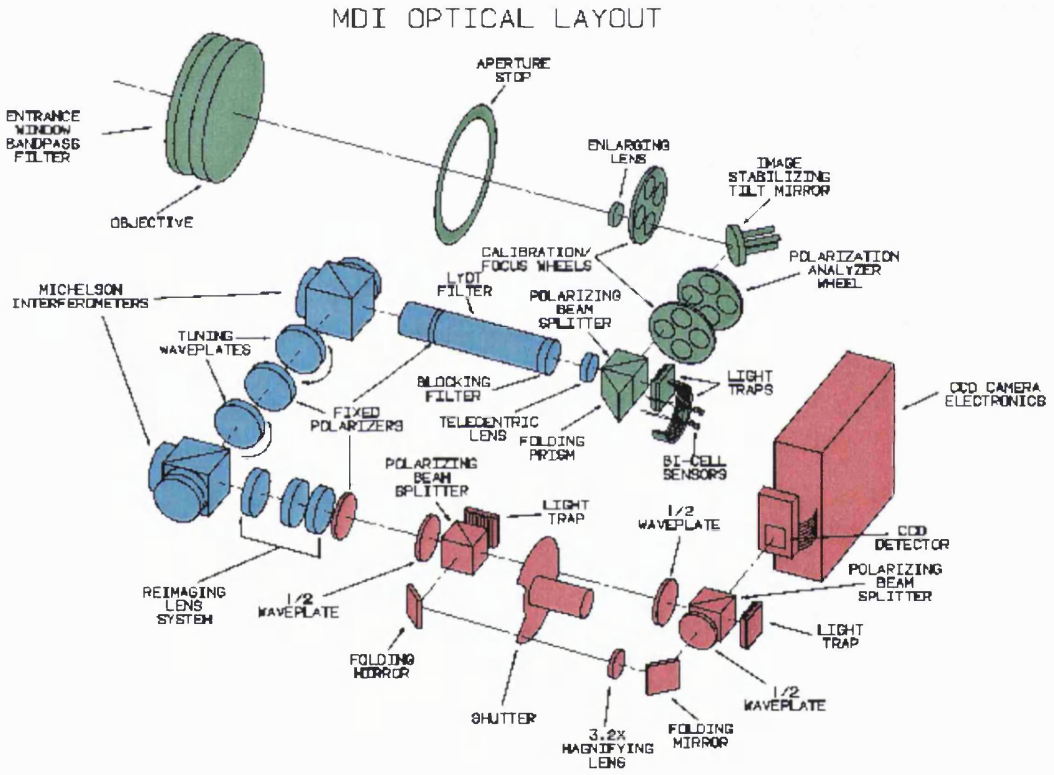

Figure 2.6: A schematic illustration of the SOI-MDI optical layout. Right and left hand polarisation can be selected through use of the filter wheels, shown here in green (from Scherrer et al. [1995]).

MDI uses a refracting telescope to feed sunlight through a set of increasingly narrow filters. A beam with 94 Å bandpass centred on the mid-photospheric Ni I 6768 Å solar absorption line is defined and incident onto a 1024x1024 pixel CCD detector.

Longitudinal magnetograms are constructed by measuring the Doppler shift separately in left and right hand circularly polarised light. The difference between these filtergrams provides a measure of the Zeeman splitting of the Ni I 6768 Å absorption line and is approximately proportional to the magnetic flux density. In the case of MDI magnetograms, flux density is defined as the line-of-sight component of the magnetic field averaged over a single pixel.

Figure 2.6 shows a schematic illustration of the MDI optical layout. Right and left hand polarisation can be selected through the use of filter wheels (represented by green in the figure).

MDI can operate in one of two modes: normal or high resolution. During normal observations, MDI makes synoptic observations of the line-of-sight magnetic field with 96 minute cadence. When operating in this mode, MDI pixel size corresponds to a resolution of approximately 2"x2" over a 34' field of view. When MDI is switched to high-resolution mode, the solar image is magnified by a factor of 3.2 prior to reaching the detector. This allows for an increased resolution of 0.625"x0.625" over a field of view 10.5'x10.5'. Both modes of observation have a combined instrumental and background noise level of approximately 20 Gauss. Five minute averaged full disk magnetograms are also available with a cadence of 96 minutes, having a correspondingly reduced noise level of approximately 8 Gauss [Meunier, 1999].

2.2.2 EIT: The Extreme-Ultraviolet Imaging Telescope

The primary objectives of the Extreme-ultraviolet Imaging Telescope [Delaboudinière et al., 1995] are the study of the dynamics and evolution of coronal structures over a wide range of timescales, sizes and temperatures, in order to gain new insights into the mechanisms responsible for coronal heating and solar wind acceleration. Through imaging the solar disk, EIT also allows study of the connection between coronal structures observed on the solar disk and those seen off-limb by the LASCO coronagraphs.

Full disk images of the transition region and the inner corona extending out to a radius of 1.5 R_o are made using EIT with a field of view 45'x45' and a pixel size of 2".6 which corresponds to the telescope's spatial resolution. In addition, on-chip pixel summation may be carried out (2x2 summation providing 5".2x5".2 per pixel resolution images and 4x4 summation leading to a resolution of 10".4x10".4 per pixel) in order to optimise the limited EIT telemetry and provide high cadence observations of a sub-region of the solar disk.

Capable of imaging solar plasma in the temperature range 0.06 to 3 MK, EIT produces images in one of four wavelength bands. Table 2.3 lists the four bands along with the peak temperature and main solar observational objectives.

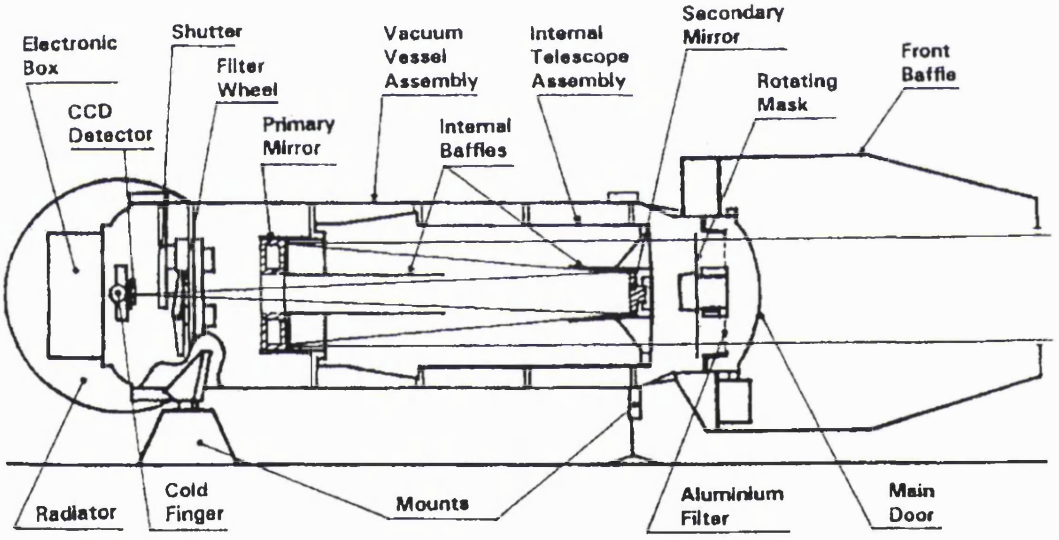

Figure 2.7: A schematic illustration of the EIT telescope indicating the major subsystems (from Delaboudinière et al. [1995]).

Observation in four separate wavelength bands is achieved through the use of multilayer normal incidence EUV optics. Figure 2.7 shows a schematic representation of the EIT optical arrangement. The telescope mirrors are divided into quadrants, each coated with alternating layers of molybdenum and silicon. Bandpasses are determined

through interference effects arising in the multilayer coatings. The coating applied to each quadrant may be tuned to define a specific, narrow temperature range. A rotating mask ensures that only a single quadrant is illuminated at any time.

Table 2.3: A list of the EIT bandpasses and the observational objective for each [Delaboudinière et al., 1995].

Wavelength	Ion	Peak Temperature	Observational Objective
304 Å	He II	8.0×10^4 K	Chromospheric network, coronal holes
171 Å	Fe IX-X	1.3×10^6 K	Corona/transition region boundary; structures inside coronal holes.
195 Å	Fe XII	1.6×10^6 K	Quiet corona outside coronal holes
284 Å	Fe XV	2.0×10^6 K	Active regions

Figure 2.8 illustrates the EIT temperature response, in units of DN (digital number) per second, determined for each of the four wavelength bands with the filter wheel in the open position. Emission measure is taken to be 10^{44} cm^{-3} and the gain is set such that one DN corresponds to detection of 18 electrons per CCD pixel.

Figure 2.8d shows the 304 Å bandpass response. In addition to the main peak at approximately 80,000 K, a second, slightly weaker, peak is observed at about 1 MK. The lower temperature peak is formed by the He II line at 304 Å and the higher temperature peak is a result of Fe IX at 171 Å and Si XI at 303.3 Å.

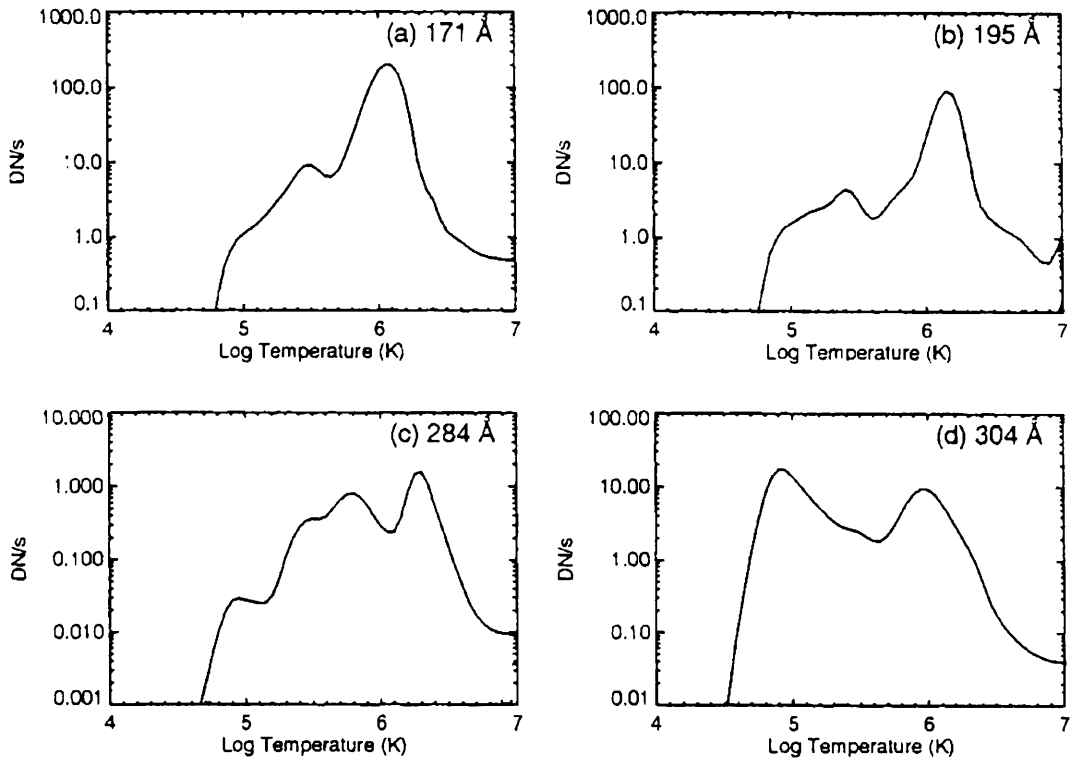

Figure 2.8: CCD signal (DN/s) as a function of source temperature from each EIT quadrant: (a) Fe IX/X 171 Å, (b) Fe XII 195 Å, (c) Fe XV 284 Å and He II 304 Å line. Figures assume solar emission measure of 10^{44} cm^{-3} (from Delaboudinière et al. [1995]).

2.2.3 The Large Angle Spectroscopic COronagraph (LASCO)

The Large Angle Spectroscopic COronagraph [Brueckner et al., 1995] is comprised of three individual coaligned coronagraphs, C1, C2 and C3. These coronagraphs jointly image the solar corona from 1.1-30 R_o.

This thesis incorporates data from the C2 and C3 coronagraphs only. Table 2.4 illustrates key system parameters of these coronagraphs. For further description of C1 the reader is referred to the LASCO instrument paper by Brueckner et al. [1995].

Table 2.4: System parameters for C2 and C3 [from Brueckner et al., 1995]. This table lists the field of view, pixel size and observable brightness range for each telescope.

	Field of View (R_o)	**Pixel Size**	**Brightness Range (B_o)**
C2	2.0*-6.0	11.4"	$2x10^{-7}$ to $5x10^{-10}$
C3	3.7-30.0	56.0"	$3x10^{-9}$ to $1x10^{-11}$

* the value of $1.5R_o$ quoted in the Brueckner et al. paper has since been found to be incorrect. A value of 2.0 R_o is now known to represent the inner limit of C2 more accurately.

Both C2 and C3 are externally occulted coronagraphs. Two main limitations exist in the design of this type of coronagraph. Firstly, the use of an occulting disk provides a minimum distance from the solar limb above which the corona may be observed (2.0 R_o in the case of C2). Furthermore, at the inner edge of the field of view, the imaging lens is shadowed by the occulter. This results in strong vignetting and reduces the spatial resolution of the inner corona. The second limitation, imposed by size constraints dictates that instrument apertures may not exceed a few cm. In the C3 case, a 110 mm opening (A0 in Figure 2.9) contains the centred occulting disk. This disk shields an entrance aperture (A1) of width 9.6 mm from direct sunlight.

The LASCO investigation is able to overcome the above limitations through the use of a nested set of three coronagraphs. The fields of view of these coronagraphs overlap such that spatial resolution is maintained over the whole range 1.1-30 R_o.

Figure 2.9 provides a conceptual illustration of the C2 and C3 telescope design. Figure 2.9a shows the path taken by coronal light as it is brought to a focus F. In each of the two telescopes, the external occulter (D1) shadows the entrance aperture (A1) from direct sunlight. The C3 occulter consists of three circular disks mounted on a common spindle, sized and spaced such that each intercepts diffracted light from the previous disk. The C2 occulter is a tapered cylinder with a finely polished screw thread that imitates multiple disks. These are each held in place by a pylon. This does not block the field of view, rather it provides characteristic distortion in the south-east quadrant of C2 and C3 data.

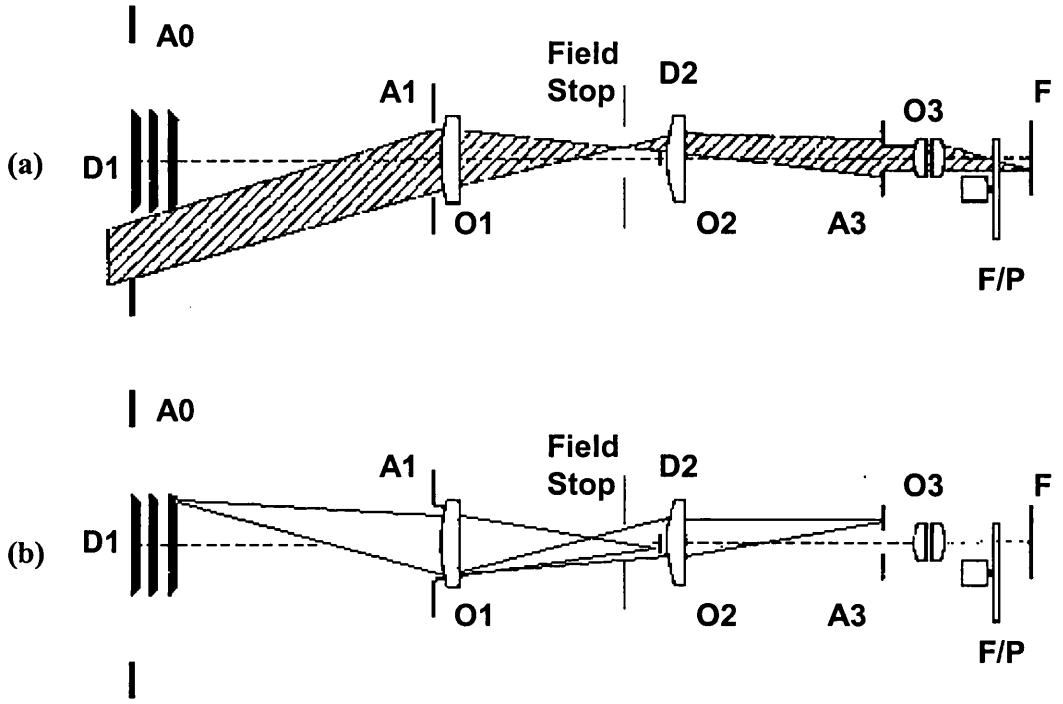

Figure: 2.9 A schematic illustration of an externally occulted Lyot coronagraph. Figure (a) illustrates the path taken by coronal light as it is brought to a focus F. Figure (b) depicts the removal of stray light. The front aperture A0, external occulter D1, entrance aperture A1, objective lens O1, internal occulter D2, field lens O2, Lyot stop A3, relay lens with Lyot spot O3, filter/polariser wheels F/P, and focal plane, F are shown (from Brueckner et al. [1995]).

The C2 and C3 coronagraphs are installed in one half of a rectangular instrument case 339.5x323x1362 mm with alignment of less than 60". Each coronagraph incorporates a 1024x1024 pixel detector having pixel size 21μm. Gain is set such that 1DN (digital number) is equivalent to between 15-20 photons per pixel incident onto the CCD. This is monitored by the onboard LASCO Electronics Box (LEB).

Both LASCO and EIT (see Section 2.2.2) are operated via the LEB where onboard image processing and compression takes place. Five different LASCO image sizes are produced by the LEB, depending on memory allocation: full image (1024x1024), ¼ image (512x512), 1/10 image (256x400), 1/16 image (256x256) and

1/64 image (128x128). The telemetry rate allocated to LASCO is 4.2 kbps. At this rate, transmission of a 1024x1024 image at 2 bytes/pixel would take in the order of 60 minutes. As a result, onboard compression is carried out by the LEB allowing transmission of several images per day [Brueckner et al., 1995].

2.3 Hα Observations

Observations in the Hα line, centred at 6563 Å, provide important information about the morphology and evolution of solar photospheric and chromospheric features.

The Hα data used throughout this thesis has been obtained from ground based observatories. Each ground-based observatory will only be in sunlight for some number of hours during the day. Therefore, in order to complement the satellite based observations of SOHO and Yohkoh, Hα data have been obtained from two ground-based observatories; each located in a different time zone:

- Big Bear Solar Observatory: Singer Full Disk H-alpha Telescope [PST: GMT-8]
- HIDA Flare Monitor Telescope [JST: GMT+9]

The BBSO Singer telescope uses a 0.5 Å bandpass Halle (Lyot) Hα filter to obtain images in the Hα line. The image resolution is approximately 1" per pixel. Data provided by BBSO for use in this thesis are in the form of Hα centre-line images with a cadence of 1 second.

Data supplied by the HIDA/FMT have resolution 4".5 per pixel and are available at a cadence of 1.5 minutes.

Chapter 3:

Data Analysis Techniques

3.1 Yohkoh SXT Analysis

SXT data is available at MSSL in the form of uncalibrated orbit files. Prior to analysis of this data, it is necessary to apply several corrections. These are carried out in a modular format using a standard routine supplied to the solar physics community entitled SXT_PREP. Corrections relevant to the work described in this thesis are:

- location of saturated pixels,
- data decompression,
- dark current removal,
- subtraction of the thin Aluminium (Al.126 μm) filter pinhole leak,
- correction for telescope vignetting,
- image alignment and formation of observing region where relevant in the case of partial frame data and
- exposure normalisation.

This routine also produces a measure of uncertainty in the prepared data arising from errors in the decompression, dark current subtraction and image alignment algorithms.

3.1.1 SXT Temperature and Emission Measure

The SXT analysis filters described in Section 2.1.1 each have slightly different bandpasses within the wavelength range 0.3-4.5 nm. This allows calculation of an approximate plasma temperature and emission measure by means of a filter ratio technique.

According to the SXT instrumental response, the energy of photons transformed into electron-hole pairs in the CCD detector during an exposure time δt_i is defined by:

$$E_i = \frac{\delta t_i \delta\sigma}{4\pi D^2} \int dl \int d\lambda \left\{ n_e^2(l) P[\lambda, T(l)] \eta_i(\lambda) \right\} \qquad \text{-(3.1)}$$

where D is the Sun-Earth distance, σ is the area of the Sun corresponding to 1 CCD pixel, i denotes one of five interchangeable analysis filters, η_i is the SXT effective area for filter (i), l is the line-of-sight path length and P[λ,T(l)] is the combined continuum and line emissivity.

An electron-hole pair is created with 3.65 eV of photon energy incident onto the CCD detector and the gain is set such that 1 DN~100 electrons. Therefore DN is related to Equation 3.1 as follows:

$$DN_i = \frac{E_i}{100x3.65eV} = \delta t_i \delta\sigma \int n_e^2(l) f_i[T(l)] dl \quad \textbf{(DN)} \qquad \text{-(3.2)}$$

where $f_i(T)$ is the temperature response of the telescope to an isothermal plasma at temperature T. Assuming temperature is homogeneous along the line-of-sight, this reduces to

$$DN_i = \delta t_i \delta\sigma EM f_i(T) \qquad \textbf{(DN)} \qquad \text{-(3.3)}$$

where $EM = \int n_e^2(l) dl$

Taking a ratio of normalised images in each of the two selected analysis filters i and j, illustrates the ratio's dependence on temperature alone:

$$R_{ij} = \frac{DN_i / \delta t_i}{DN_j / \delta t_j} = \frac{f_i(T)}{f_j(T)} \qquad \text{-(3.4)}$$

Temperature is then inferred by direct comparison of the measured ratios with the theoretical curves illustrated in Figure 2.3b. The corresponding plasma emission measure is derived from Equation 3.3 through substitution of the estimated temperature.

3.1.2 Estimation of Uncertainty in SXT Derived Temperature and Emission Measure

There are thought to be several sources of uncertainty in derived SXT temperature and emission measure values. These include both random and systematic errors, photon scattering and superposition of the line-of-sight corona [Tsuneta et al., 1997].

Systematic errors in temperature and emission measure arise from the instrument calibration. Porter and Klimchuk [1995] estimated these errors to be less than 28% and 71% respectively.

In addition, random errors arise from the statistical uncertainty of the incident photon distribution. Porter and Klimchuk [1995] estimated the influence of these errors to be less than 40% and 70% for temperature and emission measure calculations respectively.

Errors arising from poor photon statistics can be improved by summing consecutive aligned images taken using the same analysis filter over a period during which the soft X-ray profile of the structure does not change appreciably [Tsuneta et al., 1997].

3.1.2.1 Scattered Light

Another possible source of uncertainty in values derived from SXT data is scattering caused by micro-roughness of the grazing incidence mirrors. This leads to formation of a power-law wing of the SXT point spread function (PSF) [Tsuneta et al., 1997].

The scattering profile for X-rays is dependent on plasma temperature for broadband X-ray observations owing to the dependence of the point spread function (PSF) on wavelength and the X-ray spectrum being a function of plasma temperature [Hara, 1996; Hara et al., 1994].

The PSF has two main components: a gaussian core and a wing component which obeys a power law. The presence of this wing component leads to an increased background both around bright active regions and, to a lesser extent, over large distances. Hara et al. [1994] derived an expression for the wing component of the PSF using in-orbit observations of two flares (8th June 1992 and 6th September 1992). This was achieved by comparing a saturated full frame image taken at the beginning of each flare with partial frame images of higher time cadence and resolution. The PSF was found to behave as $r^{-2.00\pm0.01}$ for r>50", connecting smoothly to the core gaussian portion of the PSF measured prior to launch between r~20"-50".

The level of scattering in SXT is dependent on the wavelength of incident photons. Shorter wavelength photons lead to increased scattering. Hence, most scattering will arise from bright flare loops and the level of scattering will increase inside the limb.

3.1.2.2 Line-of-sight Corona

A third possible source of uncertainty in temperature and emission measure arises from the contribution of the line-of-sight corona to the image. Any temperature calculation for coronal plasma will consist of a temperature component for the flaring plasma and a second component arising from the non-flaring line-of-sight corona. The temperature component arising from the line-of-sight corona becomes important when the relative

emission measure of this background plasma is of the order of 50% of the plasma to be measured [Tsuneta et al., 1997].

It is assumed by Tsuneta et al. [1997] that the emission measure of quiet Sun regions is too low in temperature (~2 MK) to contribute significantly to the temperature analysis of flaring regions. Over the course of this thesis, temperature and emission measure analysis has been applied to regions of enhanced brightness following eruptive coronal activity only. It is therefore assumed that, in these cases, contamination from the line-of-sight corona is negligible in comparison to the other sources of error described above.

3.2 Coronal Mass Ejection Onset Identification

3.2.1 SOHO/LASCO Height-Time Extrapolation

In order to infer an approximate CME onset time and location, it is necessary to extrapolate coronagraph observations in space and time back to either a location on the solar disk, or a point on or above the solar limb. LASCO observations are available at a cadence of 20-30 minutes from the C2 coronagraph and approximately hourly from C3. This allows tracking of the CME path as the ejecta propagates through the corona between 2 and 32 R_o, or until the material has expanded such that the feature being tracked can no longer be clearly identified.

LASCO data is available via ftp from NRL (Naval Research Laboratories) and by request from the University of Birmingham. Level 0.5 data has been used throughout this thesis. At this level, data has been decompressed and rotated such that solar north points upwards. Prior to analysis, LASCO images are contrast enhanced by subtracting the background corona. A pre-CME image of the corona is subtracted from each image containing CME data [Plunkett et al., 1998].

Height-time data is then extracted from the resulting C2 and/or C3 movies by choosing a well-defined part of the CME, marking its location in the corona in each image and plotting radial distance as a function of time. The widget-based IDL routine

used to obtain this height-time data, titled wrunmoviem.pro, is a standard LASCO analysis routine. This routine incorporates a correction for image distortion which otherwise could alter the heights measured using this technique.

The feature used for tracking will vary according to the CME morphology. Examples include a bright front forming a CME leading edge or a bright core feature expanding away from the occulting disk.

A velocity is estimated by fitting either a linear or quadratic function to the combined C2 and C3 data depending on whether the CME appears to travel with a constant velocity or if it appears to accelerate.

An estimation of CME onset time is then achieved by extrapolating the observed height-time data to a location on the solar disk/limb. This location is determined in conjunction with SOHO/EIT 195 Å data, as will be described further in the following section. In order to locate possible CME sources on the disk a time window was selected for observation according to the estimated speed of the CME.

Since the CME material must initially start at rest with zero velocity, some initial acceleration is necessary prior to its appearance above the C2 occulting disk. Furthermore, since coronagraph observations in the range 1.5-6.0 R_o always show CMEs travelling at either constant speed or accelerating, it is thought unlikely that any deceleration occurs below the occulting disk [Harrison, 1990]. Some fast CMEs, rising with speeds in excess of 750 kms^{-1} may exhibit deceleration in and beyond the C3 field of view. This is thought to occur as the outward moving shock accompanying the CME sweeps up material from the background solar wind, leading to deceleration [Srivastava et al., 2000; Sheeley et al., 1999].

Initially it was decided to choose an onset window of length 10 hours. This follows Harrison [1991] who recommended the use of a long onset window in order to unambiguously identify activity associated with CME onset. This technique was employed for the purposes of the survey of sigmoidal active regions described in Chapter 4. However, following this study, it was decided that a 10 hour onset window was far in excess of that needed. For this reason, it was decided to define an onset window ending when the CME was first observed in the C2 field of view. The start time for this window

was estimated by first calculating the time that a CME, travelling at the velocity obtained using the height time extrapolation, would take to cross the disk and reach an altitude of 2.0 R_0. This time was then subtracted from the time at which the CME was first observed in C2 in order to give the start-time for the onset window.

The length of the predicted CME onset window can be expressed as follows:

$$\Delta t = \frac{2R_o}{v_{CME} \times 3600} \quad \textbf{(hrs)} \qquad \textbf{-(3.5)}$$

where Δt defines the length of the onset window in hours, v_{CME} is the estimated velocity of the CME, as described above, and R_o the solar radius. EIT 195 Å images of the solar disk were studied for this period. Images were studied in sequence, working backwards from the latest time within the onset window to the earliest. If no evidence of CME onset was observed during this period then the CME was assumed to have originated from behind the limb.

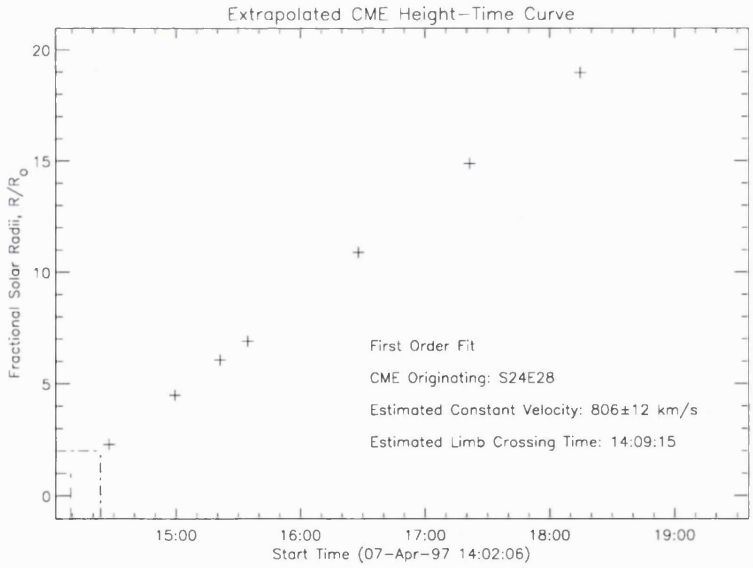

Figure 3.1: Height time data depicting a halo CME first observed by the LASCO/C2 coronagraph on 7th April 1997 at 14:27 UT. Dotted lines correspond to the solar limb

($1R/R_0$) and the C2 occulting disk ($2R/R_0$) respectively. See section 3.2.1.1 for a discussion of the uncertainties associated with this technique.

Figure 3.1 illustrates a sample height-time extrapolation for the halo CME of 7th April 1997. The event depicted in this figure is one example of the 'sigmoidal' active region survey described in Chapter 4. This event remains one of the best observed halo CMEs using both LASCO and EIT instruments [e.g. Berdichevsky et al. 1998; Thompson et al., 1999; Sterling & Hudson, 1997]. In order to produce the plot illustrated in Figure 3.1, the brightest leading edge of the CME was chosen. Figure 3.2 shows this expanding through the corona in a south easterly direction. The height-time extrapolation indicates that the leading edge travels outwards with a constant velocity of about 800 kms^{-1}. This is in agreement with the results of Berdichevsky et al. [1998].

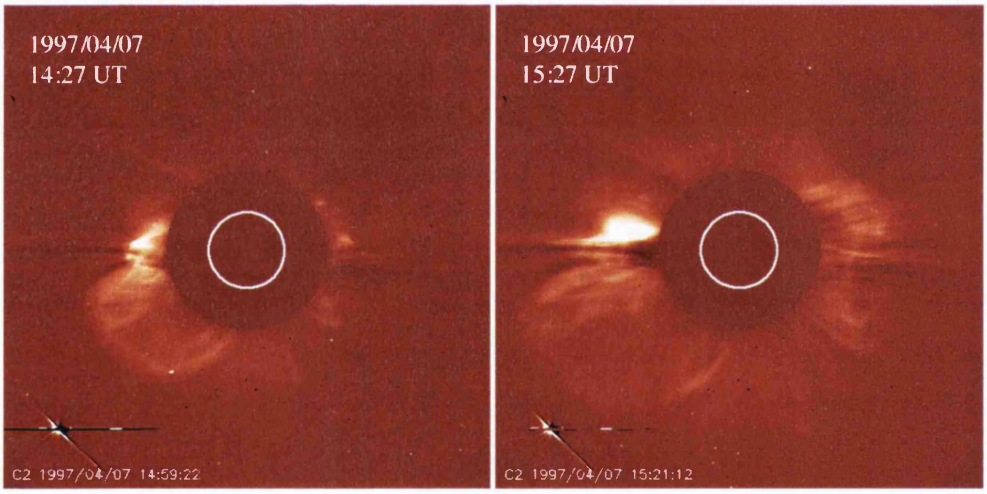

Figure 3.2: LASCO/C2 background subtracted images illustrating the outward propagation of the 7th April 1997 halo CME. Images correspond to the 2nd (14:27 UT) and 3rd (15:27 UT) points of Figure 3.1 respectively. Solar north points upwards and east to the left.

3.2.1.1 LASCO Height-Time Uncertainties

Uncertainties are introduced into the technique described above in a variety of ways. Random errors are introduced through measurement precision whereas systematic errors

are associated with the accuracy of these measurements. Sources of uncertainty include the choice of feature to be followed, precise tracking of this feature in a sequence of images and the placement of the cursor on the chosen feature. While a bright feature might be easy to track through the C2 field of view, the feature will become gradually more diffuse and increasingly difficult to follow as the feature expands through the C3 field of view. There may also be a jump between C2 and C3 data points owing to the difference in resolution of the C2 and C3 telescopes. Image resolution and exact pointing are expected to make a small contribution to the uncertainty

However, it is thought that, with practice, the precision with which measurements are made can be reduced to a minor issue in CME speed and onset time estimation [Lawrence & Young, 2001]. Lawrence [2002] estimated that although accuracy is difficult to quantify, the uncertainty introduced into a CME speed estimate through random errors is of the order of ±1% for a bright, well defined feature. For a fainter leading edge, indistinct beyond $15R_o$, an accuracy of ±3% should be achievable.

The uncertainty value quoted in Figure 3.1 is obtained using a weighted least squares fit. Weights are obtained by repeating the process of tracking a CME through the C2 and C3 coronagraphs several times. In this case, the estimate of 12 kms^{-1} is approximately ±1.5% of the estimated constant velocity. This agrees with the estimate of Lawrence [2002].

Measurement accuracy depends strongly on how the feature to be tracked is selected. Lawrence and Young [2001] illustrated that different users will select different features when tracking the same CME through the C2 and C3 fields of view. This can introduce uncertainties of up to ±25-30%. These authors also showed that the choice of curve fit often leads to a large variation in derived values.

The CME uncertainties quoted throughout this thesis reflect the precision of the measurements made and do not account for systematic errors that might result from different users' interpretation of the data.

3.2.2 EIT Observations of Dimming and Coronal Waves

EIT data is available via ftp from NASA Goddard Space Flight Centre (GSFC). Throughout this thesis level zero data has been used. Level zero data varies from QuickLook data as it has been reprocessed to include more information in the file header.

Prior to analysing EIT data, it is necessary to apply several corrections. This is achieved by means of a routine supplied with the SolarSoft IDL package named eit_prep. This routine provides the user with several optional corrections. For the purposes of the analysis described in the following chapters eit_prep was employed to:

- subtract dark current,
- provide flat field correction,
- remove the grid superimposed onto data by one of the telescope filters and
- exposure normalise images.

As described in the preceding section, EIT 195 Å data has been used throughout this thesis to gain information regarding the location and timing of activity associated with CME onset. In the case of localised EUV dimmings, full disk EIT 195 Å difference images are produced by subtracting a pre-event image from another taken during or after an event. Dimming regions are observed as localised depletions in emission.

Coronal EIT waves are observed using the techniques described by Thompson et al. [1999] and Wills-Davey & Thompson [1999]. Difference images are created by subtracting a pre-event image from all subsequent images. These difference images are then divided by the initial image to create a 'percentage difference' image. This represents the percentage change in emission between the reference and later images, and has the advantage that small fractional decreases in emission can be observed in weakly emitting regions at the same time as fractional brightenings [Thompson et al., 2000]. Figure 3.3 shows a sequence of four percentage difference images depicting the period surrounding the 7th April 1997 halo CME onset.

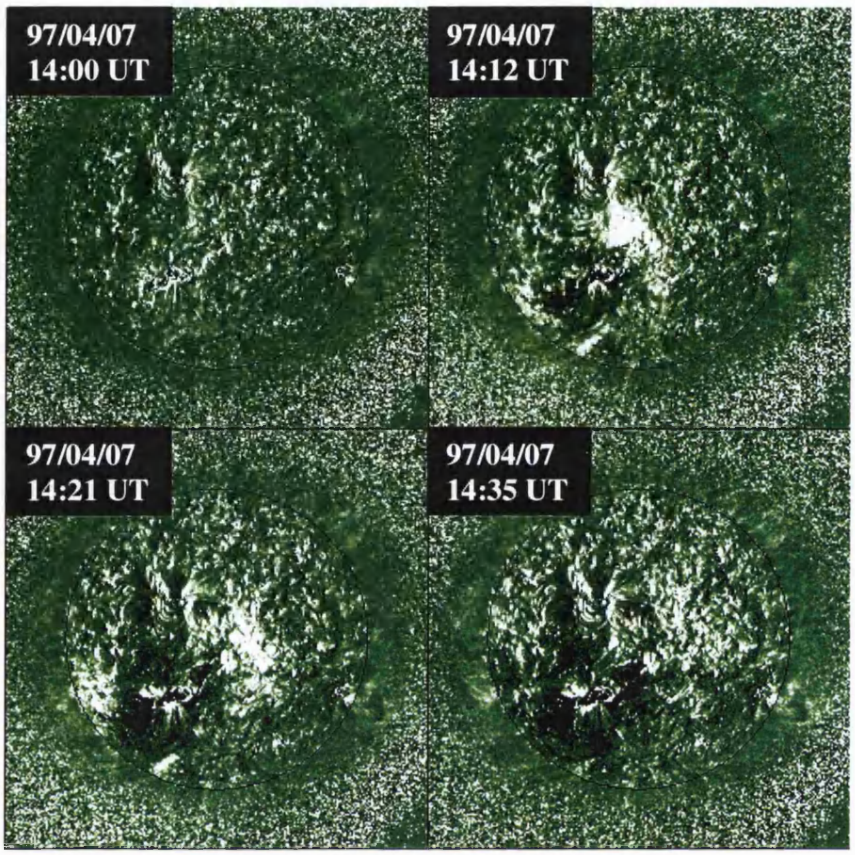

Figure 3.3: Percentage difference EIT 195Å images illustrating EIT wave onset in association with the 7th April 1997 event. The flare occurs to the south east of disk centre. The coronal wave is seen as a bright front followed by depletion in emission that expands away from the vicinity of the flare. Solar north points up and east is towards the left of the figure. Images are scaled to show ±20% changes in coronal emission

Chapter 4:

The Onset and Association of CMEs with Sigmoidal Active Regions

This chapter extends the study of Canfield, Hudson and McKenzie[1999] who considered sigmoidal active regions in terms of their association with CME onset. These authors studied only soft X-ray observations of sigmoidal active regions and used a 'sigmoid-to-arcade' proxy with which to infer CME onset. This chapter describes an extension of these results to include higher resolution soft X-ray data, white light coronagraph CME observations together with EUV and Hα disk observations in order to confirm CME onset. Active regions are reclassified according to their appearance in higher resolution soft X-ray data. Following reclassification, two sample eruptive regions are described in detail in order to determine whether regions reclassified into different categories erupt by means of the same processes.

4.1 Introduction

Viewed at soft X-ray wavelengths, coronal active regions are observed to consist of discrete bright loops that trace out magnetic field lines. These loops are often observed to collectively form S (or reverse-S) shaped features. Termed "sigmoidal" by Canfield, Hudson and McKenzie [1999], these features have frequently been referred to as the coronal manifestation of helically twisted flux tubes [Rust & Kumar, 1996]. Recent studies [e.g. Canfield, Hudson and McKenzie, 1999; Hudson et al., 1998] have found sigmoidal features to be associated with a high probability of eruption. In these cases, transient loop systems exhibiting overall S-like morphology are seen to evolve from a bright, sharp edged S-shaped feature into either an arcade of loops or a diffuse cloud.

Sterling and Hudson [1997] considered the disappearance of a sigmoidal feature on 7th April 1997 from Yohkoh Soft X-ray Telescope data [see Chapter 2 for a

description of Yohkoh/SXT]. Following eruption, this S-shaped feature was replaced by a previously unobserved cusp and two localised dimming regions. Hudson et al. [1998] extended this study to consider the coronal X-ray counterparts of 11 halo CMEs observed by the Large Angle Spectroscopic COronagraph (LASCO) onboard SOHO [see Chapter 2 for a description of the LASCO coronagraphs]. This study found that 7 of the total 11 CMEs showed on-disk eruptive signatures, four of which appeared to undergo "sigmoid-to-arcade" development. These authors described this development, observed in soft X-ray data, as occurring when "an S-shaped active region structure flares and transforms itself into a set of bright loops during the launch of a CME". They further suggest that the "sigmoid-to-arcade" development provides an on-disk signature of the standard CSHKP reconnection model for a solar flare (see Section 1.3.2.2). These authors suggest that the location of the post-event arcade or cusp footpoints may not correspond to those of the pre-flare structure, thus implying that plasma heating takes place on field lines which were not visible prior to eruption [Sterling et al., 2000].

The Sterling et al. [2000] study also considered SOHO Extreme-ultraviolet Imaging Telescope (EIT) [see Chapter 2 for a description of EIT] observations of sigmoidal regions associated with flaring and CME onset. EIT Fe XII (195 Å) data was used primarily for this study, having a peak temperature response lower than that of SXT at approximately 1.5×10^6 K. The authors noted that only a weak counterpart of the sigmoidal soft X-ray feature was visible in EIT data. These EUV-sigmoids were observed to become most prominent close to the peak in soft X-ray intensity associated with flaring and CME onset.

Further evidence for the association of sigmoidal features with CME onset was provided by Canfield, Hudson and McKenzie [1999]. This study considered Yohkoh/SXT observations of active regions visible on the solar disk during 1993 and 1997. These data were reviewed with the intention of clarifying which X-ray features possess the highest probability of eruption. Canfield, Hudson and McKenzie found active regions having an S (or reverse-S) shaped appearance to be most eruptive, through use of the "sigmoid-to-arcade" development as a proxy with which to infer CME onset. 51% of

all active regions were classified "sigmoidal". These sigmoidal regions accounted for 61% of all eruptions observed in soft X-ray data.

In order to account for the apparent spatial inconsistency between the location of the pre-flare sigmoid footpoints and those of the post-flare arcade, Sterling et al. [2000] speculated that overlying unsheared loops may be disturbed by the twisted flux rope as it begins to rise and erupt. The resulting reconnection of these loops would lead to heating, producing temperatures sufficient for these loops to be observed in SXT data. However, no evidence for this scenario was provided and these loops were not observed prior to eruption.

Several studies have shown that a magnetic flux tube may become unstable if the twist from one end to the other exceeds a critical value [c.f. Priest, 1982]. Pevtsov, Canfield and Zirin [1996] proposed that the twist possessed by individual pre-flare loops would combine on reconnection, causing the level of twist transferred to a larger post-flare sigmoidal feature to exceed the maximum threshold for stability. This would lead to the sigmoid becoming unstable and beginning to rise.

A number of authors [Moore et al., 2001; van Driel-Gesztelyi et al., 2000; Titov & Demoulin, 1999] have described a "sigmoid expansion" scenario by which an eruptive, transient sigmoidal feature is formed in association with flaring through reconnection of two j-shaped loops.

According to the "sigmoid expansion" model of van Driel-Gesztelyi et al. [2000], this upward motion drives magnetic reconnection between highly sheared arcade field lines primarily located beneath the flux tube. A long S-shaped field line is formed at the border of the flux tube. This joins the outer ends of two anti-parallel j-shaped loops which existed separately as part of the sheared arcade prior to activity commencing. Short loops are formed below, connecting the internal parts of the two pre-flare j-shaped loops. As reconnection proceeds, the flux tube becomes extended, eventually becoming insufficiently dense to be observed at SXT resolution. Consequently, the S-shaped loop will be observed to expand and disappear from view. Fast outward motion of the flux tube is thought to build a current sheet, of the type described by Kopp and Pneuman [1976] (Figure 1.8), below the outward moving feature. This implies that the newly

reconnected loops will adopt a cusp shaped appearance. This cusp shaped feature will gradually fade from view as the magnetic field relaxes [Forbes & Acton, 1996].

The above summary highlights some of the questions regarding the nature of sigmoidal features that have not yet been answered. Line-of-sight effects are important when observing disk features. It is therefore, often difficult to determine whether an apparently sigmoidal feature is comprised of a single feature or many individual features, oriented such that they appear sigmoidal in projection. This raises the question of whether a region should only be classified as sigmoidal if it comprises a single structure or whether 'projected sigmoids' should also be included in the definition. Previous studies have inferred CME onset using soft-X-ray data alone. While flaring can be clearly observed in this data, CME onset can only be inferred by proxy and observations may be misleading. Thus, the relationship between highly sheared structures and CME onset warrants further investigation.

This chapter begins with an extension of the Canfield, Hudson and McKenzie [1999] survey of sigmoidal active regions, incorporating active regions previously classified as both sigmoidal and eruptive over an increased range in wavelength. This extended survey incorporates white light coronagraph data, EUV and Hα disk observations together with increased resolution soft X-ray observations of the same regions. The aim of this extended survey is to clarify the relationship between the sigmoid-to-arcade development and CME onset.

Following the extended survey, two sample active regions are described in detail and comparison is made between the mechanisms involved in their eruption. These regions illustrate that S (or reverse-S) shaped features may appear in the corona as a result of differing magnetic field configurations. Consequently, the probability of their eruption is unlikely to be the same. The magnetic topology of each region is discussed in the light of current models. The implications of these observations in terms of CME onset prediction are then discussed.

4.2 Observations

It was decided to approach this investigation by extending the results of Canfield, Hudson and McKenzie [1999] to provide a more detailed study of those active regions classified as *sigmoidal* and *eruptive*. In addition to the soft X-ray proxy of a sigmoid-to-arcade development, the inclusion of SOHO based instrumentation allows confirmation of CME onset through white light coronagraph data together with EIT extreme-ultraviolet observations of on-disk onset signatures. A detailed description of this technique can be found in the preceding chapter.

In order to improve statistics and minimise the number of sigmoidal active regions interacting with adjacent structures, the Canfield, Hudson and McKenzie study considered active regions that formed during the years 1993 and 1997. Both years exhibit an intermediate level of solar activity. The SOHO mission was launched in 1996 and so extension of the Canfield, Hudson and McKenzie results to include comparison with SOHO data is only possible using the latter half of the initial list (active regions formed during 1997).

Hα data from the Big Bear Solar Observatory are also included in the extended survey. These data were available via the Yohkoh data archive at the rate of a single image per day. Active region prominences however, are frequently seen to erupt on a timescale of 20-30 minutes, often reforming later [Martin, 1998]. As a result, actual filament eruptions were rarely observed in the daily Hα images. Active region filaments could also be observed in absorption in EIT Fe XII (195 Å) data. Any changes to the filament observed using these data were recorded together with changes seen in Hα data. Filaments were classed as "eruptive" if their morphology appeared to change or if a full/partial disappearance could be observed following activity in the region.

The Yohkoh SFD videodisk used by the Canfield, Hudson and McKenzie study is composed of composite data with an average rate of approximately 50 images per day. The use of composite data compensates for the effects of saturation in the SXT images but the inclusion of only full disk data has the effect of degrading the image resolution to between 5" and 10" per pixel as compared with the maximum 2".45 per pixel resolution

[Rust & Kumar 1996; Tsuneta et al., 1991]. While this is undoubtedly advantageous when carrying out large surveys of data, short duration events (<1 hr) may be missed and detailed observation of sigmoidal active regions is inhibited. For the purposes of this investigation it was decided to repeat the original Yohkoh/SXT survey to include the full range of 9".8, 4".9 and 2".45 per pixel Yohkoh/SXT data where available.

Appendix A contains the list of 1997 "sigmoidal and eruptive" active regions identified by Canfield, Hudson and McKenzie [1999]. The estimated eruption times, provided by Canfield [1999] are also included in this appendix.

For the purposes of this study, the eruption and pre-eruption morphology of each active region previously classified as *sigmoidal* and *eruptive* were confirmed using SXT data of the highest available resolution. Comparison was then made between each of the eruptive events previously attributed to eruptive sigmoids and SOHO/LASCO CME data for that period. This was achieved by means of a LASCO height-time extrapolation, an example of which is illustrated in Figure 3.1. Each CME was traced back to eruptive activity on the disk, as described in Chapter 3. CMEs were only discounted if :

a) an exact origin other than that of the candidate region could be determined, or
b) if the time interval between observed event time and extrapolated CME onset time exceeded 10 hours (see Section 3.2 for more information regarding this choice).

CME onset was further confirmed through comparison with SOHO/EIT Fe XII (195 Å) observations. Whilst usually only a weak counterpart of the soft X-ray sigmoid is observed in cooler EUV data [Sterling et al., 2000], a dimming in the corona close to the active region is often observed in association with CME launch. Eruptive events may also be accompanied by a coronal EIT wave [Thompson et al., 1998]. Evidence of coronal waves and/or EUV dimming was searched for in order to provide an estimated onset location.

4.3 Sigmoidal Active Region Survey: Analysis

The initial survey published by Canfield, Hudson and McKenzie [1999] classified active regions as sigmoidal if either an S or reverse-S shaped configuration could be distinguished in the overall structure of the active region, as observed using Yohkoh SFD data.

The increase in SXT resolution to include full resolution (2".45 per pixel) partial frame data, where available, allowed a more detailed study of each active region to be carried out. Higher resolution observations illustrated that regions previously classified as sigmoidal and eruptive could be further divided into three categories in accordance with their appearance in full resolution (2".45 per pixel) SXT images:

a) active regions appearing to comprise a single S (or inverse-S) shaped feature prior to eruption,
b) regions found to comprise many smaller loops, the projection of which onto the solar disk causes them to appear sigmoidal at 5"-10" per pixel resolution, and
c) active regions not in possession of sigmoidal characteristics at increased SXT resolution.

Figures 4.1 to 4.3 show a sample active region from each of the three above categories. These regions illustrate the difference in appearance between sigmoidal, projected-sigmoidal and non-sigmoidal active regions observed at increased resolution.

Rust and Kumar [1996] measured the aspect ratio (length to width) of 103 sigmoids observed between 28th September 1991 and 4th November 1994. Under the force-free field approximation, these authors found the average value to be consistent with the observation of a twisted flux rope viewed in projection against the solar disk. Therefore, for the purposes of this study, category (a) active regions were classified sigmoidal since a single S (or reverse-S) shaped feature was observed within the region either prior to or during the eruption. Category (b), termed "projected-sigmoidal" defines

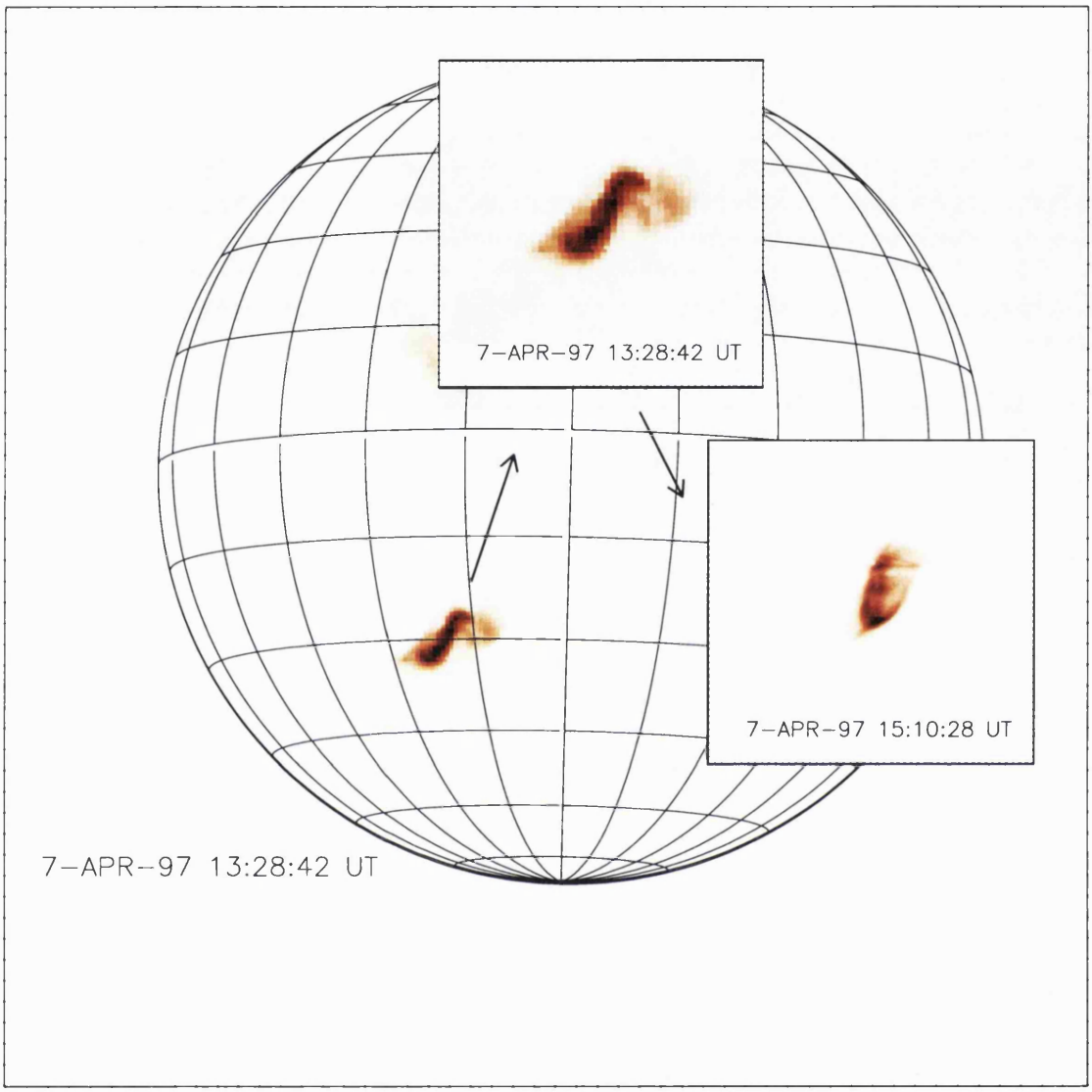

Figure 4.1 Yohkoh/SXT full and partial frame observations illustrating a sample active region from the reclassified *sigmoidal* category. This feature was observed to erupt, undergoing a sigmoid to arcade development with associated CME on 7th April 1997. Inset pre-event image indicates the sigmoidal feature at half resolution (4".9 per pixel) as no pre-event full resolution observations were made. The inset post-event image illustrates the appearance of a cusp shaped feature following eruption at full resolution (2".45 per pixel). In all cases solar north points up and east to the left. Images are reverse colour such that strongly emitting regions appear dark.

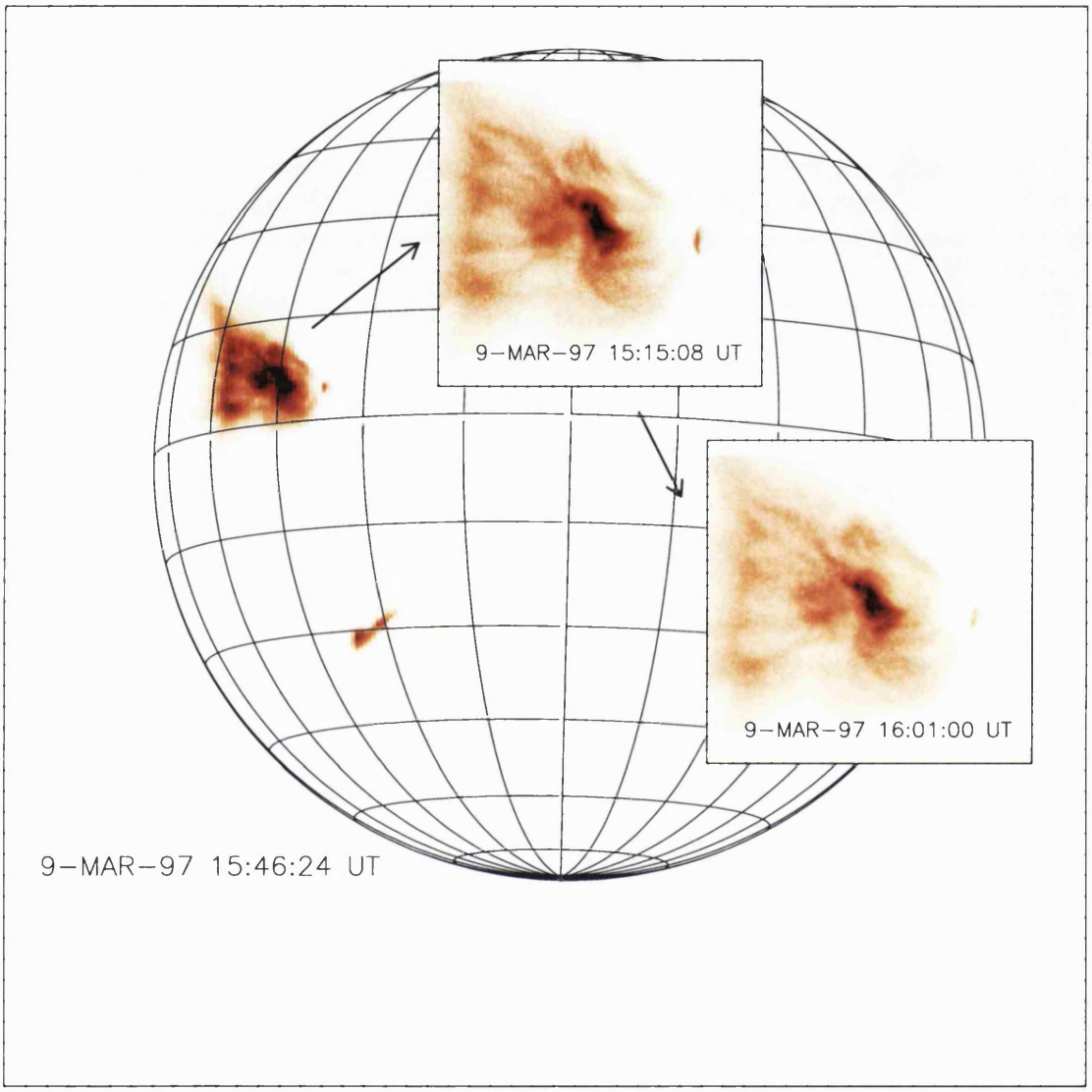

Figure 4.2: Yohkoh/SXT full and partial frame observations illustrating a sample active region from the *projected-sigmoidal* category. Inset images are both full resolution (2".45 per pixel). Both pre and post-event full resolution images illustrate an arcade of loops observed at an angle close to the east limb. These full resolution images illustrate that projection effects acting on this arcade of loops lead to the observation of a reverse-S shaped feature at lower resolution. Comparison of the inset images illustrates little/no change taking place within the arcade in association with CME onset. Solar north points up and east is to the left in each image. Images are reverse colour such that strongly emitting regions appear dark.

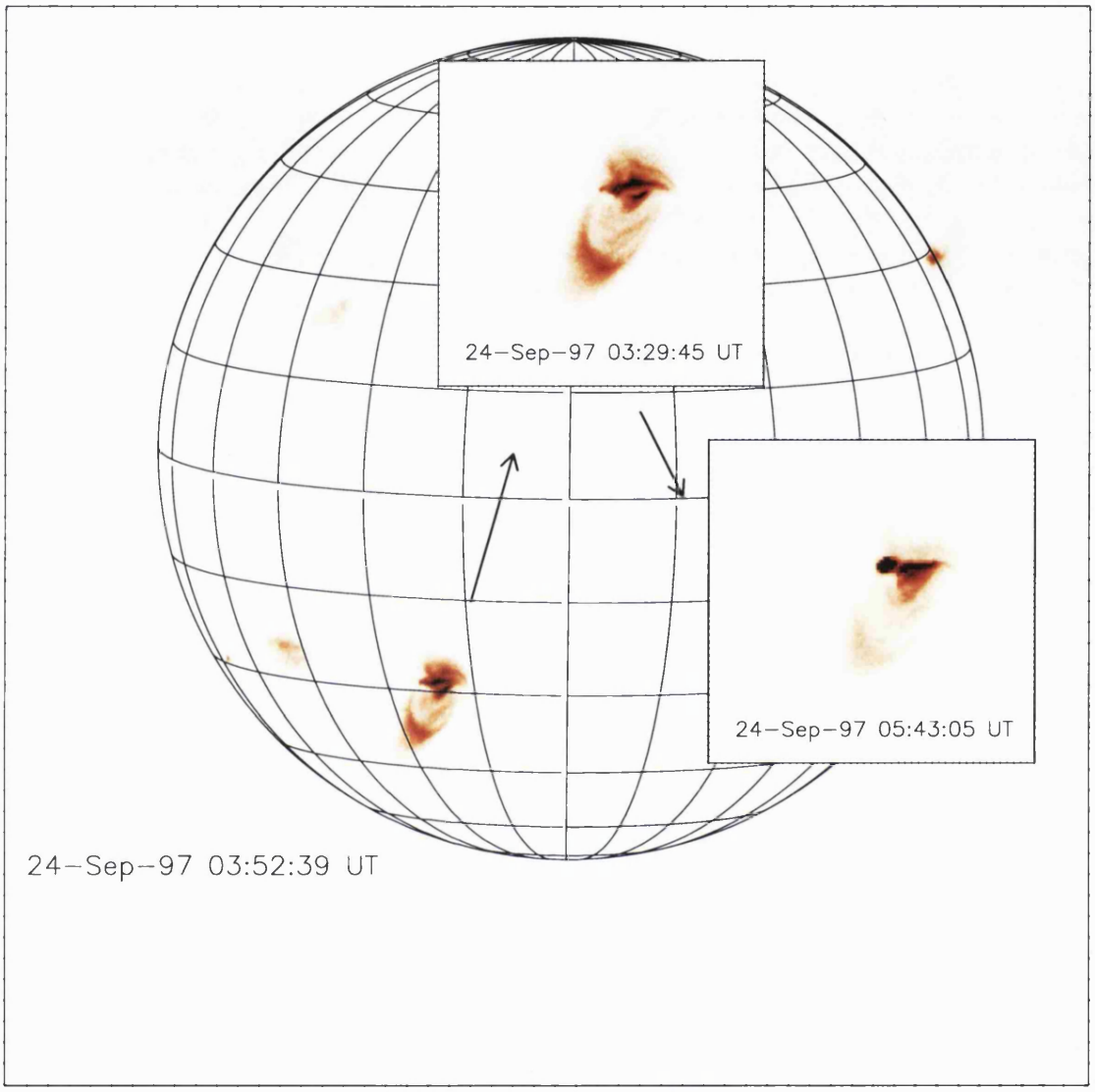

Figure 4.3: Yohkoh/SXT full and partial frame observations illustrating a sample active region from the *non-sigmoidal* category. Inset images are both full resolution (2".45 per pixel). These observations illustrate morphology changes in AR 8088 in association with flaring on 24th September 1997. A cusp shaped feature is already visible prior to flaring and is observed to form a connection between AR 8088 and 8087. Little change is observed in AR 8088 morphology as a result of flaring. Solar north points up and east to the left. Images are reverse colour such that strongly emitting regions appear dark.

regions also previously classified as "sigmoidal" as part of the Canfield, Hudson and McKenzie [1999] survey. However, observation at increased resolution found the sigmoidal appearance of these regions to be caused by the projection of a number of smaller soft X-ray features. Although brightenings did occur within these active regions, no continuous S (or reverse-S) shaped feature was observed in association with the eruptive event listed by Canfield, Hudson and McKenzie. While these active regions could certainly have been described as complex, observations did not agree with the concept of a single twisted flux rope. Accordingly, these active regions were classified separately.

Having repeated the soft X-ray survey using the full SXT dataset, comparison with other wavelength data was carried out. Tables 4.1 to 4.3 list the results of this comparison as applied to sigmoidal, projected-sigmoidal and non-sigmoidal active regions for which the full range of SXT, LASCO, EIT 195 Å and Hα data were available. "Y/W" denotes observed EUV dimming (Y) and coronal EIT wave (W) onset. "-" indicates either no dimming and/or EIT wave or no active region filament, depending on column.

Table 4.1: *Sigmoidal* Active Regions: Active regions appearing to comprise a single S (or reverse-S) shaped feature when observed at SXT full resolution (2".45 per pixel).

NOAA N°	Date	CME	Filament Eruption	EUV Dimming (195Å)
8027	07-Apr-97	Y	Y	Y/W
8032	17-Apr-97	N	N	-
8038	12-May-97	Y	N	Y/W
8090	05-Oct-97	N	N	-
8092	11-Oct-97	Y	Y	Y/W
8100	06-Nov-97	N*	Y	-
8108	19-Nov-97	N	Y	-

* denotes active region erupts to produce a CME several hours after the event time suggested by Canfield, Hudson and McKenzie [1999].

Comparison of Tables 4.1 to 4.3 with the results of Canfield, Hudson and McKenzie [1999] shows considerable difference in the number of active regions

exhibiting sigmoidal morphology. Of the initial 17 active regions, only 7 appear truly sigmoidal when observed using SXT full resolution data. Furthermore, comparison with LASCO and EIT data shows that only 6 of a total 17 active regions considered during this study are associated with CME onset. Only half of these regions are found in the reclassified 'sigmoidal' category.

Table 4.2: *Projected-Sigmoidal* Active Regions: Regions found to comprise many smaller loops when viewed by SXT at 2".45 per pixel resolution. The projection of these loops onto the solar disk causes them to appear sigmoidal when observed at 5"-10" per pixel resolution.

NOAA N°	Date	CME	Filament Eruption	EUV Dimming (195Å)
8015	04-Feb-97	N	-	-
8020	09-Mar-97	N	-	-
8026	03-Apr-97	N	-	-
8048	01-Jun-97	Y	-	Y
8096	20-Oct-97	N	-	-
8097	21-Oct-97	Y*	Y	Y/W

* denotes active region erupts to produce a CME several hours prior to the event time suggested by Canfield, Hudson and McKenzie [1999].

Table 4.3: *Non-Sigmoidal* Active Regions: Active regions not in possession of sigmoidal characteristics when viewed at SXT full resolution.

NOAA N°	Date	CME	Filament Eruption	EUV Dimming (195Å)
8056	25-Jun-97	N	N	-
8066	29-Jul-97	N	-	-
8088	24-Sep-97	N	Y	-
8103	11-Nov-97	Y	-	Y

In total, only 3 of the 7 reclassified sigmoidal active regions erupt in association with CME onset at the time quoted in Appendix A. Of a total 6 CMEs observed, 4 are seen to be associated with erupting filaments. Tables 4.4 and 4.5 together with Figure 4.4

provide an overview of the activity distribution with morphology for the present study. Dimming is observed in all regions associated with CME onset. Coronal waves are associated with all CMEs except one.

Table 4.4: Morphology and associated CME distribution for the reclassified sigmoidal, projected-sigmoidal and non-sigmoidal active regions.

	Sigmoidal	**Projected-Sigmoidal**	**Non-Sigmoidal**
CME onset	3	2	1
No observed CME onset	4	4	3
Total	7	6	4

Table 4.5: Morphology and eruptive filament distribution for the reclassified sigmoidal, projected-sigmoidal and non-sigmoidal active regions.

	Sigmoidal	**Projected-Sigmoidal**	**Non-Sigmoidal**
Eruptive Filament	4	1	1
Non-Eruptive Filament	3	-	1
Total	7	1	2

Tables 4.4 and 4.5 together with Figure 4.4 illustrate that whilst each of the active regions in question appears to be sigmoidal and eruptive at 5"-10" per pixel resolution, analysis using higher resolution data shows that this is not the case. Only 41% of regions initially classified as both sigmoidal and eruptive appear at increased resolution as though they might comprise a single twisted flux rope. These account for the highest proportion (50%) of observed CMEs. A further 38% of active regions, appearing sigmoidal as a result of projection effects rather than a single twisted structure, account for 33% of the observed CMEs. The remaining 24% of active regions have no visible sigmoidal characteristics and account for the remaining 17% of the observed CMEs.

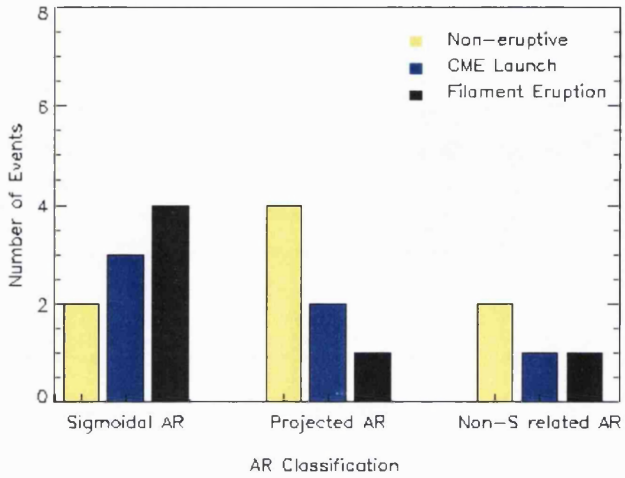

Figure 4.4: Distribution of events in terms of active region classification and activity. Non-eruptive events are associated with neither CME onset nor filament eruption. Reclassified sigmoidal active regions are associated with the highest probability of both CME onset and filament eruption. This is followed by the projected-sigmoidal category and finally, non-sigmoidal regions.

Although reclassification from 100% sigmoidal into the above categories has resulted in each category containing only a small number of cases, active regions showing a clearly defined S (or reverse-S) shaped soft X-ray structure do appear to be associated with the highest probability of CME onset.

4.4 Comparison of sample eruptive *Sigmoidal* and *Projected-Sigmoidal* Active Regions

The following sections describe two sample active regions taken from the extended survey of sigmoidal active regions. One active region is selected from each of the 'sigmoidal' and 'projected-sigmoidal' categories, each showing evidence of eruptive activity. Comparison is made between the S (or reverse-S) shaped feature visible in each of the two active regions and the mechanisms involved in the eruption of these features.

4.4.1 NOAA AR 8092: 11-Oct-97 Event, A Sigmoidal Active Region.

Previously classified as both sigmoidal and eruptive by Canfield, Hudson and McKenzie [1999], this active region was selected for use as an example of the reclassified *sigmoidal* category listed in Table 4.1 owing to its clear S-shaped appearance and evidence of eruption. This evidence included CME onset, EIT wave onset, EUV dimming, soft X-ray and EUV morphology change. Only one other active region in this category possessed all these characteristics. This was the 7th April 1997 eruptive sigmoid event which has already been the subject of several studies [e.g. Sterling et al., 2000; Zarro et al., 1999; Hudson et al., 1998]. Therefore, NOAA AR 8092 was selected for the purposes of this discussion in order to analyse an alternative region.

Brightening located toward the centre of the active region was initially observed in Yohkoh/SXT data at 08:44 UT on 11th October 1997. Flaring was first observed detected at 08:51 UT by both SXT and EIT 195 Å as shown in Figures 4.5 and 4.6. Following the event, both soft X-ray and EIT 195 Å data illustrate the formation of an arcade with its axis approximately perpendicular to the active region neutral line. This arcade appeared in place of the pre-flare structures, which had been approximately aligned with the neutral line. Therefore, it provides evidence of reorganisation within the active region, in line with the Kopp-Pneuman reconnection model for an eruptive flare [see Chapter 1, Figure 1.8]. Expanding CME material was first observed in the LASCO/C2 coronagraph at 10:28 UT. Use of a height-time extrapolation indicates CME onset consistent with activity in AR 8092.

The GOES light curve corresponding to the period of activity in AR 8092 is shown in Figure 4.7. Unfortunately, a data gap led to classification of this event as a B4.8 flare. Observation of X-ray flux before and after this gap is suggestive of a larger event.

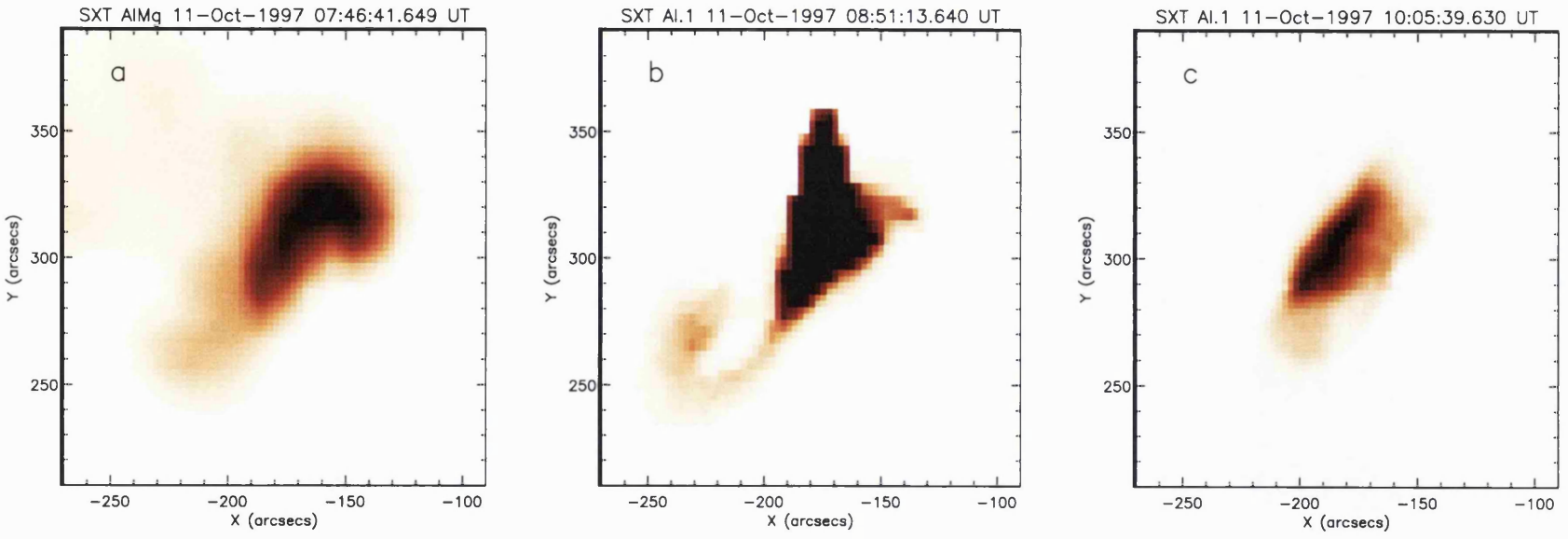

Figure 4.5 Yohkoh/SXT images of NOAA AR 8092 illustrating morphology changes during eruption on 11th October 1997. Figure (a) illustrates the presence of j-shaped loops prior to eruption. This image was taken prior to flare mode triggering and consequently has lower resolution of 4".9 per pixel. Figure (b) illustrates the appearance of an S-shaped feature following flare onset. Figure (c) illustrates the appearance of a post-event arcade of loops. Figures (b) and (c) were taken whilst Yohkoh was operating in flare mode and therefore each has resolution 2".45 per pixel. Dark rectangular structures seen towards the center of the active region in Figure (b) represent saturation of the CCD during the flare and do not represent real features. Images are displayed in reverse colour such that strongly emitting regions appear dark.

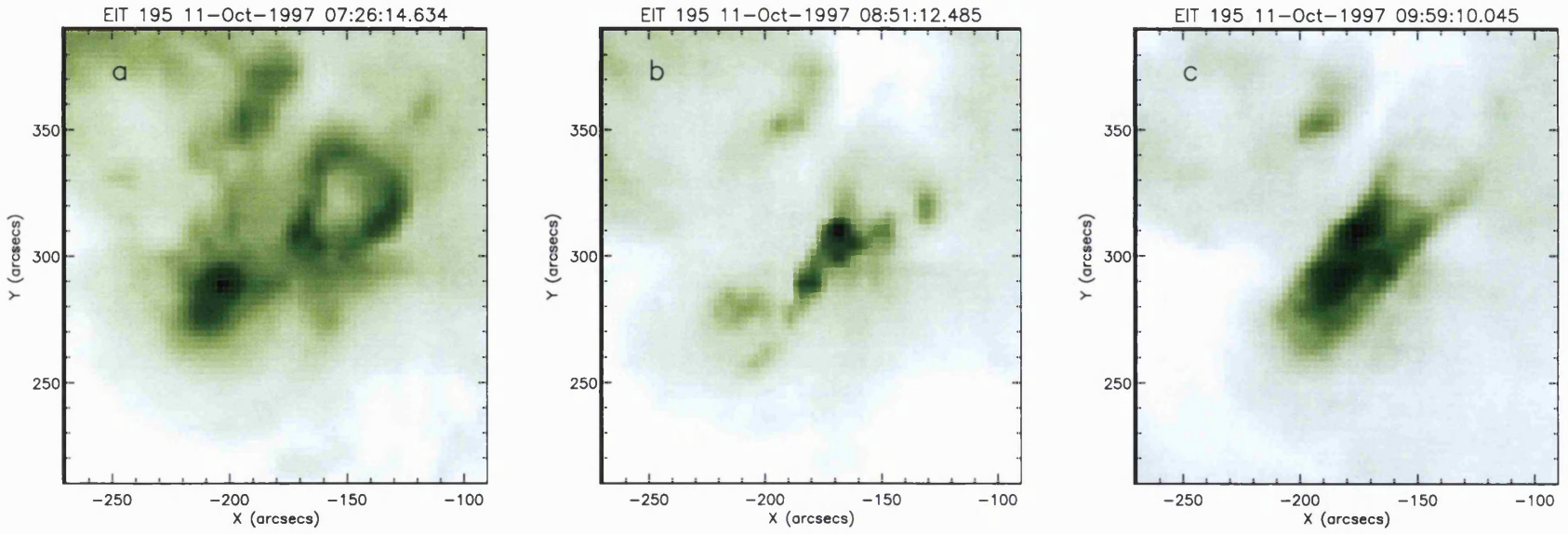

Figure 4.6: EIT Fe XII (195Å) images illustrating active region 8092 morphology change as a result of the 11th October 1997 eruptive event. (a) illustrates pre-flare configuration, (b) illustrates brightening between two adjacent j-shaped loop systems and (c) shows the post-eruption arcade. The resolution in each case is 2".5 per pixel. Images are displayed in reverse colour such that strongly emitting regions appear dark.

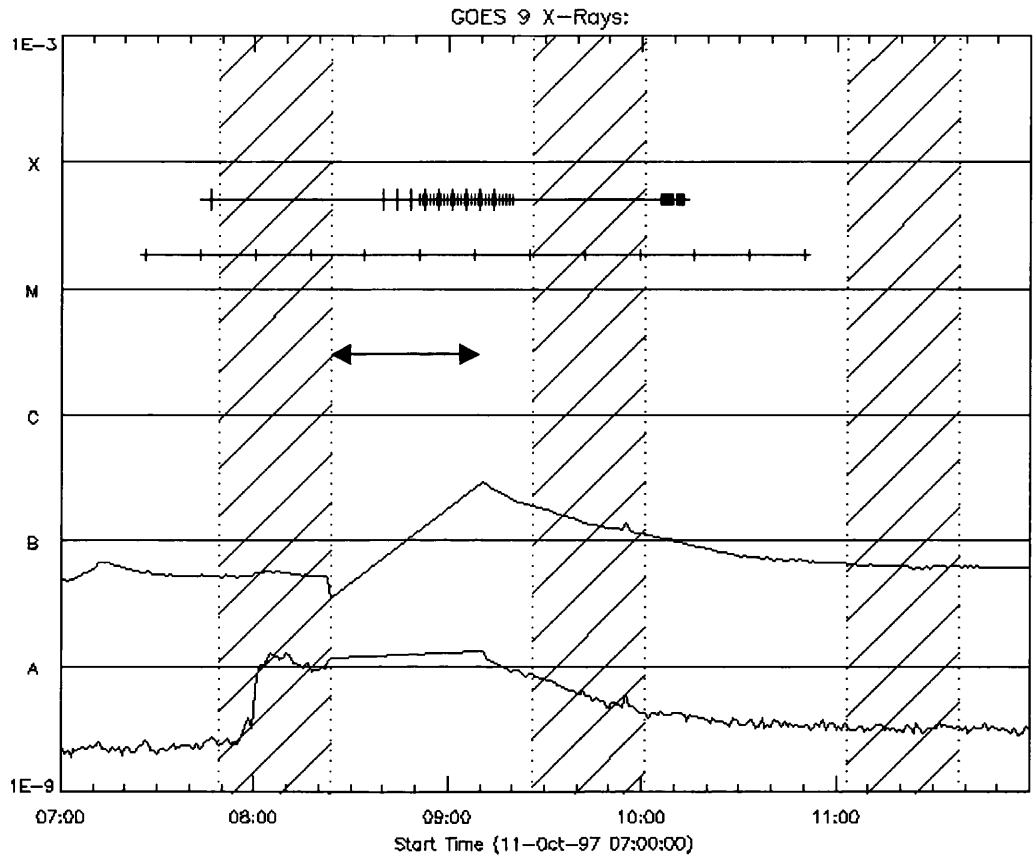

Figure 4.7: GOES 1-8 Å light curve for the period surrounding eruption of AR 8092 on 11th October 1997. Shaded areas represent periods of Yohkoh spacecraft night. The red horizontal line indicates SXT exposure times (short ticks denote partial frame observations and long ticks denote full frame). The green horizontal line indicates SOHO/EIT Fe XII (195 Å) exposures. An arrow indicates the GOES data gap during the flare.

A coronal wave was initially observed in EIT Fe XII (195 Å) images of the AR 8092 at 08:51 UT. This coincided with EUV brightening observed above the neutral line at a point separating the two pre-flare loops, as shown in Figure 4.6b. Unfortunately SXT images of this period show saturation towards the centre of the active region, making it only possible to observe the location of this brightening at the lower temperature response of the EIT Fe XII filter.

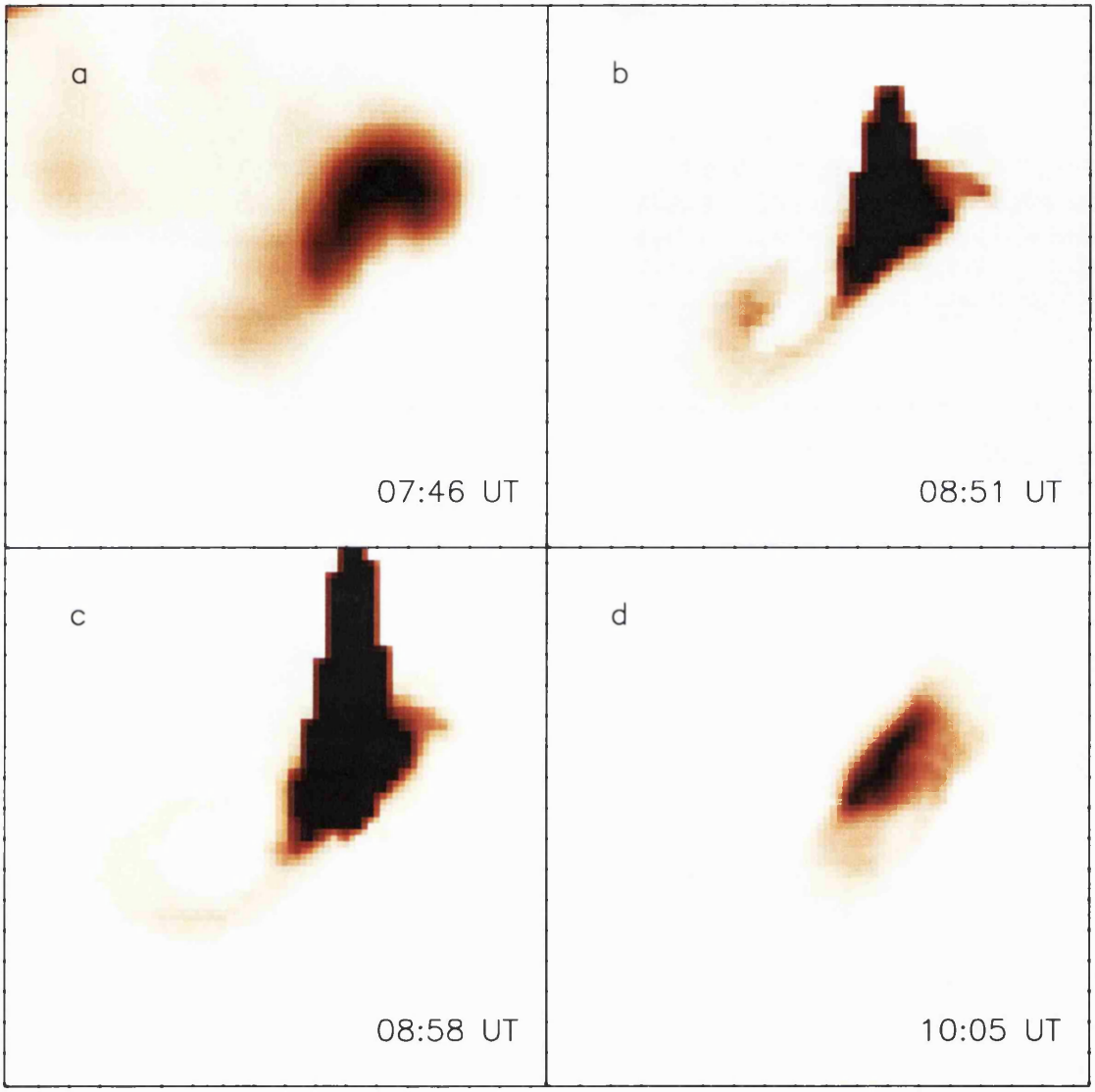

Figure 4.8: Yohkoh/SXT observation of expanding loops in AR 8092. Figure (a) represents the pre-flare bipoles. Loop expansion is observed to the south east of the active region in Figures (b) and (c). Figure (d) illustrates the unsheared post-flare arcade. Figure (b), (c) and (d) are full resolution (2".45 per pixel) images taken during flare mode, while (a) is half resolution (4".9 per pixel), included as no full resolution observations were made prior to flare mode triggering. Solar north points up and east to the left in each case. Images are reverse colour such that strongly emitting regions appear dark. Figures (b) and (c) clearly show the effect of CCD saturation towards the centre of the active region. This appears as dark triangular features in each case.

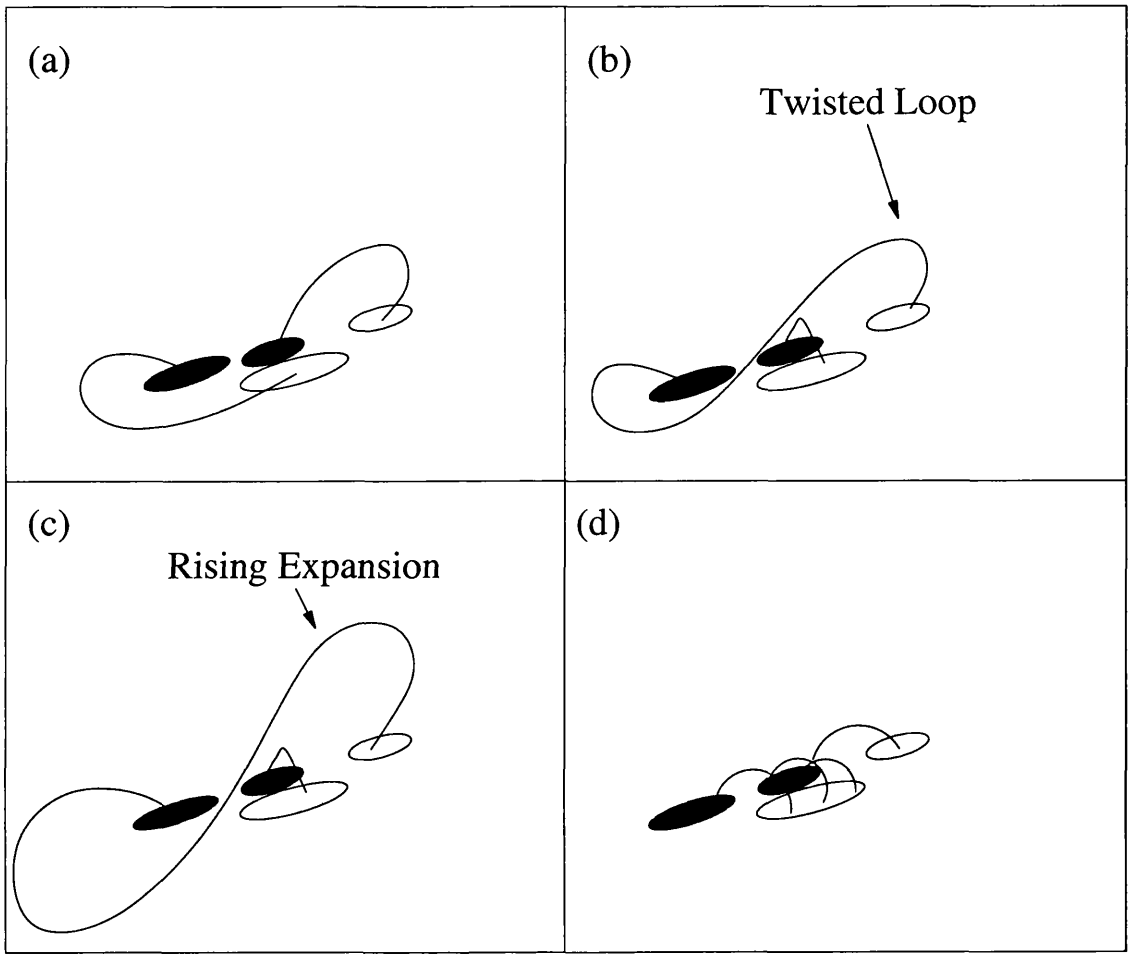

Figure 4.9: Schematic illustration of the AR 8092 core field behaviour during the ``sigmoid expansion" scenario thought to take place within AR 8092. Sheared pre-flare loops (a) reconnect to form a twisted loop (b). This unstable loop rises (c) and causes eruption of the field below leaving behind a post-flare arcade in possession of reduced shear (d).

Figure 4.8 illustrates full and half resolution SXT data for this period. These images show the expansion of S-shaped loops in a south-easterly direction. This expansion takes place during the period 08:54 – 08:59 UT. Following the disappearance of these loops, an unsheared arcade is observed to form in both SXT partial frame and EIT Fe XII (195 Å) data (Figures 4.5c and 4.6c respectively).

The expansion illustrated in Figure 4.8 is suggestive of reconnection taking place between two j-shaped loops to form a single, twisted structure and shorter, untwisted loops below. This follows the expanding sigmoid model of van Driel-Gesztelyi et al. [2000]. Figure 4.9 provides a simple illustration of the reconnection scenario undergone by the core field in association with eruption.

Later observations show a post-flare arcade aligned approximately perpendicular to the active region neutral line. This suggests that the lower loops, situated beneath the rising sigmoid, erupt in the manner described by Kopp and Pneuman [see Chapter 1, Figure 1.8].

Although few changes to the MDI magnetogram observations of AR 8092 are observed during the event itself, earlier magnetograms illustrate that the active region is decaying. White light observations show that there are no sunspots associated with the region at this time. Magnetogram observations shown in Figure 4.10 illustrate footpoints beginning to coalesce and strengthen just prior to eruption. In the hours following eruption, these footpoints weaken with the emergence of new flux to the north-east of the active region.

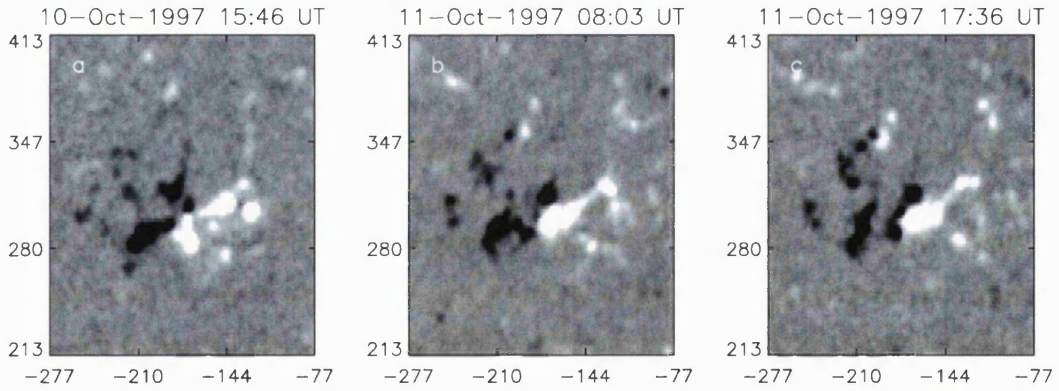

Figure 4.10: SOHO/MDI magnetogram data taken during the period of 34 hours surrounding eruption of AR 8092 on 11th October 1997. Observations have a resolution of 2" per pixel and illustrate changes in the photospheric field including footpoint coalescence, before and after the time of eruption. Axes are labeled in arc-seconds. Black denotes magnetic field oriented towards the photosphere whereas white denotes magnetic field directed towards the observer.

Finally a linear force-free field (LFFF) extrapolation [Brown, 1999] was applied to SXT and SOHO/MDI data both before and after eruption. The LFFF coefficient (α) giving the best fit to pre-flare observations was of the order of $\alpha=1.49\text{x}10^{-8}$ Mm^{-1}. Figure 4.11 illustrates an example extrapolation of the type achieved using this technique. The upper image shows SXT data taken during the flare. The lower image shows the corresponding section of MDI magnetogram data with extrapolated magnetic field lines superimposed onto the image.

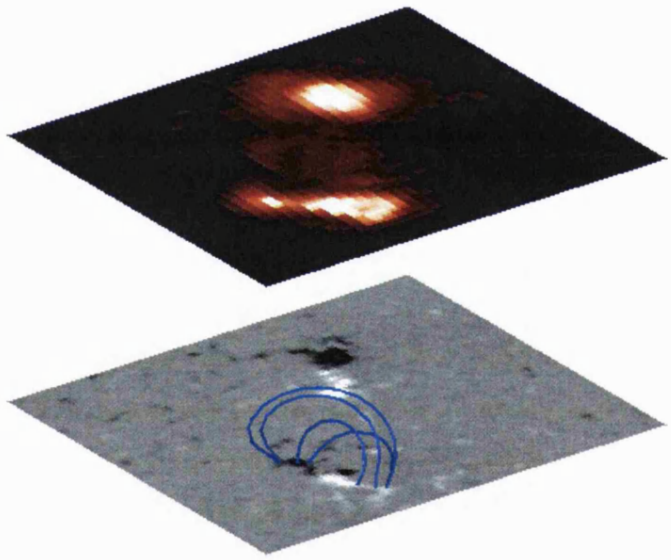

Figure 4.11: Example force-free field extrapolation, as applied to SXT and MDI magnetogram data from the 11th October 1997 event. The upper image shows SXT observations of the region to be extrapolated. The lower image shows the corresponding section of MDI magnetogram data with extrapolated magnetic field lines superimposed above.

Post-event data confirms the formation of an unsheared arcade. At this time, the magnetic configuration observed in SXT data could be accurately represented using a potential field extrapolation (α=0). Achieving a potential field fit was not possible using pre-event images, thus suggesting that the pre-event structures were highly sheared. Therefore, the magnetic non-potentiality of the region was assumed to have decreased following this event.

4.4.2 NOAA AR 8097: 21-Oct-97 Event, a Projected-Sigmoidal Active Region

This region was classified as both sigmoidal and eruptive by Canfield, Hudson and McKenzie [1999]. An onset time of 19:55 UT is listed in Appendix A. This region was selected for discussion here as an example of an eruptive 'projected-sigmoidal' active region. Flaring was initially observed at 17:06 UT on 21st October 1997 in Yohkoh full disk data. These observations were made slightly earlier than the eruption time quoted by Canfield [1999] and listed in Appendix A. This event was also associated with a halo CME observed by LASCO on the same day. Other activity associated with the same event included a filament eruption, EUV dimming and coronal wave onset.

Coinciding with an increase in GOES flux at approximately 17:05 UT on 21st October, AR 8097 appears to undergo a change in morphology to form a bright, well defined reverse-S shaped feature in SXT half resolution data (4".9) at 17:06 UT on 21st October 1997, as illustrated in Figure 4.12.

EIT 195Å data illustrated in Figure 4.13 shows the appearance of a bright, reverse-S shaped EUV emission feature at 17:34 UT. This feature is spatially consistent with the reverse-S shaped feature observed in SXT approximately 30 minutes beforehand. The observation of the EUV emission feature, however, coincides with a period of Yohkoh spacecraft night. Therefore, comparison with SXT data at this time is not possible.

The EUV feature is observed during the main phase of the C-class flare. Comparison with Hα data from the Big Bear Solar Observatory, available at 1.5 minute cadence, illustrates that the EUV emission feature coincides with a filament eruption

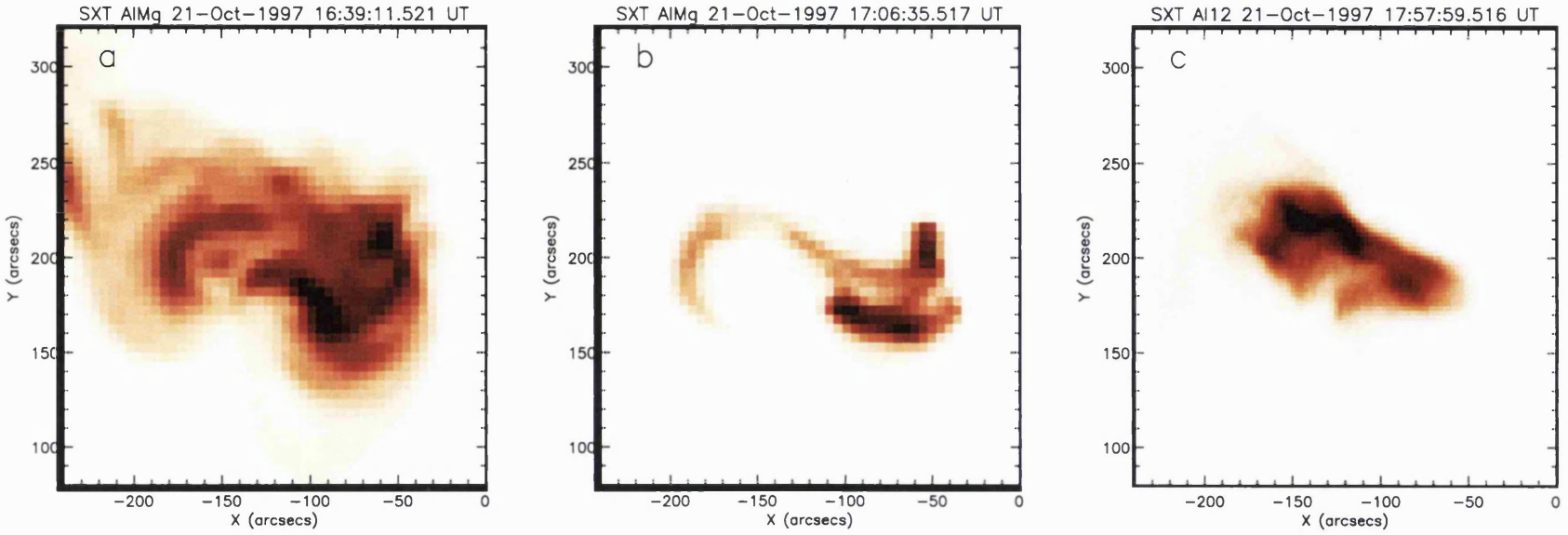

Figure 4.12: Yohkoh/SXT half and full resolution (4".9 and 2".45 per pixel respectively) data illustrating the formation of an apparently sigmoidal feature in AR 8097 just prior to eruption on 21st October 1997. Figure (a) at half resolution illustrates many small-scale loops oriented in an overall reverse-S configuration. Figure (b), also at half resolution, shows brightening and formation of an apparently single structure prior to CME onset and finally Figure (c), taken at full resolution, shows the post-eruption arcade. Images are reverse colour such that strongly emitting regions appear dark.

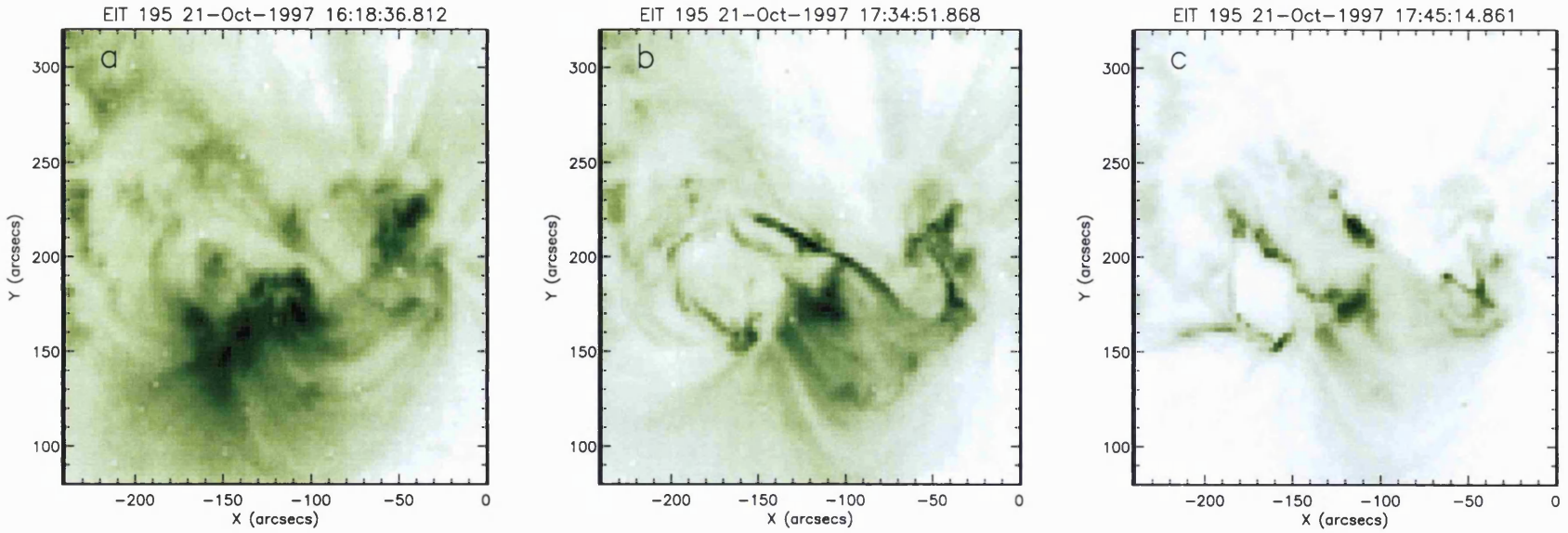

Figure 4.13: SOHO/EIT Fe XII (195Å) data illustrating formation of a reverse-S shaped feature in AR 8097. Figure (a) shows the pre-eruption configuration of loops. Figure (b) illustrates the appearance of a bright, reverse-S shaped feature approximately 30 minutes after the sigmoidal soft X-ray feature illustrated in Figure 4.12. Figure (c) indicates the cooler EUV counterpart of post-event loops observed in SXT data. The EIT data illustrated in this figure has resolution 2".5 per pixel.

observed in Hα data at 17:32 UT. Hα data for the earlier period during which the reverse-S shaped soft X-ray emission feature was observed however, does not show evidence that a filament eruption took place at this time.

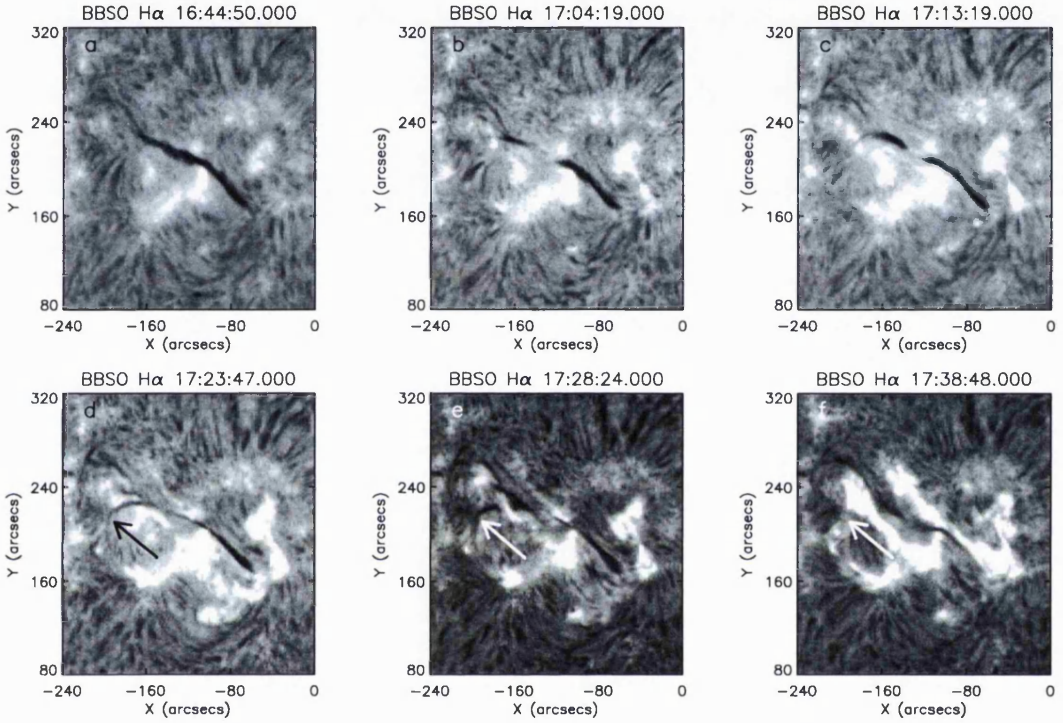

Figure 4.14: BBSO Hα observations of AR 8097 on 21st October 1997, at a resolution of 1" per pixel. Filament material is observed apparently draining from the initially straight filament channel into an adjacent curved channel, immediately preceding eruption. Figure (a) illustrates the almost straight filament channel aligned with the main active region neutral line prior to activity beginning. Figure (b) shows this straight filament appear to separate into two parts, Figures (c), (d) and (e) show changes in the filament structure as an additional curved channel forms at the eastern end of the existing straight channel. This curved filament erupts several minutes after formation leading to the filament layer eruption illustrated in Figure (f). Arrows indicate the location of the curved channel as it forms and erupts in association with a filament layer eruption along the main active region neutral line.

Figure 4.14 illustrates changes in the Hα morphology of AR 8097 during the period in which both soft X-ray and EUV reverse-S shaped features were observed. Figure 4.14a shows that prior to eruption, the filament occupies an almost straight channel.

Coinciding with initial observation of the reverse-S shaped feature in SXT images at 17:06 UT, brightening is observed in Hα and the filament appears to separate into two parts, as illustrated in Figure 4.14b; possibly as a result of localised heating. Just prior to the appearance of the EUV emission feature at 17:34 UT, the filament material is observed to partially drain into a curved channel to the north east of the active region. Figures 4.14d and e show changes in the filament structure as the curved channel appears in Hα between 17:23 UT and 17:28 UT. The curved filament channel erupts several minutes after formation, leading to the filament layer eruption illustrated in Figure 4.14f. Both Hα ribbons and a residual filament suspended above the active region neutral line are observed following eruption in this case.

The curved channel into which the filament material flows is spatially consistent with both the pre-flare soft X-ray loops and the EUV emission feature. However, the relative timing of activity observed at soft X-ray, EUV and Hα wavelengths suggests that the EUV feature is associated with the filament eruption, whereas the soft X-ray feature is not.

The SXT filter ratio technique described in Chapter 3 was applied to SXT data in order to produce a temperature map of the reverse-S shaped soft X-ray feature. This map was obtained using consecutive SXT Al.1 and AlMg filter images and is shown in Figure 4.15. The temperature map illustrates a strong temperature and density discontinuity along the main sigmoid axis. Contours represent the intensity of the original soft X-ray image, and outline the sigmoidal feature. A discontinuity along this structure is observed on the temperature map as a sudden change from light to dark orange towards the western end of the feature. This observation is suggestive of more than one feature combining in projection to appear as if it were a continuous sigmoidal structure. A single soft X-ray loop would not be expected to show a jump in temperature along its length.

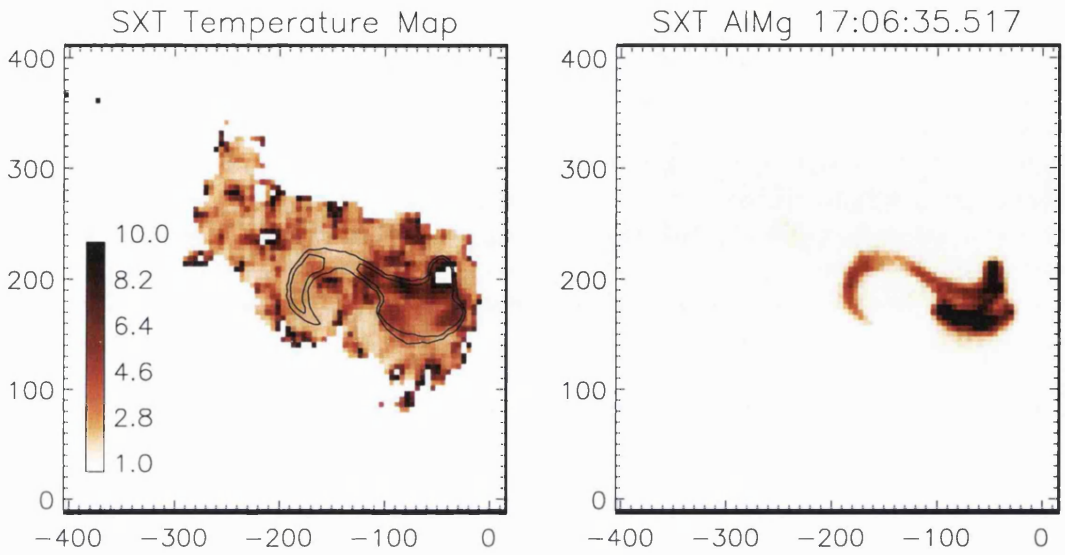

Figure 4.15: Comparison of SXT full disk data (4".9 per pixel) (right) with a temperature map (left) showing a strong temperature discontinuity along the sigmoid axis. Contour lines indicate the location of the bright SXR sigmoid on the temperature map. Temperature scale in units of MK. Axes are marked in arc-seconds in each case, solar north being oriented up and east to the left. The SXT image is displayed in reverse colour such that strongly emitting regions appear dark.

No full resolution (2".45 per pixel) observations were made prior to Yohkoh flare mode being triggered by this event. Therefore, the sigmoidal feature was only observed in three half-resolution images (4".9): a standard observing mode used during non-flaring periods. Owing to the existence of only lower resolution data, the temperature map is subject to uncertainties, as described in Section 3.1.2. However, a clear discontinuity is observed in the temperature map. This suggests that, at the time of observation, the sigmoidal feature observed in SXT did not represent the on-disk projection of a single twisted flux rope.

These observations suggest that the soft X-ray "sigmoid" observed in SXT may have consisted of a projection of smaller soft X-ray loops appearing to form a reverse-S shaped feature as a result of projection effects. Alternatively, a heated soft X-ray counterpart of the curved filament observed in Hα data between 17:23 to 17:28 UT, may

have contributed to the reverse-S shaped appearance of the region [e.g. Kano, 1994; Hudson et al., 1999].

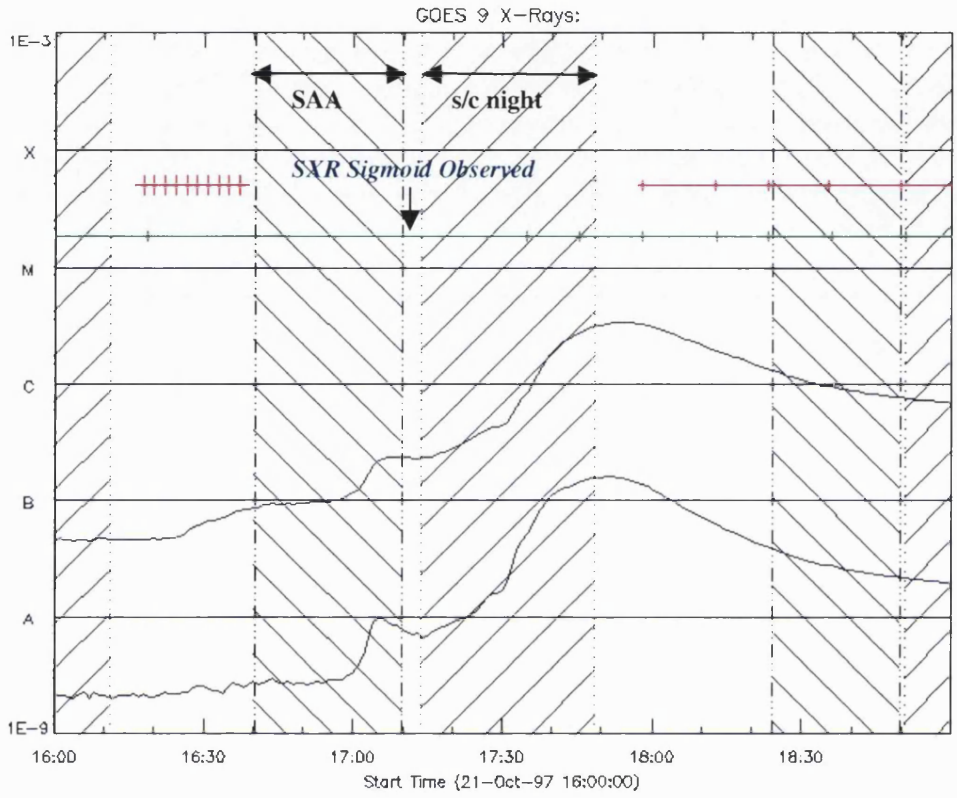

Figure 4.16: GOES 1-8 Å light curve indicates the influence of Yohkoh night & SAA crossing (left handed hatching represents spacecraft night and right handed hatching indicates SAA crossing) on observation of the 21st October 1997 eruptive event. The horizontal red line indicates SXT exposure times (short vertical lines denote partial frame images and long lines denote full frame). The green line indicates EIT 195Å exposures. The soft X-ray sigmoid is initially observed at 17:06 UT in the interval following Yohkoh SAA crossing and preceding spacecraft night.

A height-time extrapolation was applied to CME ejecta observed by the LASCO coronagraphs (see Section 3.2.1 for a description of this technique). The CME onset time was estimated to be 17:24 UT with an uncertainty of approximately ±7 minutes. This is consistent with a period of increasing GOES X-ray flux, just preceding the rise phase of

the main flare, as indicated in Figure 4.16. The estimated CME onset time follows the appearance of the soft X-ray sigmoidal feature by approximately 18 minutes. It also precedes the first Hα observation of a filament eruption and the appearance of the eruptive, reverse-S shaped EUV feature illustrated in Figure 4.13b.

A force-free field extrapolation was also applied to the active region. However, the model was unable to recreate the level of twist observed in the soft X-ray sigmoid. Noting that the apparently sigmoidal feature is observed *after* the initial rise in GOES X-ray flux preceding flare onset, it is possible that the level of activity within the region at that time exceeds the maximum that can be attributed to a constant α force-free field. These extrapolations assume an approximately steady state and uniform distribution of α. Neither condition is likely to be the case during flaring. However, it is also possible that the inability of the model to provide an accurate fit to the observed SXT structure provides further evidence that the SXT sigmoid does not trace out a single structure, and that projection effects lead to its sigmoidal appearance in SXT full frame data.

4.5 Comparison of AR 8092 and 8097 Eruptive Events

Section 4.4 has described analysis of two active regions previously considered to be both sigmoidal and eruptive by Canfield, Hudson and McKenzie [1999]. These regions were reclassified in Section 4.3 of this thesis as sigmoidal and projected-sigmoidal respectively. The aim of this section is to provide comparison between the processes leading to formation and eruption of these reclassified regions in order to determine whether sigmoidal and projected-sigmoidal active regions erupt by means of the same process.

Table 4.6 illustrates the main similarities and differences between the two case studies. Each region was found to erupt by means of a different process. NOAA AR 8092 appears to erupt through reorganisation of the coronal fields visible in soft X-ray data to form a single twisted flux rope. This becomes unstable in a similar manner to that described by Pevtsov, Canfield and Zirin [1996]. These observations are in accordance with the scenario described by van Driel-Gesztelyi et al. [2000]. In the scenario described

by these authors, reconnection leads to the formation of a twisted field line surrounding an already existing flux rope and the formation of shorter field lines beneath. Both the overlying S and the smaller loops below are observed to erupt. The S-shaped loop erupts as a result of instability gained from the twist imparted to this field via reconnection of j-shaped loops. The shorter, underlying loops erupt as a result of the formation of a current sheet caused by the rapid rise of the overlying helical field. In the case of AR 8092 considered here, the active region is small and inclined at such an angle that cusp-like loops cannot be observed. However, the formation of a bright, unsheared arcade is observed in both SXT and EIT 195 Å post-event images.

Table 4.6: Summary table comparing main features of the eruptive activity associated with sample sigmoidal and projected-sigmoidal active regions.

	AR 8092 : 11th Oct 97	**AR 8097 : 21st Oct 97**
Pre-eruption SXR appearance	S	Discontinuous reverse-S
Post-eruption SXR appearance	Arcade	Arcade
Flare Magnitude	B4.8	C3.3
CME observed	Y	Y
Filament Eruption/ Chromospheric reorganisation	Y	Y
EIT Wave	Y	Y
White light sunspots	N	Y

Erupting sigmoidal active regions studied by van Driel-Gesztelyi et al. [2000] and Manoharan et al. [1996] show evidence of coronal dimming taking place at large distances from the erupting active region sigmoid. These dimmings are interpreted as the effect of the rising twisted structure as it interacts with overlying loops. This indicates that the sigmoidal field may not be simply connected.

No remote dimming regions were observed in association with the eruption of AR 8092. This may be due to the triggering of Yohkoh flare mode in association with the event. However, nearby flux systems are undoubtedly present in the case of AR 8092. The proximity of AR 8092 to AR 8093 and the observation of emerging flux to the north-east of AR 8092 (in the region separating it from AR 8093), is suggestive of interaction

with overlying loops and nearby flux systems. This follows the "sigmoid-expansion" model of van Driel-Gesztelyi et al. [2000].

The temperature map of NOAA AR 8097 shown in Figure 4.15 suggests that, although it appears to form a single structure just prior to eruption, the region actually consists of more than one feature observed in projection. AR 8097 also appears to both gain and lose its *projected* sigmoidal appearance in close association with the formation and consequent eruption of an underlying reverse-S shaped filament (Figure 4.14). Unfortunately, saturation of SXT data during the eruption of AR 8092 prevents a direct comparison between temperature maps of each region during the initial rise in GOES flux. However, it is thought unlikely that both would exhibit the same discontinuity as no soft X-ray counterpart for the west 'hook' of the AR 8097 sigmoid is observed prior to formation of the transient, reverse-S shaped brightening. It is also possible that the inability of the force-free field extrapolation to reproduce the observed level of twist provides further evidence that the transient feature consists of more than one feature observed in projection and not a continuous flux rope.

Following eruption, a transequatorial connection is formed between AR 8097 and a weak polarity region in the southern hemisphere. This system of loops will be discussed in more detail in Chapter 6 where an illustration of the transequatorial loop system can be found in Figure 6.8.

Both regions considered here exhibit an overall S (or reverse-S) like nature, composed of several smaller features for a period of several days prior to eruption. However, not until X-ray emission from the region increases in association with flaring do they appear to form a continuous transient S (or reverse-S) shaped structure. Both active regions exhibited sigmoidal morphology for a period of less than an hour prior to eruption. This is in agreement with the observations of Pevtsov, Canfield and Zirin [1996] who found that a transient, reverse-S shaped soft X-ray feature formed within an active region tens of minutes prior to eruption. In addition, neither active region appears to erupt as a single bipole. In both cases external fields appear to play a role in the energetics of eruption.

4.6 Conclusions

This study has extended the findings of previous investigations into the connection between "sigmoid-to-arcade" development, seen in soft X-ray active region observations, and CME launch by the inclusion of white light, EUV and Hα data. By increasing SXT resolution to include full resolution partial frame data (2".45 per pixel) where available, regions previously classified as both sigmoidal and eruptive using only full disk resolution data could be further divided into three sub-categories:

- sigmoidal,
- projected-sigmoidal and
- non-sigmoidal

where only the "sigmoidal" category is consistent with the observation of a helically twisted flux rope, as described by Rust and Kumar [1996].

This extended survey has shown that regions having clearly defined sinuous S (or reverse-S) type morphology do possess a stronger tendency to erupt with the formation of an associated CME, coronal EUV dimming and, on occasions, a coronal EIT wave.

Furthermore, S- (or reverse-S) shaped regions found to comprise many smaller features superimposed onto one another in projection do appear less likely to erupt than regions found to constitute a single sigmoidal structure; an observation consistent with their separate classification as "projected-sigmoidal" rather than "sigmoidal" regions. A further survey incorporating several years' data from the above instruments may provide additional examples of sigmoidal active regions, thus allowing a more quantitative, statistical analysis of differing activity levels exhibited by active regions of each category.

Following the extended survey, two of the surveyed eruptive active regions have been described in detail. These regions were selected as examples from the sigmoidal and projected-sigmoidal categories on the basis of activity associated with eruption in each case and clarity of the sigmoidal feature observed. The aim of this comparison was to

determine whether both sigmoidal and projected-sigmoidal regions erupt by means of the same process.

Both active regions are observed to gain their sigmoidal structure *after* the initial rise in GOES X-ray emission associated with flaring. In each case, the transient feature is visible for under an hour prior to eruption.

Comparison with proposed models for sigmoid eruption, suggests that the first active region (8092) erupts by means of a "flux breakout" mechanism similar to that described by Antiochos [1998] and applied to sigmoidal features as a "sigmoid-expansion" model by van Driel-Gesztelyi et al. [2000] and Manoharan et al. [1996]. These models require the presence of additional flux systems in order that reconnection and removal of the overlying field can take place prior to eruption of the sheared sigmoidal core flux. The sigmoidal core structure itself is thought to form through successive reconnection of fields below a magnetic flux tube. Reconnection forms both helical fields wrapped around the flux tube and shorter loops below. The rising unstable flux leads to formation of a current sheet below and thus finally to cusp-shaped loops.

The second region considered also illustrates external connection resulting from eruption. However, this active region does not appear to erupt by means of the same process. A temperature map of the reverse-S shaped soft X-ray feature formed in association with the event illustrates a temperature discontinuity along the sigmoid axis; an observation suggestive of more than one feature being observed in projection. Further evidence that the reverse-S shaped feature did not constitute a single structure was found when the force-free field model applied to the data proved unable to reproduce the level of twist observed in the reverse-S shaped feature.

Rather than the above "expanding-sigmoid" model of eruption, it is thought that the eruption of AR 8097 is associated with changes observed in the underlying filament channel. Prior to eruption, the initially straight filament channel drains into a curved channel spatially consistent with the location of the eastern "elbow" of the reverse-S shaped feature. This erupts soon after formation, leading to a filament layer eruption along the main active region neutral line, associated flaring and CME onset. In this case,

eruption is thought to take place by means of a different mechanism. The active region does not display characteristics of a twisted flux tube in soft X-ray data.

Comparison of these two active regions, both of which have different magnetic field topology, suggests that not all features with sigmoidal appearance appear in active regions by means of the same processes and they may in fact comprise different magnetic field arrangements (i.e. a single structure or many smaller structures viewed in projection). Further understanding of how and when these features form, together with understanding of how they interact with the surrounding field regions may provide a better means with which to predict their eruption.

4.7 Summary

- This survey has extended the results of Canfield, Hudson and McKenzie [1999] to show that regions having clearly defined sinuous S (or reverse-S) type morphology at SXT full resolution (2".45 per pixel) do possess a stronger tendency to erupt than regions composed of several smaller loops aligned such that they appear sigmoidal as a result of projection effects.
- Comparison of an eruptive sigmoidal and projected-sigmoidal active region illustrated that both active regions gained their transient S (or reverse-S) shaped structure *after* the initial rise in GOES X-ray emission associated with flaring.
- Comparison of these two active regions, both of which have different magnetic field topology, suggests that these sigmoidal features did not form or erupt by means of the same processes. Both examples appear to consist of different magnetic field arrangements.
- Further understanding of how and when these features form, together with understanding of how they interact with the surrounding field regions is needed in order to provide a better means by which to predict their eruption.

Chapter 5:

Formation and Evolution of a Non-Active Region Sigmoid

This investigation extends previous studies of sigmoidal features in the corona and their associated CME activity to provide the first detailed study of the formation and evolution of a large sigmoidal feature unconfined by a single active region. The region's CME and flaring activity is studied and the relative timing of eruptive activity and sigmoid appearance is considered.

5.1: Introduction

Coronal Mass Ejections (CMEs) are known to originate in association with both flaring of bright, compact active regions [e.g. Hudson et al., 1998; Harrison, 1990] and the gradual destabilisation of quiet coronal features such as helmet streamers and quiescent filaments [e.g. Illing & Hundhausen, 1985; Low, 1994; Webb et al., 1998; Plunkett et al., 2000]. As described in the preceding chapter, recent studies of eruptive coronal features have centred around *sigmoidal* features observed at soft X-ray wavelengths. Thought by some authors to indicate the presence of helically twisted magnetic flux tubes in the corona [Rust & Kumar, 1996], these features have been associated with a high probability of eruption [Canfield Hudson & McKenzie, 1999; Hudson et al., 1998].

To date, these studies have concentrated only on sigmoids observed in the vicinity of strong active region fields. However, large scale sigmoids, unconfined by a single active region, have not yet been studied in detail [Canfield, Hudson & Pevtsov, 2001]. Therefore, little is known about how these apparently twisted structures form and evolve in weak field regions of the corona. Furthermore it is not yet known whether any connection between eruptive activity and non-active region sigmoids is the same as the

relationship thought to exist between eruptive activity and sigmoids that form within active regions and their associated stronger magnetic fields.

If sigmoidal features indicate the presence of helically twisted magnetic flux ropes in the corona, then they provide a means by which magnetic helicity stored within coronal fields can be visualised through observational data. Section 1.2.5 briefly discusses how magnetic field line twist relates to magnetic helicity. Consequently, understanding the origin of this twist may lead to an understanding of how magnetic helicity is generated in the corona as a whole, although a quantitative analysis of this connection is beyond the scope of this study.

Several studies have proposed mechanisms by which magnetic helicity can be generated in the corona. Therefore, in some cases these mechanisms may be partly responsible for sigmoid formation. These mechanisms will be discussed briefly in the following paragraphs.

Differential rotation acting on emerged flux was initially proposed as a mechanism for helicity generation in the corona by Sturrock and Woodbury [1967]. These authors considered the variation in photospheric velocity from the equatorward side of a sunspot to the side closest to the pole resulting from differential rotation. In this case, the action of differential rotation would induce helicity into the newly emerged field through rotational motion. As a result, twist will be generated in the vertical magnetic flux tube. More recently, van Ballegooijen [1999] simulated the action of differential rotation combined with granular & supergranular diffusion flows on an untwisted bipole rooted in the photosphere. This study found that these combined motions were able to generate sufficient helicity to lead to a hemispherical preference in the sense of twist (chirality) consistent with the observed rule (positive in the south and negative in the north). Furthermore, DeVore [2000] estimated the contribution to the Sun's total magnetic helicity balance that a model sunspot group would generate through the action of differential rotation over the course of several solar rotations. This study found that the helicity induced by differential rotation could successfully account for the observed hemispheric chirality trends together with the observed helicity balance between coronal structures and interplanetary cloud measurements at 1 AU.

In contrast, magnetic helicity may also be generated below the photosphere, prior to flux emergence. Pevtsov, Canfield and McClymont [1997a] compared measurements of the force free field parameter (α) calculated from vector magnetogram data at the photosphere and (α) inferred from coronal X-ray observations of sigmoidal active regions. These authors found a strong correlation between the orientation of electric currents observed at the photosphere and those measured from coronal observations. These authors inferred from this observation that the source of these currents, and consequently of field line twist, may be of sub-photospheric origin.

Using a different approach, van Driel-Gesztelyi et al. [1997] and Leka et al. [1996] found that the magnitude of vertical currents measured above active regions increased in association with emerging flux and sunspot rotation. This observation indicates that emerging flux may already be in possession of significant twist prior to its emergence through the photosphere.

The studies described above provide evidence for helicity generation both above and below the photosphere. However it has not yet been conclusively determined which mechanism holds the greatest influence over the observed distribution of helicity in the corona [Pevtsov, Canfield & Metcalf, 1995].

This study considers three rotations of a large active region and the surrounding area. The influence of differential rotation on the emerged flux regions is estimated.

The active region is observed to decay over three rotations. Sigmoidal structures develop during both second and third rotations. The large scale sigmoidal feature is formed during the third rotation, among weak field regions that remain after the decay of the main active region. Its appearance in soft X-ray data at this time is illustrated in Figure 5.1. Changes in coronal, chromospheric and photospheric features are analysed in order to understand the processes leading to the formation and eruption of the large scale S-shaped feature.

Both the action of differential rotation and emergence of magnetic flux in possession of twist would act to increase the helicity content of the active region field. Through the ejection of magnetic flux into the corona, CME activity from the region may act to balance this increase and reduce the helicity content of the region [Demoulin et al.,

2002; van Driel-Gesztelyi et al., 1999; Low, 1996]. According to the principle of helicity conservation, magnetic helicity will be approximately conserved during reconnection [Berger, 1984] i.e. during periods of confined flaring. However, helicity will be removed through CME onset as large quantities of magnetic flux are ejected into the corona. Consequently, CME and flaring activity from the region is studied together with associated soft X-ray morphology changes in order to observe the influence of differential rotation and emerging magnetic flux on the level of activity throughout all three rotations. In addition, whenever a sigmoidal feature is observed within the region, the relationship between the sigmoidal feature and eruptive activity was considered in order to determine whether the CME appeared or disappeared in association with eruptive activity.

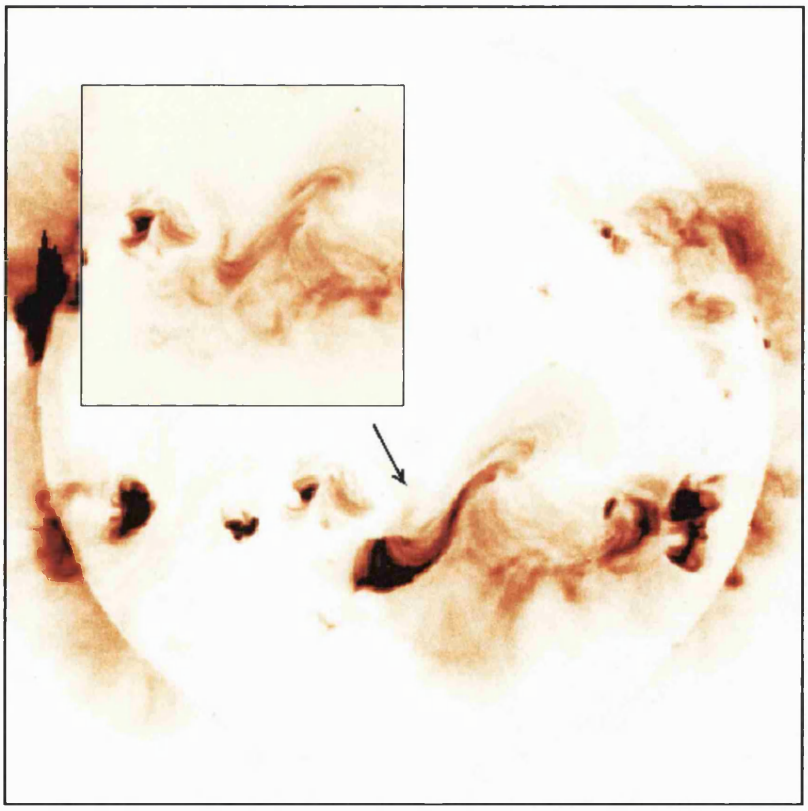

Figure 5.1: SXT full disk image illustrating a large scale sigmoidal region as it appears to form a single structure following CME onset at 09:45 UT on 8th May 2000. Inset panel illustrates the same region prior to eruption at 04:36 UT. Images are reverse colour such that strongly emitting regions appear dark and both have 4".9 per pixel resolution.

5.2: Observations

Observations describing the third (May) rotation of NOAA AR 8906 during which the large scale sigmoidal feature was observed were made as part of a SOHO Joint Observing Programme (JOP). This programme was titled 'Formation and Evolution of a Sigmoidal Active Region' and was initially scheduled as a target of opportunity programme between 29th April and 14th May 2000. The large scale sigmoid was selected as a suitable target on the 7th May. Observations continued until 11th May by which point the region had approached the west limb.

Yohkoh SXT data [see Chapter 2 for a description of SXT] having resolution 2".45, 4".9 and 9".8 per pixel, were employed in order to study the region's sigmoidal appearance at X-ray temperatures throughout all three rotations.

In addition to soft X-ray morphology changes associated with flaring and CME onset, photospheric changes were monitored throughout the three observed rotations using full disk magnetograms from the SOHO Michelson Doppler Imager (MDI) [See Chapter 2 for a description of MDI]. Five minute averaged magnetograms with a cadence of 96 minutes and 2" per pixel resolution were available.

In order to determine how activity associated with the region varied over the three studied rotations, all GOES events and CME onsets associated with this region whilst it remained visible on the disk were recorded.

Flare magnitude and duration information was obtained from Solar Geophysical Data (SGD: US Dept of Commerce) in the form of 1-8 Å observations from the GOES satellite series of full Sun monitors. In cases where no NOAA active region number had been assigned to a particular GOES event, EIT Fe XII (195 Å) data and SXT full disk data were studied for that period. If flaring could be unambiguously identified as originating from the region of interest alone then that event was included in the survey.

CME onset was inferred through study of EIT Fe XII (195 Å) and LASCO coronagraph data [see Chapter 2 for descriptions of these instruments]. Percentage difference movies were created from EIT 195 Å data using the technique described in Chapter 3. These images were available at a cadence of approximately 20 minutes with

resolution 2".6 or 5".2 per pixel. In the event that EIT 195 Å data illustrated mass motion associated with the eruption of underlying filament material, EUV dimming and/or the onset of a coronal EIT wave [Thompson et al., 1998] from the region of interest, a comparison was made with LASCO CME data.

Height-time extrapolations were applied to LASCO data in order to determine an approximate onset time and location for each CME. If the origin could be confirmed as consistent with the region of interest by comparison with disk observations, the CME was included in the survey.

The chromospheric data described in Section 5.4 was provided by two sources. Hα data from the HIDA Flare Monitor Telescope (FMT) has a spatial resolution 4".2 per pixel and cadence 1 minute. Hα data from the Big Bear Solar Observatory was available with a spatial resolution of 1" per pixel and cadence 1.5 minutes.

5.3: Long Term Evolution of AR 8906: March – May 2000

The active region that this study focuses on was initially classified as NOAA AR 8906 on 9th March 2000. This study considers the development of this region over three rotations from its appearance around the east limb on 9th March 2000 until its approach of the west limb on 12th May 2000. Table 5.1 and Figure 5.2 provide a comparison between activity associated with this region throughout the three observed rotations.

During the March rotation AR 8906 dominated activity on the disk as the largest and most complex active region. During both the March (1st) and April (2nd) rotations, a large number of GOES events were observed to originate from the vicinity of AR 8906[1]. These events included 6 M-class flares during March and 9 M-class flares during April.

In addition, 10 CMEs were observed to originate in association with activity in the vicinity of AR 8906 during the March rotation and 9 CMEs were observed to originate with activity associated with this region during April.

[1] It should be noted that the active region was reclassified AR 8948 following its rotation and consequent reappearance around the east limb in April. However, for the purposes of consistency, this active region will be referred to as AR 8906 throughout this chapter

A considerable decrease in activity originating from AR 8906 was observed between April and May. Whereas high levels of CME and flaring activity had been observed during both March and April rotations, the May rotation saw the region associated with only 1 B-class GOES event and 2 CMEs.

Table 5.1: Distribution of GOES events and CME activity from AR 8906 observed between 9th March and 12th May 2000. CM denotes central meridian in this case.

Date of CM Pass (2000)	GOES Events				CME Onsets
	X	M	C	B	
13th March	0	6	67	0	10
10th April	0	9	39	0	9
7th May	0	0	0	1	2

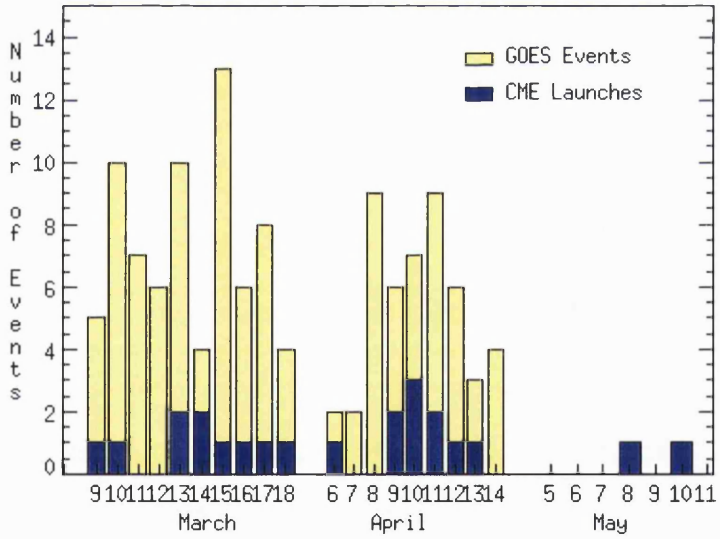

Figure 5.2: Distribution of GOES events having magnitude in excess of B1.0 and CME onsets originating from AR 8906[1] during the period 9th March to 12th May 2000. High flaring (indicated in the figure by "GOES Events") and CME activity is observed during both March and April rotations. The final (May) rotation shows that CME activity persists but flaring has almost ceased.

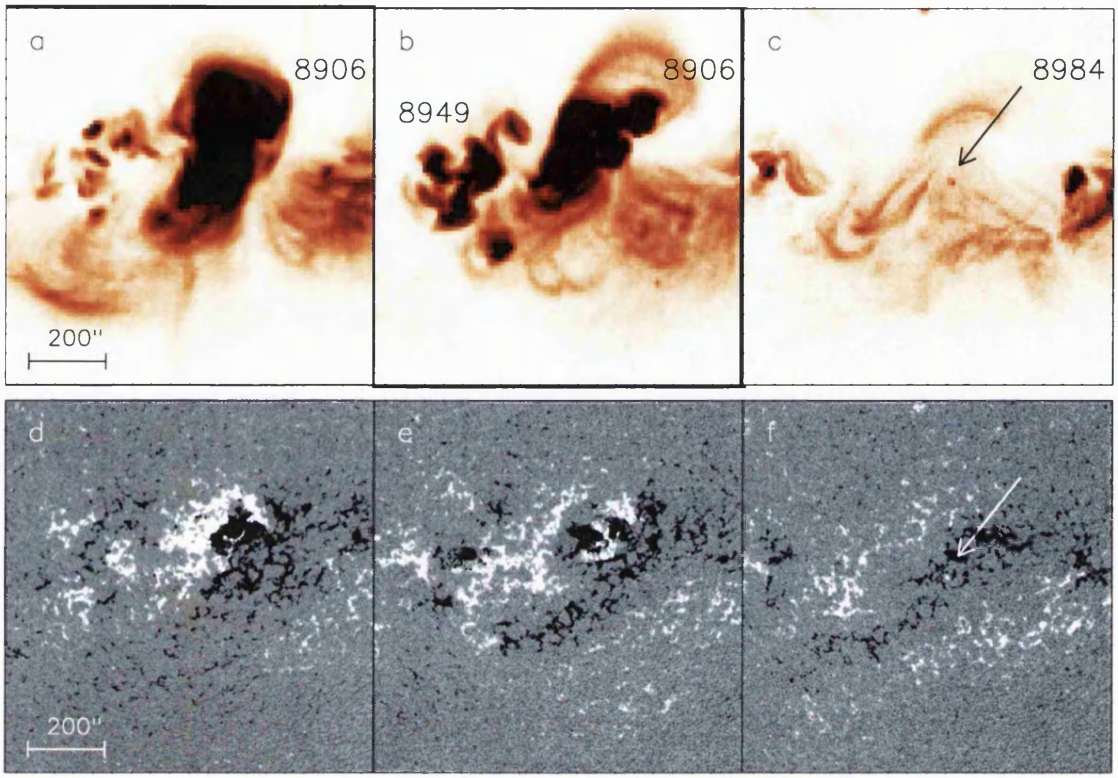

Figure 5.3: SXT (a, b, c) and MDI (d, e, f) full disk observations taken near consecutive meridian passes. 13th March (a,d), 10th April (b,e) and 7th May (c,f). Strong active region flux disperses over three rotations, forming an extended filament channel. The growth of this filament channel can be observed in Figures (e) and (f). SXT data has resolution 9".8 per pixel in each case and MDI data has resolution 2" per pixel. Solar north points up and east to the left. Arrows in Figures (c) and (f) indicate the emerging flux region AR 8984. Magnetogram data shows positive magnetic flux (line-of-sight magnetic field oriented towards the observer) in white and negative in black. Images are reverse colour such that strongly emitting regions appear dark.

Figure 5.3 provides a comparison between full disk SXT and MDI data as the region crosses central meridian during each of the three studied rotations. Comparison of Figures 5.3d, e and f illustrates the action of differential rotation and flux diffusion on AR 8906 over the course of three rotations. Comparison was also made between the region's extent in white light data (as calculated by SGD) as it crossed the central meridian during the March and April rotations. This showed that the sunspot region had decreased in area

to approximately 18% of the size observed as it crossed the central meridian during the previous (March) rotation. Differential rotation, combined with the action of flux diffusion arising from granular and supergranular motion, has caused the flux to disperse and begin formation of an extended neutral line.

Throughout its evolution, AR 8906 is situated entirely within the southern hemisphere. Consequently the region follows the hemispheric rule that suggests regions with magnetic fields subject to right-handed twist, indicated in this context by S-shaped coronal structures, will predominate in the southern hemisphere.

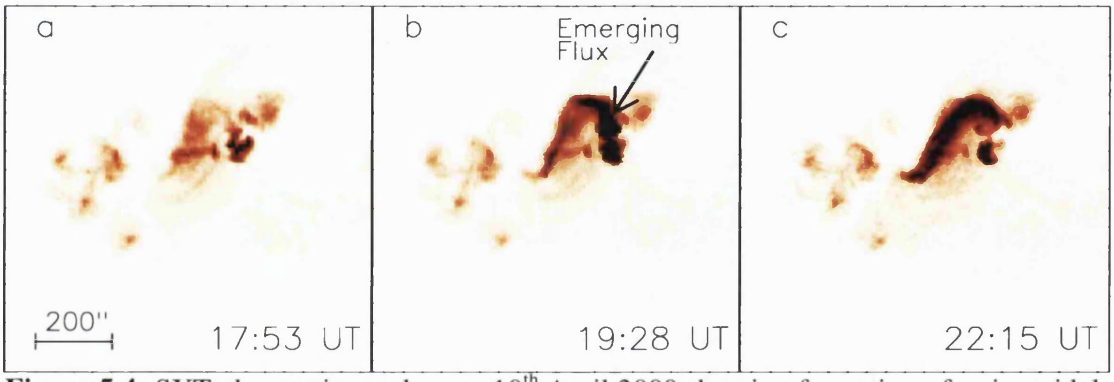

Figure 5.4: SXT observations taken on 10th April 2000 showing formation of a sigmoidal feature. A sigmoidal feature is observed to form between emerging flux in the north west and the outlying filament channel to the south east. Figure (a) illustrates AR 8906 prior to flaring. Figure (b) illustrates flux emergence, possibly the cause of a C8.6 class flare peaking at 19:11 UT. SXT data has resolution 4".9 per pixel. Solar north points up and east to the left. Images are reverse colour such that strongly emitting regions appear dark.

The second (April) rotation shows an overall decrease in the level of flaring and CME activity from the area under observation; now composed of an active region and extended neutral line (Figures 5.3b and e). The most CME active period during the second rotation coincides with the appearance of the strongly sigmoidal feature illustrated in Figure 5.4. Initially observed following a C8.6 class flare from the region on the 10th April at 19:11 UT, this feature forms a connection between emerging flux at the centre of AR 8906 and the neutral line that now extends towards the south west of the remaining

active region. Figure 5.5, provides a comparison between the location of the sigmoidal feature observed in soft X-ray data and the region's photospheric magnetic structure seen by MDI. The north west edge of the sigmoidal feature is consistent with a region of strongly emerging flux at the centre of AR 8906. The south east edge of the feature, however, extends towards the more diffuse flux regions of the filament channel.

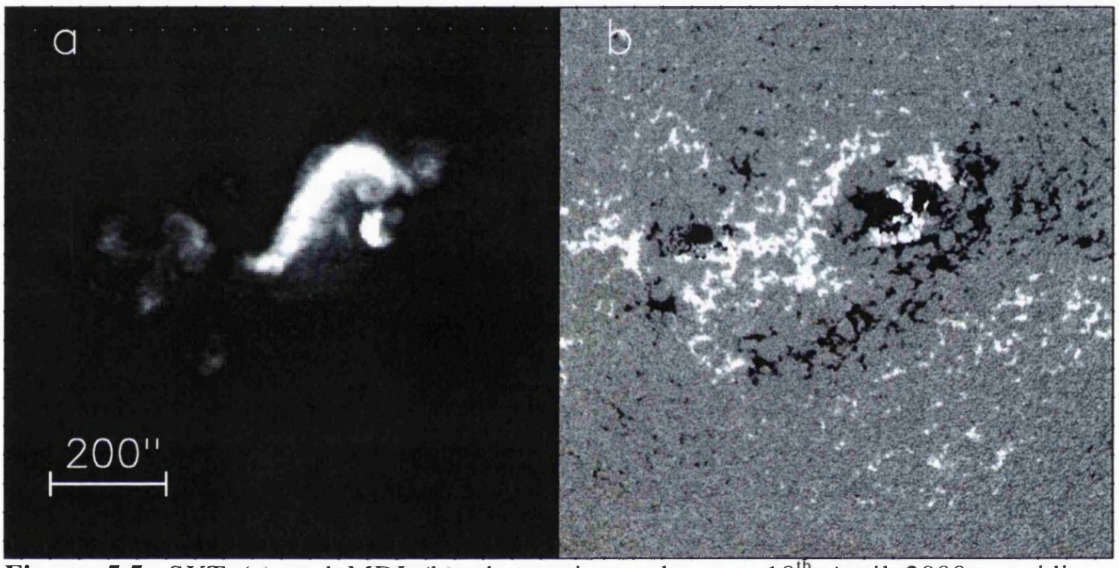

Figure 5.5: SXT (a) and MDI (b) observations taken on 10th April 2000 providing comparison between the location of the sigmoidal feature and the region's photospheric magnetic structure. The sigmoidal feature is observed in Figure (a) to connect newly emerging flux in the north west to the gradually diffusing filament channel. SXT and MDI data have resolution 4".9 and 2" per pixel respectively. Solar north points up and east to the left.

Figures 5.4 and 5.5 described above, both show the April sigmoid in SXT full disk data. This feature appears to consist of a single structure. Unfortunately, although partial frame observations were made of this region at this time, the size of the sigmoidal feature exceeded that of the field of view. Therefore, it was not possible to verify this observation using data of higher resolution.

In this case, the sigmoid was observed to gradually fade over a period of approximately 12 hours, rather than disappear in direct association with CME onset.

During this active CME period, a further active region labeled AR 8949 is observed to emerge in close proximity to the extended filament channel. This active region was observed to increase in size throughout the April rotation. The proximity to AR 8906 may also have contributed to the increase in activity during this period.

5.4: Activity During Rotation 3, May 2000: Formation and Evolution of a non-AR Sigmoidal Feature

The third rotation of AR 8906 began on 4th May 2000. By this time, the complex field regions associated with both AR 8906 and AR 8949 had dispersed almost entirely. MDI observations of the region shown in Figure 5.3f illustrate an extended neutral line with only a small, positive parasitic polarity region situated close to this neutral line. The parasitic polarity region may have indicated the remnants of AR 8906. Weak flux emergence within this parasitic region on 5th May 2000 led to its reclassification as an active region (AR 8984).

During the third rotation of AR 8906, two CMEs were observed in association with activity in this region. Table 5.2 lists the main characteristics of these events. The first event, a GOES X-ray class B6.8 two-ribbon flare, peaked at 06:23 UT on 8th May. This event took place as the, now diffuse, filament channel passed close to the central meridian. In this case, an increase in soft X-ray intensity was observed to originate from the southern half of the region. This contrasts with earlier activity which was concentrated in the northern half of the region close to the active centre of AR 8906 and the location of most emerging flux during previous rotations. It is at this point, following CME onset, that the large scale sigmoidal feature illustrated in Figure 5.1 is observed.

Figure 5.6a illustrates that, prior to eruption, soft X-ray features overlying the extended filament channel consist of many diffuse loops arranged in an overall S-shape. However, SXT data illustrated in Figure 5.6b suggests that, following CME onset, a change in morphology takes place and the region gains its sigmoidal appearance. Comparison with EIT 195 Å data illustrated in Figures 5.6c and d, shows that the curved southern tail of the sigmoidal feature is consistent with the appearance of a post-flare

arcade seen in EIT data. These loops are observed to fade over the hours following eruption along with the post-CME sigmoidal feature.

Table 5.2: Comparison between two CME onset events observed from AR 8906 during Rotation 3 (May 2000). Only Event (A) was associated with localised flaring.

	Event (A) 8th May 2000	**Event (B) 10th May 2000**
Peak Time (UT)	06:23	22:16
Flare Class	B6.8	None
CME First Observed in C2 (UT)	06:50	19:26
Filament Eruption	Partial	Full

Faint CME ejecta was first observed in the south west quadrant of the LASCO/C2 field of view at 06:50 UT on 8th May. A height time extrapolation finds CME onset to coincide with initial mass motion observed in EIT 195 Å data but precede the GOES X-ray peak.

Hα observations made by the HIDA Flare Monitor Telescope (FMT) during the eruption, show the presence of a discontinuous filament structure beneath the sigmoidal feature. Figures 5.6e and f illustrate the disappearance of the curved southern half of the filament during the event, together with the formation of bright footpoints. These footpoints correspond to the observation of bright flare arcades in both EIT 195 Å and SXT data. Extensive movement is observed in the northern half of the filament, although no complete disappearance and/or eruption is observed.

Following eruption on 8th May, the sigmoidal feature gradually fades in SXT data until 10th May. Figure 5.7a illustrates the soft X-ray morphology of the region at this time. No increases in soft X-ray intensity are observed between the decay of the sigmoidal feature on 8th May and the 10th May. At this stage, the region under observation has rotated towards the limb and sigmoidal morphology is no longer clearly distinguishable.

Commencing on 10th May 2000, and initially observed at 16:15 UT, Figures 5.7c, d and e illustrate a gradual rise in soft X-ray emission from the arcade. The arcade is

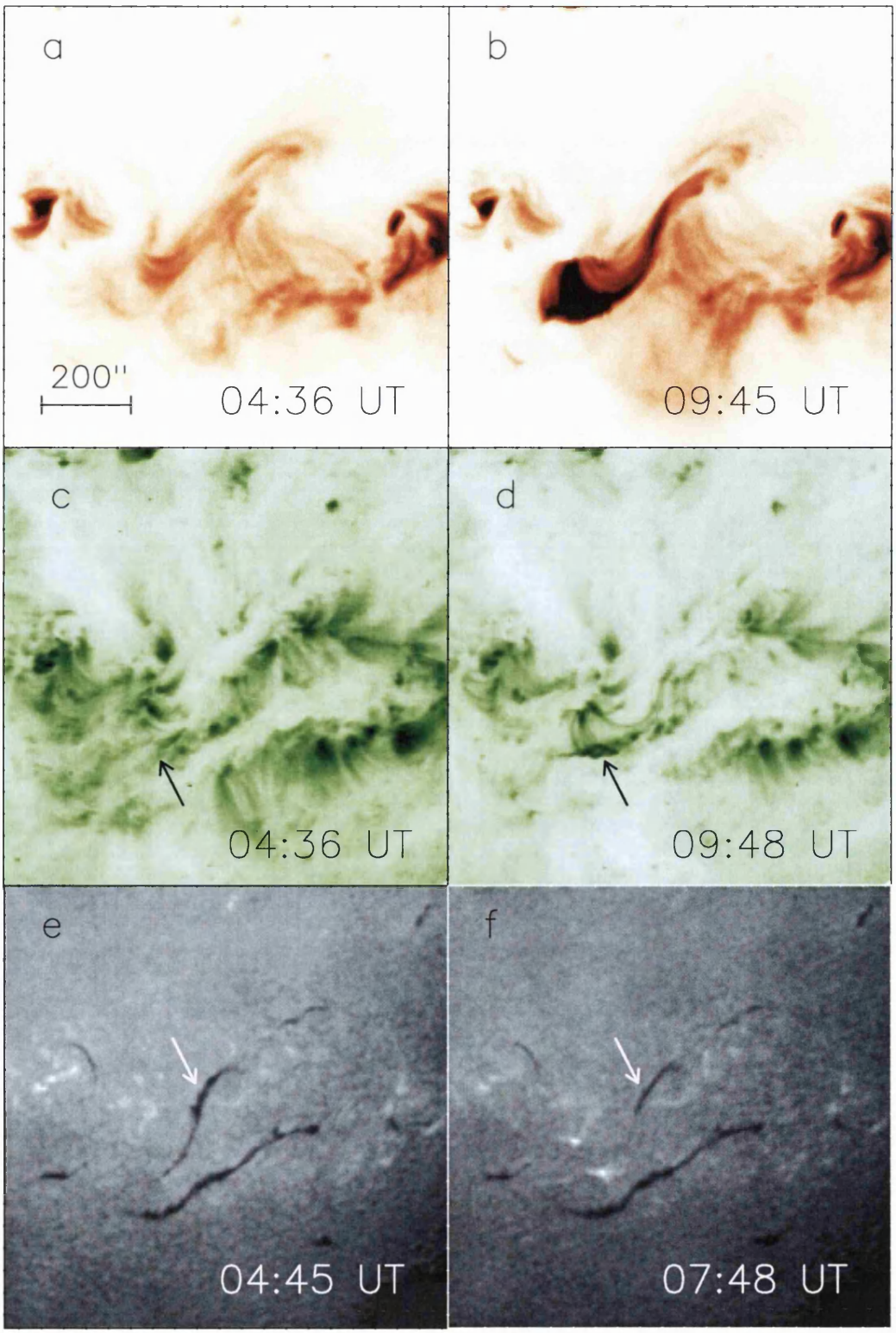

Figure 5.6: See the following page for full caption[2].

observed to expand and brighten. Maximum emission is observed from the region at 22:16 UT, directly following Yohkoh night.

Two loop-like CMEs were observed in the south west and north east quadrants of the LASCO/C2 coronagraph shortly after the rise in soft X-ray emission began. A height-time extrapolation of each and comparison with other activity on the disk suggests that the CME initially observed in the south west quadrant of C2 at 19:26 UT was most likely to be associated with the observed soft X-ray morphology changes in AR 8096. The estimated onset time is consistent with the gradual rise phase of the soft X-ray arcade illustrated in Figures 5.7c to e, but precedes the final configuration observed at 01:46 UT.

5.5: Discussion

This study follows the evolution of an active region through three rotations between March and May 2000. During the first (March) rotation, the region was highly complex and dominated activity on the disk. Prior to the region's reappearance in April, the action of differential rotation combined with photospheric velocity fields caused the active region flux to disperse and spread out with the formation of an extended neutral line. In addition, magnetic flux associated with both active regions was observed to have

[2] **Figure 5.6:** Comparison of SXT data prior to (a) and following (b) eruption on 8th May 2000 with EIT Fe XII (195 Å) (c & d) and Hα (e & f) data for the same period. Faint soft X-ray loops are replaced by a sigmoidal feature after eruption. Comparison with (d) and (f) shows this feature to be consistent with the post-event arcade seen to form in EUV and Hα data. Arrows in (c & d) indicate post-flare loops forming in the southern half of the filament channel. Arrows in (e & f) indicate an S-shaped filament channel underlying the soft X-ray arcade. The second filament, observed to the south of the S-shaped filament, remains unchanged throughout the eruption. Solar north points up and east to the left. SXT, EIT and Hα data have resolution 4".9, 5".2 and 4".5 per pixel respectively. SXT and EIT images are reverse colour such that strongly emitting regions appear dark.

undergone further dispersion prior to the third rotation. This left primarily only single polarities situated on either side of an extended neutral line

During the final two rotations, individual sigmoidal features were observed. The first sigmoidal feature extended approximately 150" in [x,y] coordinates and formed a connection between emerging flux at the centre of AR 8906 and outlying flux which had begun to align along the neutral line. This feature was relatively short-lived and disappeared after approximately 12 hours. The second sigmoidal feature was observed during the third rotation. This feature spanned the neutral line formed by the decay of active regions 8906 and 8949 and extended approximately 450" in both [x,y] coordinates. This sigmoid covered three times the spatial extent of the first sigmoid.

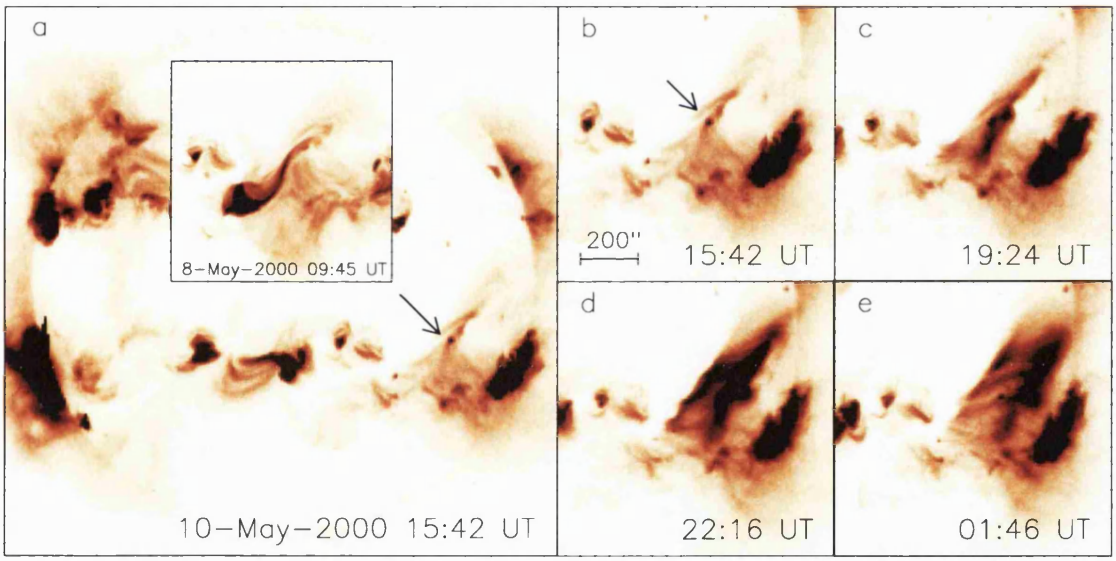

Figure 5.7: Soft X-ray morphology changes taking place between 8th May and 10th May 2000. Figure (a) provides a comparison between soft X-ray morphology of the region on 8th May 2000 (inset) and after two days rotation on 10th May 2000 (main image). The region now consists of an arcade, the location of which is indicated in (b) by an arrow. Figures (b) to (e) show the evolution of this arcade as it erupts on 10th May 2000. SXT data has resolution 4".9 per pixel in each figure. Solar north points up and east to the left. Images are reverse colour such that strongly emitting regions appear dark.

Observations of AR 8906 and its surroundings show flux emergence taking place during all three rotations. Although weak during the third (May) rotation, March and April observations illustrate strong flux emergence in agreement with the observed high levels of flaring.

The first (April) sigmoid appeared during a period of rapidly emerging flux. It is possible that this emerging flux was already in possession of twist prior to its emergence through the photosphere. Reconnection between this emerging field and existing active region fields would add to the apparent twist of the active region's magnetic field structures. This would be consistent with the appearance of the strongly sigmoidal feature directly following a C8.6 flare from the region.

Previous studies have suggested that both differential rotation [DeVore, 2000] and the emergence of flux tubes already in possession of significant twist [e.g. Pevtsov, Canfield & Metcalf, 1995] can make strong contributions to the total helicity content of coronal fields. Furthermore, it is thought that the presence of sigmoidal features within a region may indicate high levels of stored magnetic helicity. Observation of AR 8906 over three rotations suggests that both processes take place during the region's evolution. Therefore, both differential rotation and twisted flux emergence may contribute to the formation of sigmoidal features within the region during the April and May rotations. Direct measurements of the region's helicity budget would be required in order to determine which is the dominant generation process. This is beyond the scope of this study. However, it is possible to estimate the influence of differential rotation on the active region over the course of three rotations. The technique used to calculate this influence is described in the following section.

5.5.1: Action of Differential Rotation on AR 8906.

Owing to the large spatial extent of the non-active region sigmoid observed during the third (May) rotation, it was thought that differential rotation might influence changes in the region's morphology. Therefore, it was decided to study the influence of differential

rotation on the active region in order to determine whether this process could be responsible for the formation of the sigmoidal feature.

In order to estimate the effects of differential rotation, the increase in footpoint separation likely to arise through the action of differential rotation alone is considered. The difference between rotation rates at the northern and southern extents of AR 8906 flux system is calculated. This rate is then evaluated over the number of days separating each central meridian pass, giving an estimated increase in footpoint separation due to the action of differential rotation. The total angle through which the region has rotated between each meridian pass is then evaluated for northern and southern points and compared to the observed increase in longitudinal spread of the region. The observed spread in longitude was determined using full disk MDI images for each consecutive meridian pass. A smoothing function was applied in order to reduce rapid fluctuations in the data. This also had the effect of reducing the accuracy of this reading to approximately ±20". The MDI image was reduced in size to incorporate only the region of interest. Each horizontal line of the reduced image was then plotted as an intensity graph in order to determine which pixels have positive and negative fluxes in excess of twice the background level. The maximum longitudinal spread of these strong positive or negative flux regions in the vicinity of the decaying active region was then assumed to represent the maximum longitudinal extent of the region and converted to heliographic coordinates accordingly.

A simple expression for the latitude dependent rate of solar rotation is as follows:

$$\omega(\psi) = \omega_0 - \omega_2 \sin^2(\psi) \qquad \text{-(5.1)}$$

where ω_0 represents the maximum rotation rate at the solar equator, ψ the latitude at which the rotation rate is to be evaluated and ω_2 is taken to be 2°.77 day^{-1} following Newton & Nunn [1951]. This expression can be modified to calculate the difference in rotation rate between two latitudes $\Delta\omega_{NS}$:

$$\Delta\omega_{NS} = \omega(\psi_N) - \omega(\psi_S) = \omega_2\left(\sin^2(\psi_N) + \sin^2(\psi_S)\right) \qquad \text{-(5.2)}$$

where ψ_N and ψ_S denote northern and southern extents of the region prior to rotation. An estimate of the increased longitudinal extent of the region resulting from the action of differential rotation alone can then be expressed as:

$$\Delta x(calc) = (\Delta \omega_{NS})\tau \qquad -(5.3)$$

where τ denotes number of days between each central meridian crossing and $\Delta x(calc)$ is expressed in terms of heliographic longitude (°).

Table 5.3: Comparison between observed increase in longitudinal extent of AR 8906 over three rotations (Δx(obs)) and estimated values based on the action of differential solar rotation alone (Δx(calc)). Bracketed values indicate total longitudinal extent of the region measured at each central meridian (CM) pass.

Date of CM Pass (2000)	**Co-ords (North)**	**Co-ords (South)**	**Δx(obs) (°)**	**Δx(calc) (°)**
13th March	S09W09	S27E07	- (16)	-
10th April	S08W12	S33E19	15 (31)	9
7th May	S09W16	S32E24	24 (40)	17

Table 5.3 illustrates the diffusion of AR 8906 over the course of three rotations (Δx(obs)). Comparison with the increased separation predicted by the action of differential rotation alone (Δx(calc)) shows that, although this mechanism undoubtedly contributes significantly to the longitudinal increase of the region, it does not act alone. Other factors such as the observed emerging flux, flux cancellation and flux diffusion owing to the action of supergranular flow at the photosphere may also contribute to the increase.

Observation of CME and flaring activity associated with AR 8906 shows a decrease in the rate of flaring over all three rotations observed here. However, the number of CME onsets associated with the region remains high during the second rotation. The third rotation is the least active of the three: only one B-class flare is produced in

association with CME onset. It is interesting to note that this is the only event to originate from the southern half of the sigmoidal region. During the third rotation, the number of CMEs exceeds the number of flares as the region continues to disperse.

5.6: Conclusions

This investigation extends previous studies of sigmoidal features in the corona and their associated CME activity to provide the first detailed study of the formation and evolution of a large scale non-active region sigmoidal feature observed in soft X-ray data.

Individual sigmoidal features are observed during both the second (April) and third (May) rotations. The first sigmoid has [x,y] extent of 150" and forms in strong active region fields. In contrast, the second sigmoid forms within weak-field remnants of the same region following its decay to form an extended neutral line. The first sigmoidal feature is observed for approximately 12 hours and its appearance coincides with the period of highest CME onset frequency. This sigmoid does not disappear with a specific CME onset. Instead, it fades gradually. In contrast, the non-active region sigmoid gains its sigmoidal appearance *following* CME onset, as post-flare loops align along the neutral line. This sigmoid fades gradually over time.

Measurement of the increased latitudinal extent of the region, shows that differential rotation alone would be unable to reproduce the observed increase in extent gained over three rotations. As such, a combination of factors must lead to this increase. Other processes which may contribute to changes in the region's appearance are twisted flux emergence, flux cancellation and large scale surface flows.

Study of flaring and CME activity from AR 8906 illustrates high flaring and CME onset rate during both March and April in close association with periods of rapidly emerging flux. During the May rotation, both rates decrease. Flaring ceases but CME onset is still observed.

5.7 Summary

- This chapter provides the first study of a sigmoidal feature unconfined by a single active region. Both its CME and flaring activity were considered together with processes involved in its formation.
- The second (May) sigmoid has approximately three times the spatial extent of the first (April) sigmoid that was observed in the same region during the previous rotation.
- The April sigmoid formed during a period of high flaring and CME activity but does not disappear in association with a specific CME.
- Formation of the sigmoidal structure cannot be solely attributed to the influence of differential rotation. Other factors, possibly including emerging flux in possession of twist and large scale surface flows, must contribute to the final appearance of the region.
- Emerging flux is seen throughout all three rotations.
- CME activity is found to continue for three rotations although flaring has almost ceased by the third.

Chapter 6:

The Association of Transequatorial-Loops with CME Onset.

This study forms the first survey of transequatorial loop systems in terms of their eruptive character. Of a total 18 transequatorial loop systems, 10 are found to be associated with flaring and CME onset originating from a connected active region. Transequatorial loop eruption leading to soft X-ray brightening is observed equally as often as dimming in the corona in association with CME onset. It was found that the same response to CME onset could not be guaranteed, even from the same transequatorial loop system. In addition, the likelihood of CME onset was found to be greater if the connecting loop was observed to extend over a wide range in both latitude and longitude. The implications of these results for CME prediction are discussed.

6.1: Introduction

The first direct observations of transequatorial interconnecting loops were made by Chase et al. [1976] using data from the Skylab soft X-ray imager. These authors identified 100 loops connecting 94 separate active regions. Loops were found to have an average length of 20° with a maximum 37° separation in heliographic latitude. More recent results [Pevtsov, 2000; Farnik, Karlicky & Svestka, 1999] have shown that this observed maximum was biased to lower values owing to the relatively short 9 month period of Skylab's operation, close to the minimum of solar cycle 21. During this period the average active region separation in latitude was confined within a narrow range.

Pevtsov [2000] studied interconnecting loops observed by the Yohkoh soft X-ray telescope [see Chapter 2 for a description of Yohkoh/SXT] during the period 1991 to 1998. This study incorporated observations made during the declining phase of solar cycle 22 through to the rising phase of cycle 23, thus removing any bias arising from the variation in active region latitude separation over the course of a solar cycle. This study

found the average footpoint separation of transequatorial loops to be approximately 30° with a maximum of 75°. To date, no observations of loops connecting regions in the *same hemisphere* with length greater then 30-35° have been made. This lack of observations led Farnik, Karlicky and Svestka [1999] to propose that an additional process must act on transequatorial loops in order to account for their increased length. This process would need to have little influence on loops confined to one hemisphere. Differential rotation was initially proposed as this additional mechanism. Further study by Pevtsov [2000] however, found 85% of active region pairs connected by transequatorial loop systems to rotate at similar rates in either hemisphere. It was therefore concluded that differential rotation would have a minimal effect on the evolution of these loop systems.

The origin of these long transequatorial loops is thought to be reconnection in the corona. Current models assume that active region flux is most likely to emerge from the photosphere independently in either hemisphere [e.g. Moreno-Insertis, 1986]. Thus, transequatorial loops should form via reconnection in the corona. Tsuneta [1996] presented observations of a transequatorial loop system which appeared to show an X-type neutral point in projection near disk centre. Tsuneta also noted the appearance of 'remarkable flare-like cusp structures' which formed as the region rotated towards the west limb. These did not appear to be directly related to reconnection, but were interpreted as evidence that the connection between two active regions constituted a larger "active area" within which reconnection could take place with less explosive consequences than normally observed in active regions.

A number of studies [e.g. Pevtsov, 2000; Svestka & Howard, 1981] have observed cases where a connection existed between an active region and a region of quiet-Sun situated in opposite hemispheres prior to the emergence of an active region in the connected quiet-Sun region. This is suggestive of reconnection taking place as the new active region flux emerges. Pevtsov found only one case where a transequatorial connection was observed to form between two mature active regions. In 40 out of 87 cases studied by Pevtsov, a mature active region was observed to be connected to a region of quiet-Sun, with a second active region appearing later in the relevant quiet-Sun area.

A number of studies have been undertaken with the intention of gaining insight into the origin and formation of transequatorial loops. However, these structures have only recently been associated with the onset of coronal mass ejections (CMEs) [Khan & Hudson, 2000]. These authors observed a series of homologous disappearances of an interconnecting loop system. Each disappearance was observed to take place in association with CME onset and a flare of M-class or above originating from one of the two connected active regions. The results of Khan and Hudson are important in the context of CME onset studies owing to their mass estimate for the quantity of coronal material disappearing from the vicinity of the transequatorial loop system in Yohkoh/SXT images. At 10^{15} g, this is of the same order of magnitude as a typical CME mass estimate and may, therefore, account for CME ejecta later observed in coronagraph data.

Harrison [1986] illustrated that flaring associated with CME activity frequently occurs at an asymmetrical position with respect to the material ejected during the CME. If the disappearing TLS does indeed represent the origin of CME material later observed in coronagraph images, this class of CME onset agrees with the observation of Harrison since associated flaring takes place within an active region located at one end of the disappearing loop system, prior to CME onset.

This study extends the findings of Khan and Hudson [2000], who analysed a single eruptive system of loops, to consider 18 interconnecting loop systems. This study investigates how often TLS are linked with eruptive solar activity, how the transequatorial loops respond to this activity and the possible influence of differential rotation. In total, 33 events were observed in association with 10 of these 18 TLS. The remaining 8 TLS were not associated with any significant CME activity during their lifetime. The implications of these results in terms of CME onset prediction are then discussed.

6.2 Data

For the purposes of this study, full disk Yohkoh SXT observations (resolution 4".9 & 9".8 per pixel) of 18 Transequatorial Loop Systems (TLS) have been considered [see Chapter 2 for a description of Yohkoh/SXT and other instrumentation used during this project]. These data were used to identify the TLS and study their morphology. Images taken using the Al.1 and AlMg filters were primarily studied. These are the thinner of the available SXT filters and, thus, provide the clearest observations of faint transequatorial loop systems.

In 16 cases out of 18, TLS were taken from the list published by Pevtsov [2000]. The Pevtsov list consists of 87 loop systems. However, for the purposes of this study it was decided to produce a comparison between SXT observations and data from the suite of instruments onboard SOHO. Consequently, only TLS observed after January 1996 could be incorporated into this study. A further two cases were neglected as they appeared very faint in SXT data. This reduced the number of applicable examples from the Pevtsov list from 87 to 16. Two further TLS, not previously included in the Pevtsov study, were also added to this list. A list of all TLS observed by Pevtsov [2000] between 1996 and 1998 can be found in Appendix B.

In order to determine whether any TLS was associated with a CME, comparison was made between SOHO/LASCO CME observations and changes in the TLS morphology observed throughout the period during which the loop system remained visible on the disk. In numerous cases, TLS brightening was observed in association with flaring from one or both of the connected active regions.

Determination of the CME onset site and further studies of the TLS morphology were made using EUV data from the SOHO/EIT telescope. EIT Fe XII (195 Å) data were available at one of two resolutions: 2".6 or 5".2 per pixel. EUV morphology changes were observed using the percentage difference technique described in Chapter 3.

In the event that a change in TLS morphology was observed in either EIT or SXT data, SOHO/LASCO coronagraph observations were studied. If a CME was observed during this period, a height-time extrapolation was applied to the data in order to estimate

CME onset time and location [a description of this technique can be found in Chapter 3]. CMEs were only disregarded if an origin other than that of the TLS or connected active regions under investigation could be determined from SXT or EIT disk observations. The origin of the CME was investigated by searching for one or more of the signatures listed below:

a. EUV dimming e.g. in the vicinity of the active regions or the TLS,
b. coronal waves or propagation of material,
c. flaring,
d. changes in brightness of the soft X-ray TLS,
e. prominence eruption or
f. formation of a cusp-shaped feature.

These features have been described several times in the literature [e.g. Hudson & Cliver, 2001] as being associated with CME onset and allow us to estimate the position of the CME launch site. Consequently, if one or more of these features were seen close to the onset time estimated through LASCO height-time extrapolation, CME onset was assumed to have taken place at that location.

6.3 Observations

The initial study by Khan and Hudson [2000] illustrated a series of disappearances in soft X-ray data of a single transequatorial loop system. Each of these disappearances was observed to be similar in appearance, and were termed "homologous" by the authors. Each of these disappearances took place in association with CME onset. Together with theoretical implications from the Babcock model of the solar cycle, these results have led to the assumption that transequatorial loop systems (TLS) will exhibit a high probability of eruption. However, of the 18 cases considered during this study, 8 showed no connection with CME activity, associated with the interconnecting loop system itself or one or more of the connected active region(s). The remaining systems did prove to be

associated with CME onset. These CMEs were observed to follow flaring activity in a connected active region.

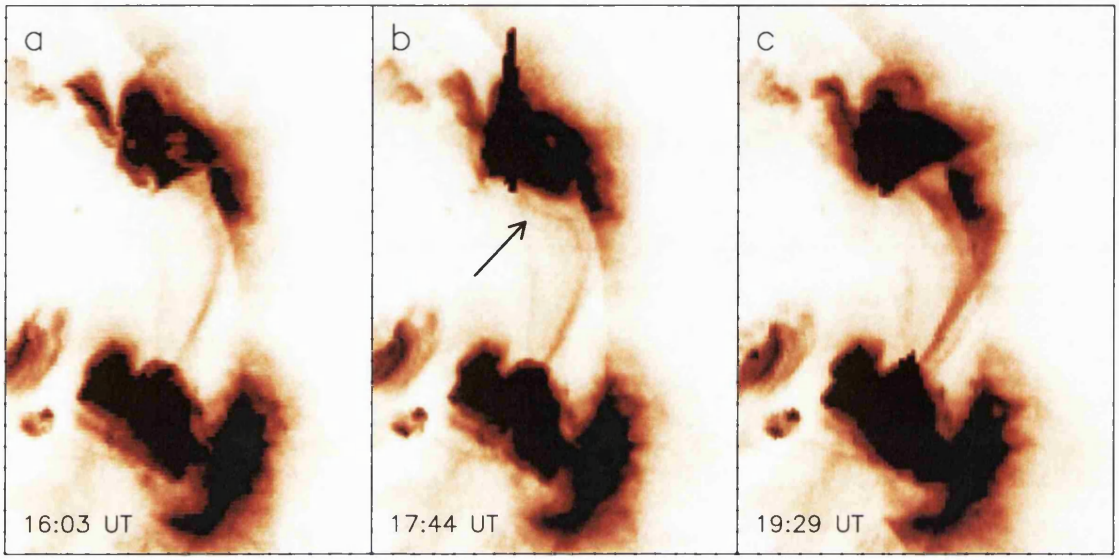

Figure 6.1: Sequence of images illustrating a Category A TLS as it forms an interconnecting cusp on 12th March 2000. Images are taken using the SXT AlMg filter at resolution 4".9 per pixel. The field of view of the images is 15'.6 by 22'.1 in each case. Figure (a) shows the pre-flare TLS, Figure (b) illustrates brightening of the northern active region (indicated by an arrow). Figure (c) illustrates a cusp shaped feature observed following CME onset. Solar north points up and east to the left. Images are displayed in reverse colours such that strongly emitting regions appear dark.

SXT and EIT 195Å data were initially surveyed in order to identify clear eruptive signatures of the TLS themselves in association with CME onset. An example of the formation of a bright cusp is shown in Figure 6.1. Formation of these features has been interpreted by previous studies as evidence of eruption [e.g. Tsuneta, 1992]. The temperature of the cusp that formed on the 12th March 2000 was determined using the filter ratio technique described in Chapter 3. Images taken using the Al.1 and AlMg filters were used for this purpose. The TLS reached an average temperature of 5.5 MK following the CME. Tsuneta [1996] found that the temperature of the TLS that he studied

Table 6.1: CME activity associated with Category A TLS. Dates on which CME activity was observed, number of active regions connected by the TLS and the eruptive signatures of the TLS themselves (where relevant) are listed. The homologous disappearances studied by Khan and Hudson [2000] are highlighted in blue.

CME Activity	Connected Ars	TLS Response to Eruption	North Location	South Location
10-Sep-97	2	dimming	N22E13	S25E40
21-Oct-97	1/QS	formation	N20E00	S09W02
2-May-98[a]	2	dimming/disappearance	N26E33	S17W10
4-May-98[a]	2	dimming	N27E06	S17W36
4-May-98[a]	2	none	N27E06	S17W36
6-May-98[a]	**2**	**disappearance**	**N27W23**	**S17W60**
6-May-98[a]	2	none	N27W23	S17W60
6-May-98[a]	2	none	N27W23	S17W60
7-May-98[a]	2	none	N27W34	S15W75
7-May-98[a]	2	none	N27W34	S15W75
8-May-98[a]	**2**	**disappearance**	**N28W48**	**Behind limb**
8-May-98[a]	2	brightening	N28W48	Behind limb
8-May-98[a]	2	dimming	N28W48	Behind limb
8-May-98	2	none	N28W48	Behind limb
9-May-98[a]	**2**	**disappearance**	**N28W61**	**Behind limb**
9-May-98[a]	2	none	N28W61	Behind limb
9-May-98[a]	2	brightening	N28W61	Behind limb
27-May-98[b]	2	dimming	N18W52	S24W89
27-May-98[b]	2	brightening	N18W52	S24W89
28-May-98[b]	2	brightening	N18W66	S24W90
29-May-98[b]	2	brightening	N18W81	Behind limb
29-May-98[b]	2	dimming	N18W81	Behind limb
29-May-98[b]	2	none	N18W81	Behind limb
29-May-98	2	disappearance	N26E21	S22W13
15-Oct-98	2	dimming	N15W12	S21W29
4-Nov-98	2	none	N18E07	S25W05
24-Nov-98	2	brightening	Behind limb	S18E71
24-Nov-98	2	none	Behind limb	S18E71
25-Nov-98	2	cusp+dimming	N17E77	S19E68
25-Nov-98	2	disappearance	N17E77	S19E68
5-Dec-98	2	none	N16E26	S16W06
12-Mar-00[b]	2	brightening	N24W45	S13W45
12-Mar-00[b]	2	cusp+dimming	N24W45	S13W45

a. Indicates that the TLS is also the system studied by Khan and Hudson
b. Indicates TLS not part of initial Pevtsov [2000] study

reached 7 MK. The average value for the diffuse corona in streamers has been determined by Foley et al. [2002] and was found to vary between 1.4 MK at solar minimum and 2.2 MK at solar maximum. It can, therefore, be seen that the 12th March 2000 TLS reached a temperature significantly above that of the quiet-Sun. The statistical study of Feldman, Laming and Doschek [1995], illustrated that a temperature of around 5.5 MK would be equivalent to the temperature reached during a low GOES B-class flare. A further example of TLS brightening in association with a CME is shown in Figure 6.4.

The 18 TLS analysed over the course of this study were separated into 2 categories as follows:

a. TLS and/or a connected active region was associated with CME activity and
b. neither the TLS nor any connected active region was associated with CME activity.

Table 6.1 lists the 33 eruptive events observed to originate with flaring in one or more of the active regions associated with the 10 TLS systems in Category A. In addition, TLS morphology changes are recorded in the column "TLS Response to Eruption" for Category A TLS. Table 6.2 lists those TLS unconnected with any significant CME activity. In both tables, the number of connected active regions ranges between 0 and 2 and indicates whether the ends of the TLS appear consistent with active regions on the disk. The northern and southern extents of the TLS are quoted in heliographic longitude.

Table 6.1 lists Category A TLS. There are 10 cases listed in this table showing evidence of the TLS itself being involved in the eruption leading to enhancement in soft X-ray images, with 2 of these developing into a cusp. This is in contrast to the disappearances observed by Khan and Hudson [2000], although it should be noted that both cases of cusp formation were followed by substantial dimming in the region of the TLS. In each case, EIT 195 Å observations of the interconnecting loop system located near to the west limb illustrate activity originating with flaring from one of the two connected active regions.

Table 6.2: A list of Category B lists TLS where no significant coronal mass ejections are observed in association either with the TLS themselves or a connected active region. '1/CH' indicates that a TLS is anchored between an active region and a coronal hole boundary. 'QS only' indicates that a TLS is anchored between regions of quiet-Sun. Dates are in accordance with Pevtsov [2000] and refer to the date on which the TLS appeared brightest since no associated eruptive activity was observed.

Date of Clearest Observation	Connected Active Regions	Northern Location	Southern Location
2-Feb-96	QS only	N20W07	S01W06
18-Dec-96	2	N18W15	S00W01
31-Jan-97	1/QS	N03E20	S00W28
23-May-97	1/QS	N02W13	S10W46
28-Dec-97	2	N20E41	S22E01
13-May-98	1/QS	N25W01	S20W05
16-Jun-98	QS only	N32E10	S17W08
15-Nov-98	1/CH	N20W07	S01W06

6.3.1 The Formation of Brightened Features in TLS

Figure 6.2 illustrates flaring of the northern active region during the 12th March 2000 event, as seen in EIT Fe XII (195 Å) observations. These images have been created using the percentage difference technique described in Chapter 3 and show regions undergoing a change in brightness of between ±20%. This sequence of images shows the event initiation occurring between 17:00 and 17:12 UT, when material can be seen to leave the northern connected active region. The appearance of the material leaving the region is similar to that of a coronal wave [e.g. Thompson et al., 1999]. However, if this feature is a coronal wave, it is of short duration and does not travel a large distance across the disk. The observed motion in EIT data corresponds to movement seen in the SXR TLS close to the northern active region during the same period. This is indicated in Figure 6.1b by an arrow.

The northern active region flare is followed by another flare of magnitude C6.4 from the southern connected active region. This flare peaks at 18:51 UT. A CME is observed in the north west quadrant of LASCO/C2 37 minutes later. Figure 6.1 illustrates

Yohkoh/SXT data for this period. The soft X-ray loops undergo brightening and morphology change to form a cusp shaped feature. This feature is initially observed at 19:03 UT (Figure 6.1c). Dimming was also observed in the vicinity of this TLS following cusp formation.

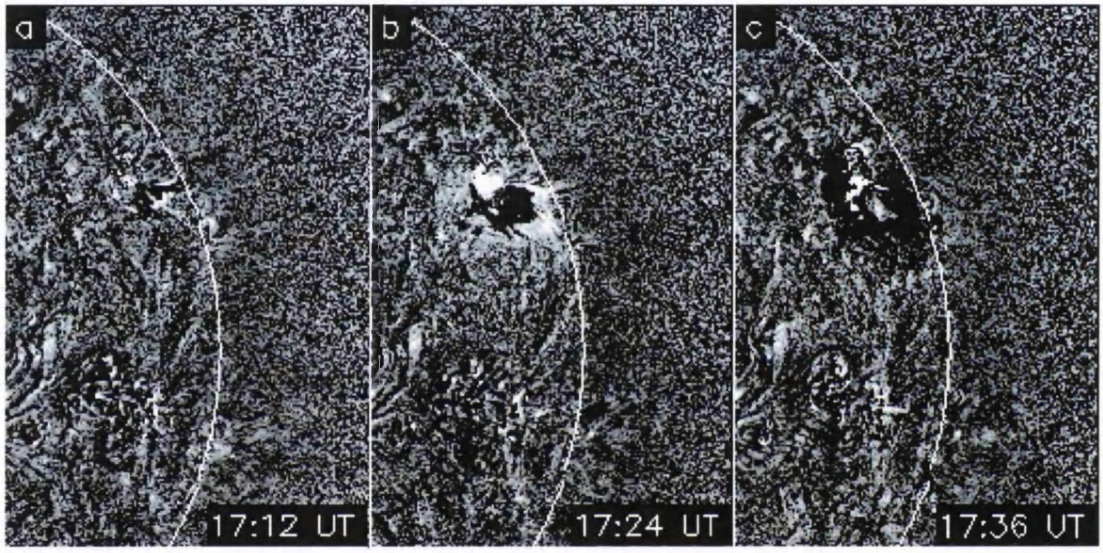

Figure 6.2: SOHO EIT 195 Å ±20% percentage difference images illustrating the eruptive TLS event onset on 12th March 2000. The field of view of the images is 15'.6 by 22'.1 in each case. The percentage difference technique causes the two active regions to appear dark in Figure (a). A bright region showing material moving away from the northern active region is observed in Figure (b) together with a brightening in the vicinity of the AR. Figure (c) illustrates dimming in the vicinity of the northern active region. Images are 5".2 per pixel resolution. Solar north points up and east to the left.

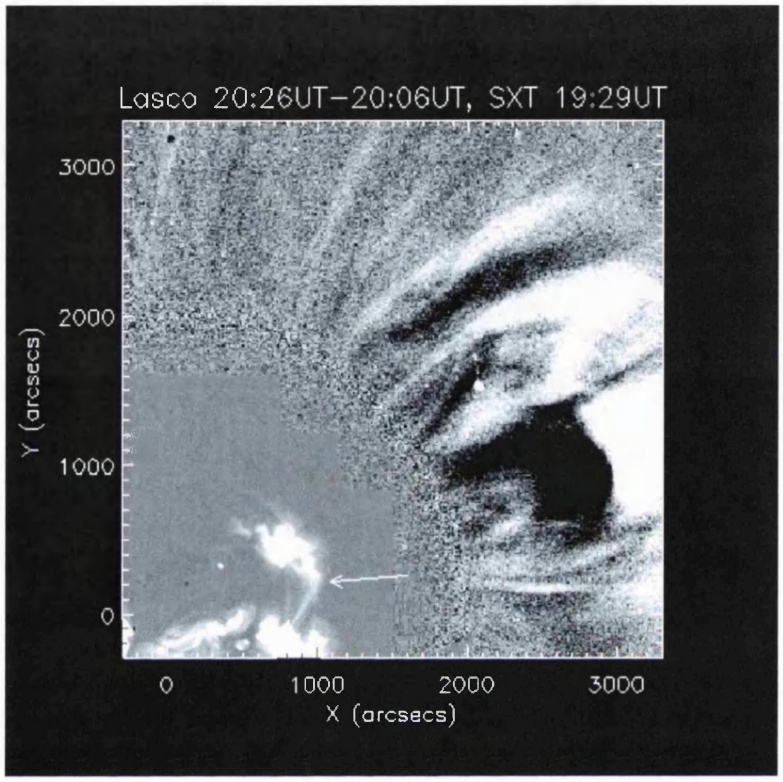

Figure 6.3: LASCO/C2 difference image (20:26 UT-20:06 UT) illustrating a loop-like CME associated with the 12th March 2000 cusp-forming event. The 19:29 UT SXT AlMg image is overlaid, showing that the CME's direction of propagation is consistent with the location of the northern active region and the TLS. An arrow highlights the position of the soft X-ray cusp shown in Figure 6.1.

Figure 6.3 shows LASCO/C2 data which illustrates the propagation of a loop-like CME through the north west quadrant of the C2 coronagraph at 20:26 UT. This took place 1 hour and 23 minutes after the cusp was first observed in SXT data. The TLS light curve shown in Figure 6.4 shows a gradual brightening of the cusp-shaped feature and a peak coinciding with the C6.4 flare onset. A second CME from this loop system also led to TLS brightening, but no cusp was observed in this case.

Figure 6.5 illustrates the changing intensity of another TLS observed using SXT during an event associated with CME onset on 29th May 1998. A diffuse collection of interconnecting loops illustrated in Figure 6.5a is observed to brighten in association with

CME onset (Figure 6.5b and c). Following activity from the northern connected active region, these loops take on a cusp-like appearance in projection situated above the west limb. This is illustrated in Figure 6.5c. Unfortunately, the full extent of this feature exceeds the SXT field of view and so this brightening cannot be classified as a cusp. Other CMEs related to this system produced a variety of responses in the TLS. These ranged from soft X-ray dimming to no response at all. Hence one consistent response to CME onset cannot be guaranteed, even from the same TLS.

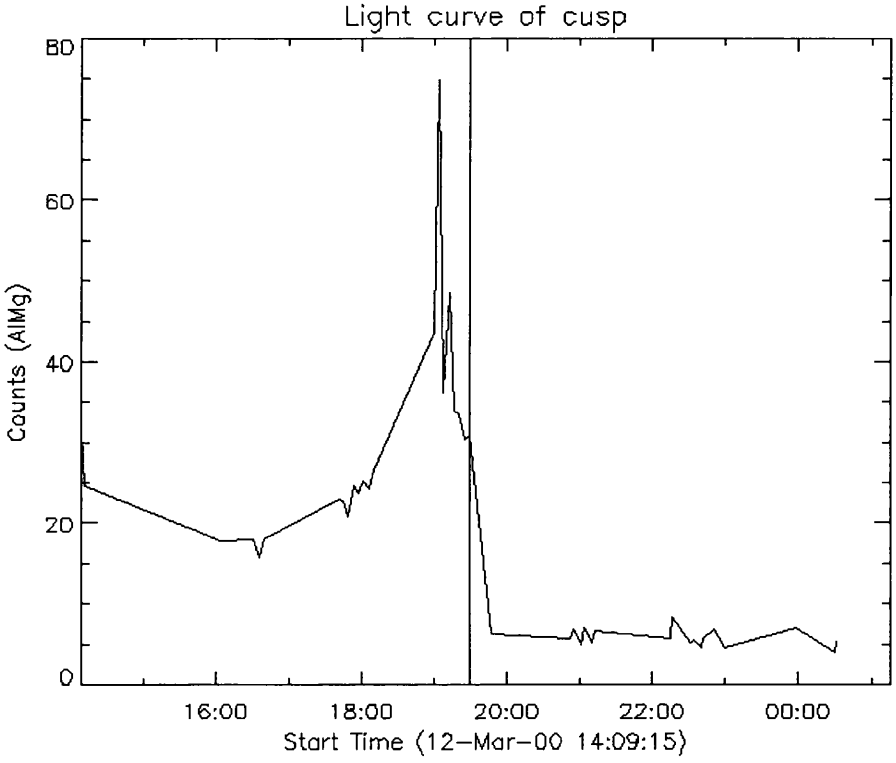

Figure 6.4: The SXT light curve for the cusp-forming region associated with the 12th March 2000 cusp-forming event. This curve illustrates how the feature brightens and then dims relative to the CME. A gradual brightening is observed starting at approximately 16:00. This is followed by a sharp peak that coincides with the C6.4 flare at 18:51UT. The vertical solid line indicates the first appearance of the CME in LASCO/C2 data at 19:28 UT.

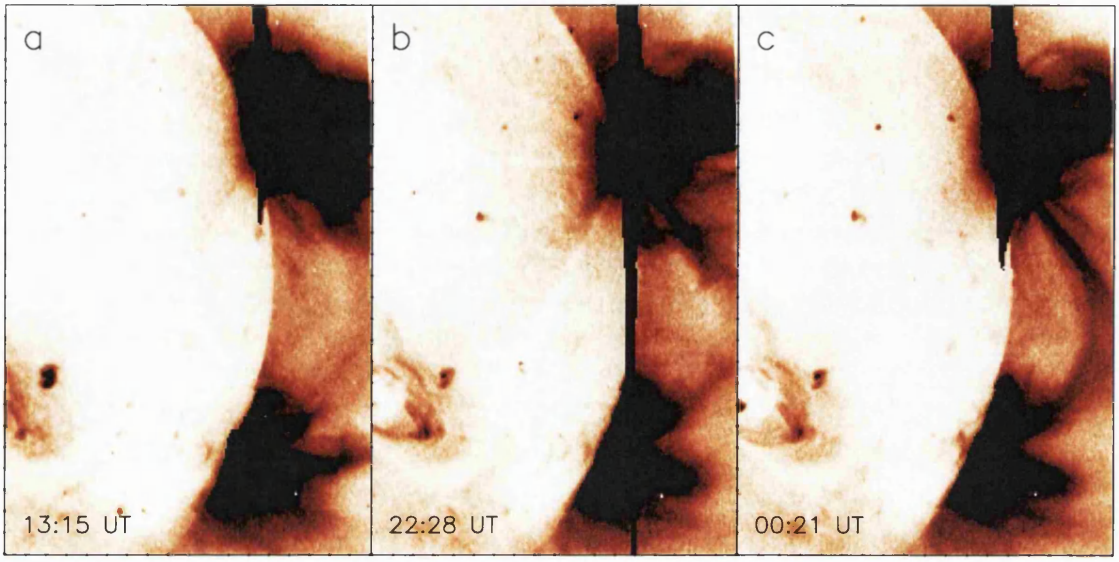

Figure 6.5: Yohkoh/SXT images showing soft X-ray brightening associated with CME onset on 29th May 1998. Figure (a) shows that a faint connection existed between the two active regions in soft X-ray data prior to the event. Figure (b), taken during the flare, shows an increase in soft X-ray intensity between the active regions and Figure (c) illustrates the formation of what appears to be an interconnecting cusp-shaped feature although the full extent of this feature is beyond the SXT field of view. Images are taken using the SXT Al.1 filter and have resolution 4".9 per pixel in each case. Solar north points up and east is to the left. Images are reverse colour such that strongly emitting regions appear dark. Saturation can be seen in each of the above three images. This can clearly be identified as the dark vertical streaks centred on the northern active region. Some scattered light can also be seen in Figure (b) as a faint halo also centred on the northern active region.

EIT 195 Å observations corresponding to the same time period as that illustrated in Figure 6.5 are illustrated in Figure 6.6. These observations show dimming taking place above the west limb confined within the latitudinal extent of the TLS. Following this dimming, the EUV counterpart of the TLS shows a change in loop morphology. Figures 6.6d, e and f illustrate brightening of the loop system taking place between 23:07 and 23:20 UT. This system is faint prior to eruption and is spatially consistent with the cusp-like loops seen in soft X-ray data (Figure 6.5c).

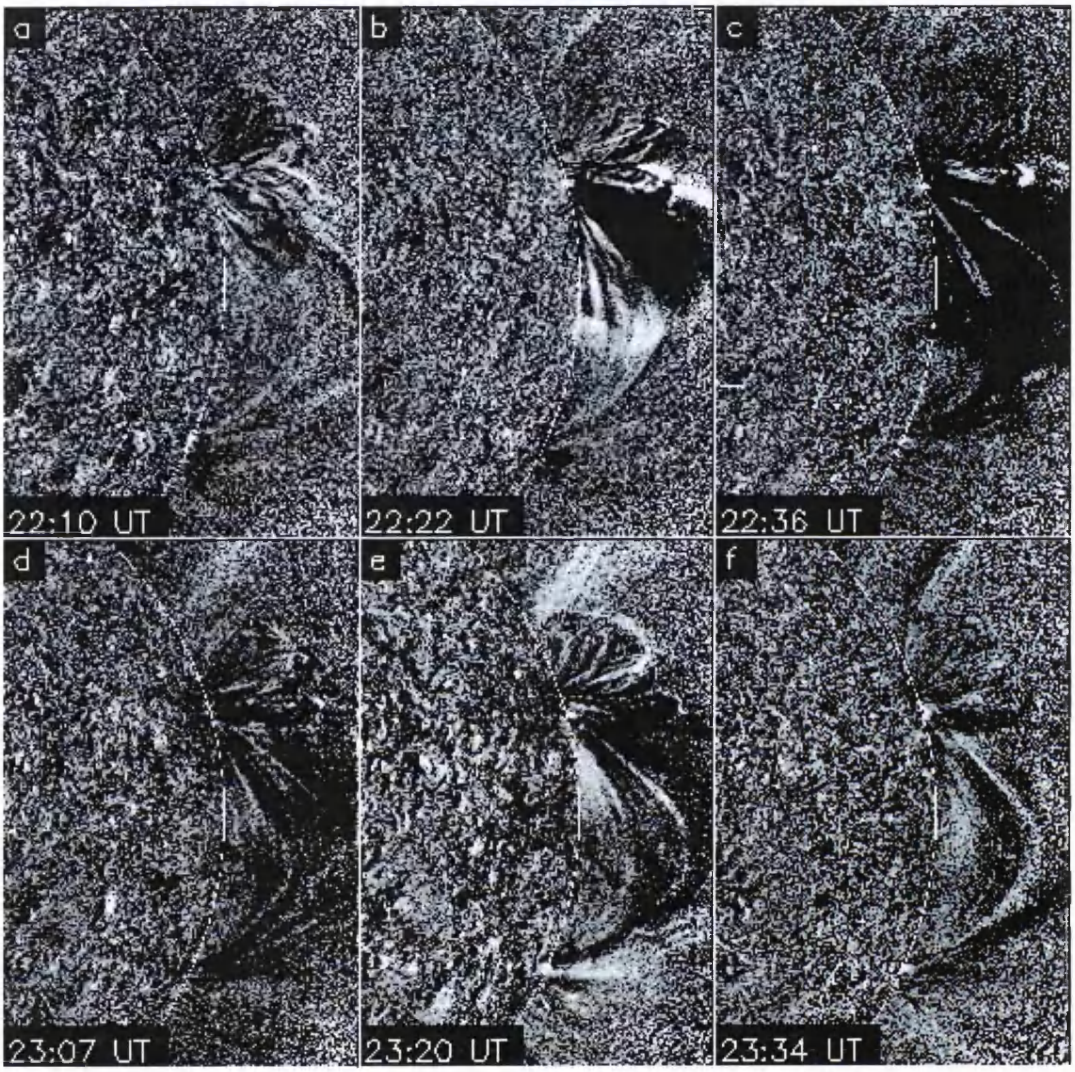

Figure 6.6: Coronal EUV dimming observed in association with CME onset on 29th May 1998. Images are percentage difference (±20%) and illustrate morphology changes observed in EIT 195 Å data at a resolution of 2".6 per pixel. Figure (b) illustrates evacuation of material from the vicinity of the northern active region. This dimming is seen to extend (c) to the width of the transequatorial loop system. Off limb brightening to the north of the dimming region (d, e, f) takes place as nearby coronal streamers are displaced by the eruption. Bright loops begin to appear in the dimming region (e, f) following eruption and prior to the first observation of the cusp-shaped feature in SXT (Figure 6.5). Solar north points up and east to the left.

Comparison of Figures 6.5 and 6.6 with LASCO/C2 and C3 data shows CME onset of the streamer blowout class [Howard et al., 1985]. An initial streamer enhancement is observed in the C2 field of view at 22:30 UT on 29th May. This extended out slowly into the corona without a clear front. Following this, and initially observed in C2 at 00:28 UT on the following day (30th May), a plasmoid is ejected along the same latitude. This two-part structure is frequently observed as a result of streamer disruption [Andrews & Howard, 1999; Sheeley et al., 1982].

Comparison with EUV dimming observed in Figure 6.6 shows that the plasmoid ejection is observed by LASCO several hours after the initial dimming onset. The first observation of the streamer enhancement in C2 data is, however, closely related in time to both the initial EUV dimming and brightening observed in SXT data at 22:28 UT.

6.3.2 Disappearance and Dimming in TLS

Table 6.1 lists 6 events where TLS undergo disappearance in association with CME onset. Of these 6 events, 3 are from the region studied in detail by Khan and Hudson [2000]. This system of loops undergoes a series of 3 homologous disappearances in soft X-ray observations. A further disappearance (or dimming) of this system in connection with CME onset was identified by Wang et al. [2002] on 2nd May 1998. However, Yohkoh spacecraft night meant that it was not possible to determine whether a sudden disappearance or gradual dimming of the TLS took place in this case.

In these four cases, eruption leads to a *dimming* in soft X-ray emission observed in association with flaring and CME onset. This contrasts with the brightened structures described in the previous section. Of the 33 CME onset events considered for the purposes of this study, 14 show either a disappearance of the type observed by Khan and Hudson or a slow dimming following CME onset. Of these 14 examples, 2 show cusp formation prior to dimming. Figures 6.7b and c illustrate a TLS that remained intact following CME onset but faded gradually over a period of several hours.

6.3.3 Gradual Brightening and Dimming of a TLS

Figure 6.7 provides an example of gradual soft X-ray brightening and dimming observed in one of the TLS. In this case, 2 CMEs are observed to originate from the northern active region. Neither CME appears to have a direct effect on the TLS morphology: the TLS appears unchanged in SXT data directly following flaring and the estimated CME onset time. Instead, a gradual brightening of the soft X-ray loops is observed over a period of hours following the first CME onset (Figure 6.7b) and a gradual dimming is then observed over several hours following the second (Figure 6.7c).

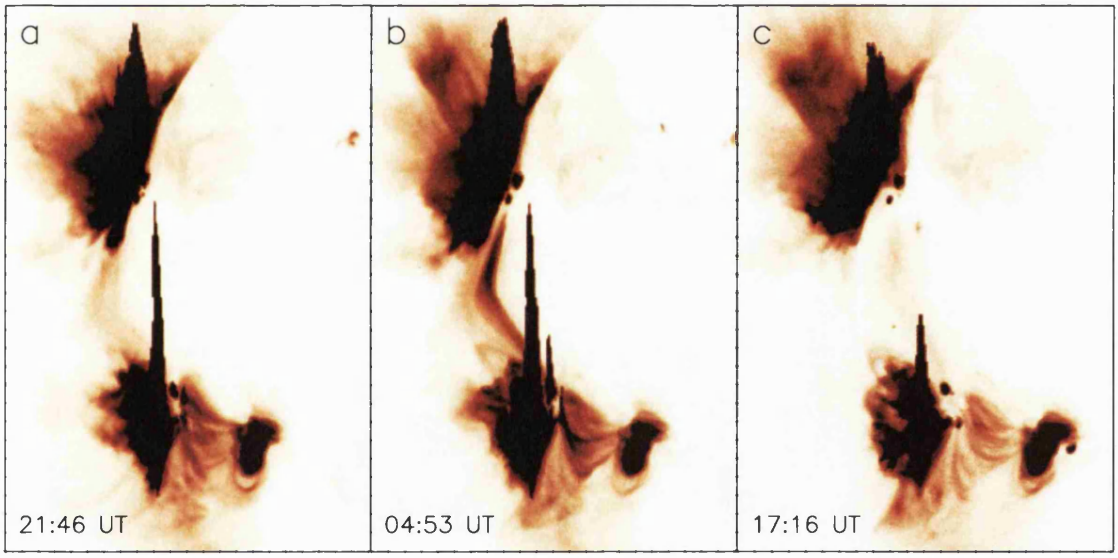

Figure 6.7: Yohkoh/SXT data from 24th and 25th November 1998 illustrating TLS morphology changes associated with CME onsets on 25th November 1998. Two CMEs take place on 25th November. In both cases the TLS remains unchanged after CME onset. This figure illustrates gradual changes in brightness over a 20 hour period surrounding the two CMEs. The field of view of the images is 18'x24' in each case. Brightening is observed in Figure (b) following the first onset at 04:40 UT, while a gradual dimming (indicated in Figure (c)) of the TLS occurs following the second onset at 12:15 UT. SXT data has 4".9 per pixel resolution. Solar north points up and east to the left. Images are reverse colour such that strongly emitting regions appear dark. Saturation can be seen in each of the above images as dark vertical streaks centred on the active regions.

The gradual dimming described here differs from the type observed by Khan and Hudson [2000] as no sudden decrease in emission is observed. In this case, the TLS remains intact following CME onset, fading gradually over a period of hours during which flaring activity continues from the two connected active regions.

6.3.4 The Appearance of a TLS in Association with Coronal Activity

The 21st October 1997 event showed no transequatorial connection in Yohkoh/SXT data prior to CME onset. In this case, loops were observed to form across the equator between an active region and an area of quiet-Sun following CME onset and flaring from the northern active region (Figure 6.8). Comparison with EIT 195 Å data shows no comparable EUV dimming at this time. Consequently, the bright soft X-ray loops may have formed as a result of the eruption. The newly formed loop system gradually fades over a period of days, without an associated eruption.

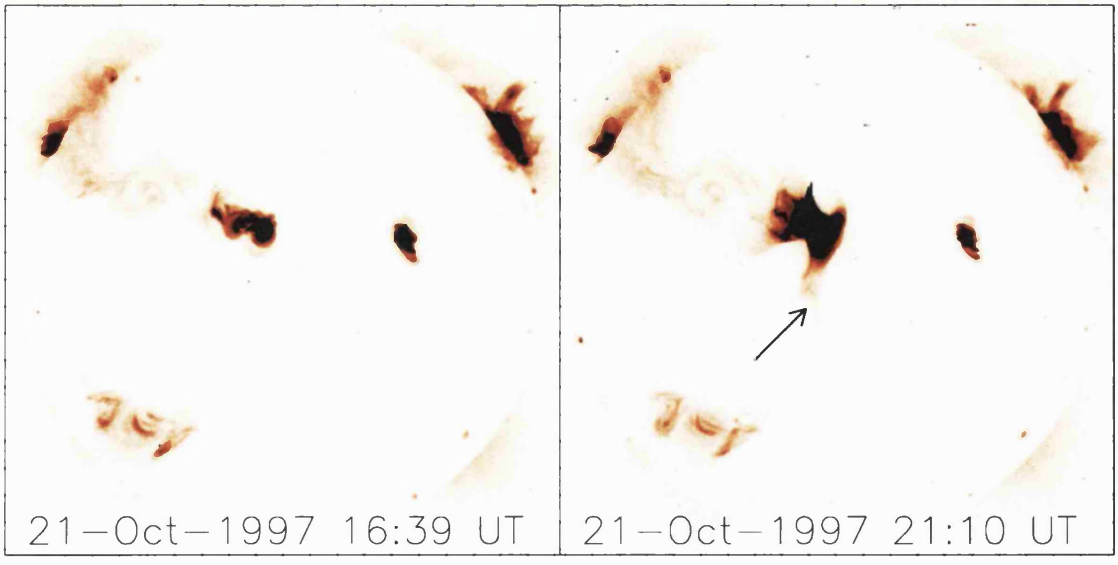

Figure 6.8: Yohkoh/SXT data illustrating the appearance of a transequatorial connection in soft X-ray data following activity in AR 8097 on 21st October 1997. An arrow indicates newly formed connections which are then seen to fade gradually over a period of several hours. SXT data has resolution 4".9 per pixel. Solar north points up and east to the left. Images are displayed in reverse colour such that emitting regions appear dark.

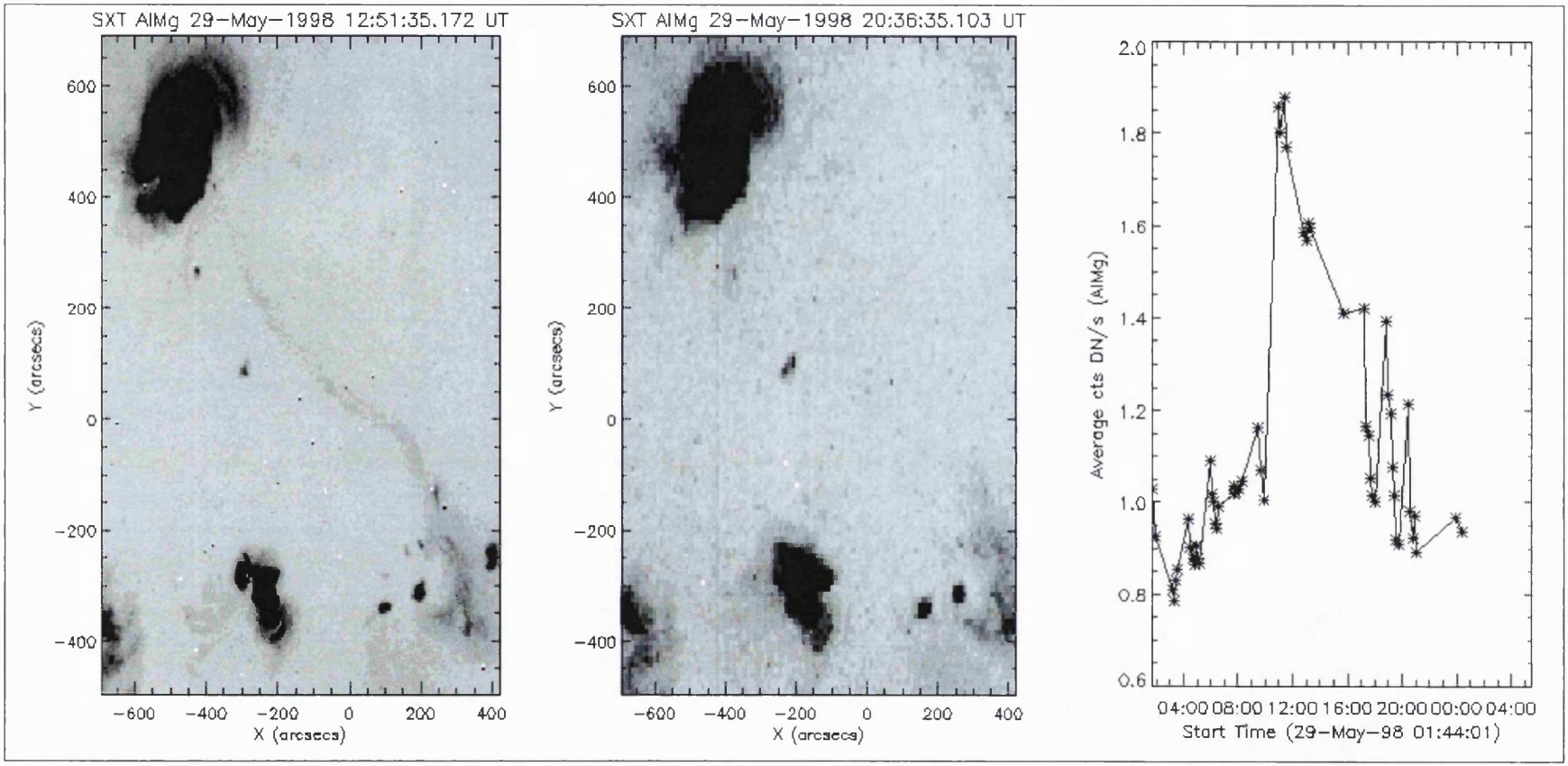

Figure 6.9: SXT observations of a short-lived TLS visible on disk on 29th May 1998, together with a light curve for the same period. The first two panels illustrate SXT observations of the TLS observed on disk with north and south location N26E21 and S22W13 (from Table 6.1) prior to and following CME onset. The third panel contains the TLS SXT light curve for this period showing the decrease in intensity back to background levels.

Figure 6.9 shows a second TLS visible to the east of the central meridian on 29th May 1998. A gradual increase in the SXT light curve of this region was seen at 09:30 UT followed by brightening in the lead up to CME onset at 11:43 UT. Dimming and disappearance were then observed after a second CME at 17:38 UT. This disappearance is illustrated by a light curve and shows the lifetime of this TLS to be about 16 hours. This was one of the shortest lived TLS considered during this study.

6.4 Discussion

The series of homologous eruptions studied by Khan and Hudson [2000] each occurred in association with a flare of magnitude M3.1 or above. Each CME onset considered as part of the present study of 18 TLS was also accompanied by flaring from one or more of the connected active regions.

While the TLS studied by Khan and Hudson [2000] disappeared on three consecutive occasions in association with flares of M-class or above, the occurrence of an M-class flare does not appear to be a requirement for eruptive interconnecting loops. The TLS involved in the series of events from 27th-29th May 1998 ending with TLS brightening, was connected to active regions both associated with flaring and CME onset as the system rotated around the west limb. In this case, the TLS did not disappear or brighten significantly in association with the strongest flare (GOES M6.7 class) associated with the connected active regions. In both cases described in Section 6.3.1, flares associated with CME onset were C-class, rather than the M- and X-class events that were associated with the eruptions studied by Khan and Hudson.

The TLS studied by Khan and Hudson [2000] was connected to NOAA AR 8210 in the southern hemisphere. This active region has been the subject of a number of studies owing to its unusually active nature for the period of the solar cycle during which it was observed. Warmuth et al. [2000] describe the evolution of this region in white light and Hα data. Sterling and Moore [2001] also studied this region in terms of its sigmoidal morphology and a series of homologous flares occurring on the 1st and 2nd May 1998, just prior to the appearance of a clear transequatorial connection between active regions.

As mentioned in the introduction, Pevtsov [2000] found 85% of 87 TLS to have footpoints in either hemisphere separated in latitude such that the difference in rotation rate experienced by the two regions would be less than 1°/day. Thus it was assumed that, in the majority of cases, differential rotation would not have significant effect on the morphology of the TLS.

In order to confirm this result for the present TLS sample and determine whether a connection might exist between a difference in rotation rate of the two footpoints and the TLS probability of eruption, it was decided to calculate the deviation from symmetry about the equator of those TLS found to be associated with CME onset.

Table 6.3: Dimensions of Category A & B TLS. Asymmetry of TLS about the equator, together with the extent of the TLS in longitude and latitude in degrees. The blue line separates Category A TLS (above) from Category B (below).

Date	Asymmetry (latitude)	Longitudinal Extent	Latitudinal Extent	Number of ARs
10-Sep-97	3	27	47	2
21-Oct-97	11	2	29	1
6-May-98	10	37	44	2
27-May-98	6	37	42	2
29-May-98	4	34	48	2
15-Oct-98	6	17	36	2
4-Nov-98	7	12	43	2
25-Nov-98	2	9	36	2
5-Dec-98	0	32	32	2
12-Mar-00	7	29	41	2
2-Feb-96	19	1	21	0
18-Dec-96	18	14	18	2
31-Jan-97	3	48	3	1
23-May-97	8	33	12	1
28-Dec-97	2	40	42	2
13-May-98	5	4	45	1
16-Jun-98	15	18	49	0
15-Nov-98	19	1	21	1

The asymmetry in latitude of the footpoints was found by calculating the difference in latitude in each hemisphere of the footpoints. The extent in latitude, used here to give a measure of loop length, was then determined by summing the latitudinal

position of each footpoint. The extent of the loop in longitude was also measured. Table 6.3 illustrates these results. Using these values to determine the difference in rotation rate at each end of the TLS gives a maximum difference of only 0.3°/day. Thus, a gradual buildup of shear over a number of days would be required if differential rotation were the cause of TLS eruption. If it is assumed that the loops form as they appear in soft X-ray data, the action of differential rotation would be insufficient to cause strong shearing within the TLS. On average, the events that are not related to a CME have a mean latitudinal asymmetry of 11.1°, a longitudinal extent of 19.8° and a latitudinal extent of 26.4°. For those events that are associated with CMEs, the mean latitudinal asymmetry is lower at 5.1°, but both longitudinal and latitudinal extent are, on average, larger having an average of 23.6° and 39.8° respectively. These results are reproduced in Table 6.4.

The above results suggest that the asymmetry in latitude is not important for the eruption of a TLS. It is more important for the TLS to be extended (no TLS associated with one or more CMEs had an extent in latitude less than 29°) in both latitude and longitude.

Table 6.4: Comparison of average Category A and B TLS latitudinal asymmetry, longitudinal asymmetry and latitude difference.

TLS Category	Latitudinal Extent (°)	Latitudinal Asymmetry (°)	Longitudinal Extent (°)
(A)	39.8	5.1	23.6
(B)	26.4	11.1	19.8

6.5 Conclusions

This study provides the first survey of transequatorial interconnecting loops in terms of their eruptive characteristics. These eruptions can lead to a variety of different signatures including the formation of bright, soft X-ray cusp-shaped features interconnecting active regions. In contrast, there are occasions where the TLS is observed to fade either gradually over a period of several hours or suddenly, as observed by Khan and Hudson

[2000]. There are also events where the loop appears to remain unchanged by the eruption even though the eruption clearly originates from one of the connecting active regions. Taking into consideration that the region studied by Khan and Hudson was one of unusual complexity and high activity, the study described in this chapter illustrates that transequatorial loops may possess eruptive character, but this is certainly not true of every example. Eruption may also be associated with only moderate, C-class levels of flaring. A flare of magnitude greater than M-class is not necessary for a TLS to show eruptive characteristics. It is more common for a TLS to show response to CME onset at EUV and soft X-ray temperatures if one or more of the following criteria are met:

a. if two active regions are involved,
b. the TLS is extended or
c. the extent in longitude is high.

This study considers a relatively small sample of transequatorial loop systems. A larger sample may provide further examples of interconnecting soft X-ray brightenings or dimmings formed as a result of CME onset. This may also help to address the question of whether projection effects influence the observation of brightened eruptive features in TLS. It should be noted that all interconnecting cusp observations made during this study occurred when the relevant system was approaching the west limb, as illustrated in Table 6.1.

6.6 Summary

- This study provides the first survey of transequatorial loop systems (TLS) in terms of their eruptive character.
- Examples of TLS brightening following flaring and CME onset are equally as common as examples of dimming or disappearance.
- All TLS do not respond in the same way to CME onset

- In cases where the TLS forms a cusp-shaped feature following CME onset, the TLS itself may be heated to temperatures equivalent to those observed during a GOES B-class flare.
- TLS appear most likely to erupt if they are extended in both longitude and latitude.
- For TLS associated with CME onset, the asymmetry about the equator is small, thus suggesting that shear would not be induced in the TLS through the action of differential rotation.

Chapter 7

Conclusions and Further Work

7.1 Sigmoidal Solar Features

This thesis has studied sigmoidal solar features on a variety of size scales. It begins with a multi-wavelength survey of sigmoidal active regions and extends this with a detailed study of the formation and evolution of a large scale S-shaped feature unconfined by a single active region.

7.1.1 Summary of Sigmoidal Active Region Study Results

Chapter 4 incorporates a multi-wavelength study of sigmoidal active regions, each of which had initially been classified as "sigmoidal" and "eruptive" by Canfield, Hudson and McKenzie [1999]. The initial survey was extended to include white light coronagraph data together with EUV and Hα observations of the solar disk. The SXT soft X-ray data used to classify each active region according to morphology was also increased in resolution from 5-10" per pixel to 2".45 per pixel where available. This led to reclassification of the regions classified as *sigmoidal* by Canfield, Hudson and McKenzie as follows:

- *Sigmoidal*
- *Projected-sigmoidal* and
- *Non-sigmoidal*

where the *sigmoidal* category refers only to soft X-ray features that appeared to consist of a single structure at Yohkoh/SXT full resolution (2".45 per pixel). Regions classified under the *projected-sigmoidal* category did not appear to consist of a single structure at

increased resolution. Instead, at higher resolution, their sigmoidal appearance was observed to comprise several smaller loops aligned in such a way that they appeared S- or reverse-S shaped at the lower (5"-10" per pixel) resolution. Whilst these regions could be described as complex, they did not appear to represent observations of a helically twisted flux rope, as described by Rust and Kumar [1996]. The reclassified *non-sigmoidal* active regions did not possess any clear sigmoidal appearance at increased resolution.

This extended survey found that regions having clearly defined sinuous S (or reverse-S) like morphology do possess the strongest tendency to erupt with the formation of an associated CME, coronal EUV dimming and, on occasions, a coronal EIT wave. Those regions falling into the *projected-sigmoidal* category show a higher probability of eruption than *non-sigmoidal* active regions, but lower than the reclassified sigmoidal category.

Following description of this survey, Chapter 4 includes a more detailed description of two sample active regions. Each of these regions was previously classified as "sigmoidal" and "eruptive" by Canfield, Hudson and McKenzie [1999]. However, these regions were chosen for further description here as examples from each of the reclassified *sigmoidal* and *projected-sigmoid* categories in order to compare their structure and the processes involved in their eruption.

Both active regions were shown to form a transient S- (or reverse-S) shaped structure *after* the initial rise in GOES X-ray emission associated with flaring but *prior* to material being ejected. In each case the sigmoidal feature is visible for under an hour prior to eruption.

Comparison with proposed models for sigmoid eruption, suggests that the first active region (AR 8092) erupts by means of a mechanism close to that of the "sigmoid expansion" model described by van Driel-Gesztelyi et al. [2000] and Manoharan et al. [1996]. This model requires the presence of additional flux systems in order that reconnection, and removal of the overlying field, can take place prior to eruption of the underlying sigmoidal core flux.

The second example region also illustrates external connections that form in association with eruption. However, this active region does not appear to erupt by means

of the same process. A temperature map shown in Figure 4.15 illustrates a temperature discontinuity along the sigmoid axis. This suggests that more than one feature may be observed in projection, thus leading to the region's overall sigmoidal appearance. Further evidence that the reverse-S shaped feature does not constitute a single structure was found when a force-free field extrapolation applied to the data proved unable to reproduce the feature's observed level of twist. Prior to the active region's eruption, the initially straight filament gains an additional curved channel spatially consistent with the eastern "elbow" of the reverse-S shaped feature. This erupts soon after formation leading to a filament layer eruption along the main active region neutral line, associated flaring and CME onset. Consequently, rather than the "expanding sigmoid" scenario attributed to the eruption of AR 8092, it is thought that the eruption of AR 8097 is associated with changes in the underlying filament.

7.1.2 Summary of Non-Active Region Sigmoid Study Results

Chapter 4 describes studies of sigmoidal features confined within strong active region fields. In contrast, Chapter 5 considers the formation and evolution of a large scale sigmoidal feature that formed within the decayed, weak field, remnants of a large active region.

This study follows the evolution of NOAA active region 8906 over three rotations. Sigmoidal features are observed during both the second (April) and third (May) rotations whereas no appreciable sigmoidal structure had been observed during the first (March) rotation.

Measurement of the increased extent in latitude of the region over the three observed rotations shows that differential rotation would be unable to reproduce the observed increase in extent alone. Therefore, a combination of factors must lead to the observed increase over the three rotations. This may have included the action of emerging flux already in possession of significant twist prior to its emergence through the photosphere [Emonet & Moreno-Insertis, 1998], the action of large scale surface flows causing flux diffusion or flux cancellation taking place along the neutral line.

Flaring and CME activity associated with AR 8906 is also evaluated over all three rotations. A high rate of both flaring and CME onset is observed during the first two rotations. The flaring rate decreases following the second rotation. Only 1 flare took place during the third (May) rotation. However, two CMEs are observed during this final rotation. Comparison of flaring and CME rates shows that an increased CME onset rate coincided with the appearance of a sigmoidal feature in the active region during the April rotation. This sigmoidal feature appeared in association with emerging flux and flaring but did not disappear in direct association with a particular CME.

During the final rotation, the sigmoidal appearance of the region is strongest *after* CME onset and flaring had taken place on the 8th May 2000. Gradual disappearance of the post-flare arcade following this event leads to a decrease in the sigmoidal appearance of the region. Finally, continued CME activity on 10th May 2000 leads to formation of a diffuse arcade and the stored energy content of the region appears to be greatly reduced.

7.1.3 Further Research into Sigmoidal Solar Features

Chapter 4 describes an extended survey of active regions previously classified as both sigmoidal and eruptive by Canfield, Hudson and McKenzie [1999]. In order to extend this survey, it was decided to produce a comparison between eruptions observed by the Yohkoh/SXT and data available from instruments onboard SOHO. Unfortunately this reduced the sigmoidal active region dataset to half its initial size and resulted in only a few active regions having sufficient data coverage to be reclassified into each of the three categories; *sigmoidal*, *projected-sigmoidal* and *non-sigmoidal*. At the time of writing, the SOHO spacecraft has been in operation for 7 years during which time, until December 2001, the Yohkoh observatory made routine soft X-ray observations of the solar corona. Thus an extended survey incorporating several years' observations and comparison between data from the two spacecraft would lead to better statistics and a more reliable estimate of the probability of sigmoid eruption.

The detailed comparison of two active regions described in Section 4.4 illustrates two examples where the active region gains its S (or reverse-S) like appearance *after* the

initial rise in GOES flux signaling flare onset. Thus, the sigmoidal/projected-sigmoidal feature forms in association with activity in the region rather then being present in the corona beforehand. However, both regions appear to erupt through different processes, thus highlighting the situation that, as yet no single model is able to reproduce or account for all sigmoid eruptions. In both cases described in detail in Section 4.4, the eruption is more complex than that of a simple bipole. Other field structures external to the active region are involved in each case.

Chapter 5 provides a qualitative, description of a large scale sigmoidal region. This study could be expanded to incorporate helicity calculations derived from magnetic field measurements e.g. Demoulin et al. [2002]. These calculations could be used to determine whether the appearance of sigmoidal features in this region gives an indication of stored magnetic helicity. Comparing the variation in the level of helicity stored within the region with the rates of flux emergence and CME onset would also help to establish whether differential rotation or emerging flux is the more dominant source of magnetic helicity. In addition, this might indicate whether CME onset does indeed remove a significant fraction of the region's stored helicity. This technique could then be applied to other regions for comparison in order to determine the role of CMEs in the Sun's helicity budget.

In conclusion, the results described in this thesis illustrate the need for a more quantitative definition of the term "sigmoid". Questions include whether an active region should be classified as sigmoidal if its morphology appears to comprise a single structure or if an overall S-like appearance, consisting of many loops is sufficient for sigmoidal classification. Further study may also indicate whether it is necessary that a sigmoidal region should form a single twisted flux rope for eruption to take place or whether an overall S-shaped alignment of loops provides sufficient indication that eruption might occur. Furthermore, what degree of twist would a sigmoid need in order to be classified as sigmoidal and potentially eruptive? The answer to this question may arise from studies of shear and magnetic complexity within sigmoidal active regions. A recent study by Falconer, Moore and Gary [2002] proposed a method by which vector magnetogram data might be used to measure the degree of magnetic helicity stored within active region

fields and provide a more quantitative estimate of the likelihood of eruption for these regions.

Multi-wavelength studies of sigmoidal active regions are currently being undertaken, illustrating a number of interesting features. Gibson et al. [1999] compared the alignment of sigmoidal active regions as observed at different temperatures. Unlike the alignment of filament and SXT sigmoid described in Section 4.4.2, Gibson et al. have consistently found sigmoids observed at EUV temperatures using the SOHO Coronal Diagnostics Spectrometer (CDS) [Harrison et al., 1995] to be rotated with respect to their appearance at soft X-ray temperatures. Although not directly related to CME onset, these observations may prove important to understanding the 3-dimensional nature of sigmoidal active regions and the changes they undergo in association with CME onset.

The advent of the STEREO (Solar TErrestrial RElations Observatory) spacecraft, currently scheduled for launch in late 2004, will lead to a greater understanding of the connection between sigmoidal features and CME onset. STEREO will consist of two spacecraft. The SECCHI instrument [Howard, Moses & Socker, 2000] will provide complementary views of the solar corona in EUV and white light coronagraph data. The complimentary EUV views will allow observation of sigmoidal features from more than one position. Currently, and by definition, a sigmoid can only be observed in projection towards the centre of the solar disk, thus preventing the same feature being classified as sigmoidal after it has begun to rotate towards the limb. The ability to view the same feature from more than one angle will provide information about whether the sigmoidal feature is indeed a single structure.

7.2 Transequatorial Loop Systems

7.2.1 Summary of Transequatorial Loop Study Results

Chapter 6 of this thesis describes the first survey of transequatorial loop systems in terms of their eruptive character. This follows on from the study carried out by Khan and Hudson [2000] which considered only a single loop system. These authors observed a

series of homologous disappearances of a transequatorial loop system, each in association with a flare of M-class or above. The survey described in Chapter 6 considers 18 transequatorial loop systems (TLS) in terms of their eruptive characteristics.

This study found that transequatorial loop brightening was observed equally as often as dimming in association with CME onset. Cases were also found where no change was observed in the TLS, despite the observation of a CME from an active region appearing connected to the TLS in soft X-ray or EUV data.

This study of 18 different TLS illustrates a wide variety of possible responses to CME onset. However, a TLS does appear more likely to exhibit eruptive character in response to a CME if one or more of the following criteria are met:

a. if two active regions are involved: i.e. one at either end of the TLS,
b. if the TLS is extended in latitude and/or
c. if the TLS is extended in longitude.

All of the CMEs observed in association with TLS eruption during this study were associated with flaring. However, it appears that TLS eruption does not depend on flare strength. TLS brightening and dimming were both observed in association with CME onset following flaring of GOES C-class strength. In addition, the average asymmetry of eruptive TLS about the equator was lower than for those TLS that were not eruptive.

Taking into account that the region studied by Khan and Hudson [2000] was one of unusual complexity and high activity, the study described in this chapter illustrates that transequatorial loops may possess eruptive character, but this is not true of every example.

7.2.2 Further Research into the Connection between Transequatorial Loop Systems and CME onset.

This study has considered the eruptive character of 18 transequatorial loop systems. Consequently the number of eruptive loop systems observed is small. An extended survey could be carried out to incorporate additional TLS observed during the period between the last case considered as part of the Pevtsov [2000] study and the date on which Yohkoh ceased operation (1998-2001). This would provide other eruptive loop systems for comparison.

Table 6.1 illustrates that in all but a single case, TLS show eruptive character only when 2 active regions are involved. A study by Canfield, Pevtsov and McClymont [1997b] has illustrated that transequatorial connections in the corona will preferentially form between active regions with the same sign of helicity (chirality). Determination of the helicity possessed by the connecting loops may indicate changes in this value prior to eruption, possibly due to the influence of flux emergence in the connected active regions. In this way, helicity would be added to the system through the action of reconnection between emerging flux, already in possession of significant twist, with existing transequatorial loops in the corona. An erupting TLS would then act to remove this helicity.

One uncertainty in Chapter 6 results arises from the potential influence of projection effects on transequatorial loop observations. The eruptions leading to interconnecting cusp observations take place when the TLS are located close to the west limb. Tsuneta [1996] also referred to the appearance of 'remarkable flare-like cusp structures' forming in a TLS as the system approached the west limb. This is suggestive of a projection effect leading to bias in the observation of erupting TLS. The advent of the Solar TErrestrial RElations Observatory (STEREO), will allow the same feature to be viewed from two separate angles at EUV wavelengths by means of the SECCHI Extreme-Ultraviolet Imagers (EUVI). The STEREO mission will consist of two identical spacecraft that will be launched into heliocentric orbit, one leading the Earth and the other lagging behind in its orbit. Separation between the craft will be gradually increased

during the mission. Combined with soft X-ray observations from the GOES Soft X-ray Imager (SXI) which has recently begun taking regular images of the corona, these observations will provide additional information on TLS and will reduce bias caused by the orientation of the feature with respect to the observer.

Acknowledgements

First and foremost, I would like to thank my supervisor Louise Harra. Her drive and commitment to her role as supervisor over the last three years has proved invaluable and for which I am very grateful.

My arrival at MSSL to join the Space Plasma Group unfortunately coincided with my original supervisor, colleague and friend, Professor Alan Johnstone, being taken ill with cancer. Unfortunately he was not to return from this, leaving an uncertain time for the entire group. I would like to thank all those that offered advice and support during this period, a difficult time for everyone who knew or worked with Alan. Specifically, Andrews Coates and Fazackerley, Louise Harra and Len Culhane at MSSL, Eamonn Daly and Alain Hilgers at ESA/ESTEC and Daniel Heynderickx at BIRA-IASB.

Thanks to Sarah Matthews, Len Culhane, Lidia van Driel-Gesztelyi, Keith Mason, Kuniko Hori, Neale Ranns, Carl Foley, Lucie Green and Gareth Lawrence for helpful comments and advice. Thanks also to Daniel Brown from St Andrews University for advice on the force-free-field extrapolation and providing the code used to carry out the extrapolations described in Chapter 4.

Some of the observations described within this thesis were obtained as part of a SOHO Joint Observing Programme (JOP). This would not have been possible without the help of numerous people. These include Richard Harrison. Andrzej Fludra, Joe Gurman, Julia Saba, Kuen Ko, John Raymond, Barry LaBonte, Spiros Patsourakos, Charles Kankelbourg, Brian Handy, Hugh Hudson and all the members of the Yohkoh Operations Centre and the SOHO/SOC.

I would like to thank PPARC for financial support during this project and for additional financial assistance allowing me to attend Space Weather Week, 1999 Boulder, Colorado, the NATO ASI on Storms and Space Weather Hazards, Crete, 2000 and a weeks Yohkoh Operations ("Tohban") experience at ISAS, Japan. Also thanks to Eamonn Daly of ESA's Space Environment and Effects Analysis Section for an ESA bursary towards attendance of the NATO ASI.

Last but definitely not least, thanks to my family for their eternal support. This thesis is dedicated to you. Thanks also to Neale for always being ready to listen and being incredibly supportive throughout.

Thanks

References

Aly A. A., *How Much Energy can be Stored in a Three-Dimensional Force-Free Magnetic Field?*, 1991, Astrophys. J. Lett., **375**, L61

Andrews M. D. and Howard R. A., *LASCO Observations of a Streamer CME on 13-14 August 1997*, 1999, in *SolarWind 9*, Ed. S. R. Habbal, R. Esser, J. V. Hollweg and P. A. Isenberg, AIP Conf. Proc. **471**, 629

Antiochos S. K., *The Magnetic Topology of Solar Eruptions,* 1998, Astrophys. J. Lett., **502**, L181

Antiochos S. K., DeVore C. R. and Klimchuk J. A., *A Model for Coronal Mass Ejections*, 1999, Astrophys. J., **510**, 1, 485

Anzer U., *Structure and Equilibrium of Prominences*, 1989, in 'Dynamics and Structure of Quiescent Solar Prominences', Dordrecht, Kluwer Academic Pub., 143

Athay R. G., *The Solar Chromosphere and Corona: Quiet Sun*, 1976, Dordrecht, Reidel

Athay R. G. and Moreton G. E., *Impulsive Phenomena of the Solar Atmosphere I: Some Optical Events Associated with Flares Showing Explosive Phase,* 1961, Astrophys. J., **133**, 935

Aurass H., Vrsnak B., Hofmann A. and Rudzjak V., *Flares in Coronal Structures – a Case Study*, 1999, Sol. Phys., **190**, 1/2, 267

Babcock H. W., *The Topology of the Sun's Magnetic Field and the 22-Year Cycle*, 1961, Astrophys. J., **133**, 572.

van Ballegooijen A. A., *Photospheric Motions as a Source of Twist in Coronal Magnetic fields*, 1999, in *Magnetic Helicity in Space and Laboratory Plasmas*, Geophys. Monogr. Ser., Vol. 111, Ed. M. R. Brown, R. C. Canfield and A. A. Pevtsov, 213

Berdichevsky D., Bougeret J.-L., Delaboudiniere J.-P., Fox N., Kaiser M., Lepping R., Michels D., Plunkett S., Reames D., Reiner M., Richardson I., Rostoker G., Steinberg J., Thompson B. and von Rosenvinge T., *Evidence for Multiple Ejecta: April 7-11, 1997, ISTP Sun-Earth Connection Event*, 1998, Geophys. Res. Lett., **25**, 14, 2473

Berger M. A., *Rigorous New Limits on Magnetic Helicity Dissipation in the Solar Corona*, 1984, Geophys. Astrophys. Fluid Dynamics, **30**, 79

Berger M. A., *Magnetic Helicity in Space Physics*, 1999, in *Magnetic Helicity in Space and Laboratory Physics*, Geophys Monogr. Ser., Vol. 111, Ed. M. R. Brown, R. C. Canfield and A. A. Pevtsov, 1

Bothmer V. and Schwenn R., *Eruptive Prominences as Sources of Magnetic Clouds in the Solar Wind*, 1994, Sp. Sci. Rev., **70**, 215

Brown, D. S., *Three Dimensional Topology of Solar Coronal Magnetic Fields*, 1999, PhD Thesis, University of St Andrews.

Brueckner G. E., Howard R. A., Koomen M. J., Korendyke C. M., Michels D. J., Moses J. D., Socker D. G., Dere K. P., Lamy P. L., Llebaria A., Bout M. V., Schwenn R., Simnett G. M., Bedford D. K. and Eyles C. J., *The Large Angle Spectroscopic Coronagraph (LASCO)*, 1995, Sol. Phys., **162**, 357

Burlaga L. F., Sittler E., Mariani F. and Schwenn R., *Magnetic Loop Behind and Interplanetary Shock: Voyager, Helios and IMP-8 Observations*, 1981, J. Geophys. Res., **86**, 6673

Canfield R. C., 1999, Private Communication. (See Appendix A for additional detail)

Canfield R. C., Pevtsov A. A. and McClymont A. N., *On the Subphotospheric Origin of Coronal Electric Currents,* 1997a, Astrophys. J., **481**, 973

Canfield R. C., Pevtsov A. A. and McClymont A. N., *Magnetic Chirality and Coronal Reconnection*, 1997b, in *Magnetic Reconnection in the Solar Atmosphere*, ASP Conf. Series Vol. 111, Ed. R. D. Bentley and J. T. Mariska, 341

Canfield R. C., Hudson H. S. and McKenzie D. E., *Sigmoidal Morphology and Eruptive Solar Activity*, 1999, Geophys. Res. Lett., **26**, 6, 627

Canfield R. C. and Pevtsov A. A., *Helicity and Reconnection in the Solar Corona: Observations*, 1999, in *Magnetic Helicity in Space and Laboratory Plasmas*, Geophys. Monogr. Ser., Vol. 111, Ed. M. R. Brown, R. C. Canfield and A. A. Pevtsov, 197

Canfield R. C., Hudson H. S. and Pevtsov A. A., *Sigmoids as Precursors of Solar Eruptions*, 2001, IEEE Transactions on Plasma Science, **28**, 1786.

Carmichael H., *A Process for Flares,* 1964, in AAS-NASA Symp. *Physics of Solar Flares*, Ed. W. N. Hess (NASA SP-50: Washington), 451

Chase R. C., Kreiger A S., Svestka Z. and Vaiana G. S., *SKYLAB Observations of X-ray loops Connecting Separate Active Regions*, 1976, in *Space Research XVI; Proceedings of the Open Meetings of Working Groups on Physical Sciences and Symposium and Workshop on Results from Coordinated Upper Atmosphere Measurement Programs*, Akademie-Verlag GmBH, 917

Chen J., Howard R. A., Brueckner G. E., Santoro R., Krall J., Paswaters S. E., St. Cyr O. C., Schwenn R., Lamy P. and Simnett G. M., *Evidence of an Erupting Magnetic Flux Rope: LASCO Coronal Mass Ejection of 1997 April 13*, 1997, Astrophys. J., **490**, L191

Delaboudiniere J.-P., Artzner G. E., Brunaud J., Gabriel A. H., Hochedez J. F., Millier F., Song X. Y., Au B., Dere K. P. Howard R. A., Kreplin R., Michels, D. J., Moses J. D., Defise J. M., Jamar C., Rochus P., Chauvineau J. P., Marioge J. P., Catura R. C., Lemen J. R., Shing L., Stern R. A., Gurman J. B., Neupert W.M., Maucherat A., Clette F., Cugnon P. and van Dessel E. L., *The Extreme-Ultraviolet Imaging Telescope for the SOHO Mission*, 1995, Sol. Phys., **162**, 291

Demoulin P., Mandrini C.H., van Driel-Gesztelyi L., Plunkett S., Thompson B., Khovari Zs., Aulanier G. and Young A., *What is the source of magnetic helicity shed by CMEs? The long-term helicity budget of AR 7978*, 2002, Astron. Astrophys., **382**, 650

Dere K. P., Brueckner G. E., Howard R. A., Michels D. J. and Delaboudiniere J.-P., *LASCO and EIT Observations of Helical Structure in Coronal Mass Ejections,* 1999, Astrophys. J., **516**, 1, 465

DeVore C. R., *Magnetic Helicity Generation by Solar Differential Rotation*, 2000, Astrophys. J., **539**, 2, 944

Domingo V., Fleck B. and Poland A. I., *The SOHO Mission: An Overview*, 1995, Sol. Phys., **162**, 1.

van Driel-Gesztelyi L., Csepura G., Schmeider B., Malherbe J.-M. and Metcalf T., *Evolution of a Delta Group in the Photosphere and Corona*, 1997, Sol. Phys., **172**, 151

van Driel-Gesztelyi L., Mandrini C. H., Thompson B. J., Plunkett S., Aulanier G., Demoulin P., Schmeider B. and DeForest C., *Long-Term Magnetic Evolution of an AR and its CME Activity,* 1999, in *3rd Advances in Solar Physics*, ASP Conf. Series, 184, 302-306, Ed. B. Schmeider, A. Hofmann and J. Staude

van Driel-Gesztelyi L., Manoharan P.K., Demoulin P., Aulanier G., Mandrini C.H., Lopez-Fuentes M., Schmeider B., Orlando S., Thompson B. and Plunkett S. *Initiation of CMEs: the role of magnetic twist*, 2000, J. Astron. Sol. Terr. Phys., **62**/16, 1437

Edlén B., *The Interpretation of the Emission lines in the spectrum of the Solar Corona. With 6 Figures*, 1942, Magazine for Astrophysics, **22**, 30.

Emonet T. and Moreno-Insertis F., *the Physics of Twisted Magnetic Tubes Rising in a Stratified Medium: Two Dimensional Results*, 1998, Astrophys. J., **492**, 804

Falconer D. A., Moore R. L. and Gary G. A., *Prediction of Coronal Mass Ejections from Vector Magnetograms: Quantitative Measures as Predictors*, 2002, Astrophys. J., 569, 2, 1016

Farnik F., Karlicky M. and Svestka Z., *Long transequatorial Interconnecting Loops of the New Solar Cycle*, 1999, Sol. Phys., **187**, 1, 33

Feldman U., Laming J. M. and Doschek G. A., *The Correlation of Solar Flare Temperature and Emission Measure Extrapolated to the Case of Stellar Flares*, 1995, Astrophys. J., **451**, L79

Feynman J. and Martin S. F., *The Initiation of Coronal Mass Ejections by Newly Emerging Flux*, 1995, J. Geophys. Res., **100,** 3355

Foley C. R., Patsourakos S., Culhane J. L. and MacKay D., *Solar cycle variation of the temperature structure within the cores of coronal streamers*, 2002, Astron. Astrophys., **381**,1049

Forbes T. G. and Acton L. W., *Reconnection and Field Line Shrinkage in Solar Flares*, 1996, Astrophys. J., **459**, 330

Gabriel A. H., *A magnetic model of the solar transition region,* 1976, Roy. Soc. Phil. Trans., Ser. A, **281**, 339

Gibson S. E., Mason H. E., Pike C. D. and Young P. R., *Searching for Sigmoids in SOHO/CDS,* 1999, in *Plasma Dynamics and Diagnostics in the Solar Transition Region and Corona*, the 8th SOHO workshop, SP-446, 331

Gibson S. E., Fletcher L., Del Zanna G., Pike C. D., Mason H. E., Mandrini C. H., Demoulin P., Gilbert H., Burkepile J., Holzer T., Alexander D., Liu Y., Nitta N., Qiu J., Schmeider B. and Thompson B. J., *The Structure and Evolution of a Sigmoidal Active Region*, 2002, Astrophys. J., **574**, 2, 1021

Gilbert H. R., Holzer T. E., Burkepile J. T. and Hundhausen A. J., *Active and Eruptive Prominences and Their Relationship to Coronal Mass Ejections*, 2000, Astrophys. J., **537**, 1, 503

Gosling J. T., Birn J. and Hesse M., *Three-Dimensional Magnetic Reconnection and the Magnetic Topology of Corona Mass Ejection Events*, 1995, Geophys. Res. Lett. **22**, 869

Gosling J. T., *The Role of Reconnection in the Formation of Flux Ropes in the Solar Wind*, 1999, in *Magnetic Helicity in Space and Laboratory Plasmas*, Geophys. Monogr. Ser., Vol. 111, Ed. M. R. Brown, R. C. Canfield and A. A. Pevtsov, 205

Hara H., Tsuneta S., Acton L. W., Bruner M. E., Lemen J. R. and Ogawara Y., *Temperatures of Coronal Holes Observed with the Yohkoh/SXT*, 1994, Pub. Astro. Soc. Jap., **46**, 493

Hara H., *Structures and Heating Mechanisms of the Solar Corona*, 1996, PhD Thesis Natl. Astro. Obs. Japan

Harrison R. A., *Solar Coronal Mass Ejections and Flares*, 1986, Astron. Astrophys., **162**, 1-2, 283

Harrison R. A., *The Source Regions of Solar Coronal Mass Ejections*, 1990, Sol. Phys., **126**, 185

Harrison R. A., *Coronal Transients and their Relation to Solar Flares,* 1991, Adv. Sp. Res., **11**, 1, 25

Harrison R. A., Sawyer E. C., Carter M. K., Cruise A. M., Cutler R. M., Fludra A., Hayes R. W., Kent B. J., Lang J., Parker D. J., Payne J., Pike C. D., Peskett S. C., Richards A. G., Culhane J. L., Norman K., Breeveld A. A., Breeveld E. R., Al Janabi, K. F., McCalden A. J., Parkinson J. H., Self D. G., Thomas P. D., Poland A. I., Thomas R. J., Thompson W. T., Kjejdseth-Moe O., Brekke P., Karud J., Maltby P., Aschenbach B., Braüninger H., Kühne M., Hollandt J., Siegmund O. H. W., Huber M. C. E., Gabriel A. H., Mason H. E. and Bromage B. J. I., *The Coronal Diagnostic Spectrometer for the Solar and Heliospheric Observatory*, 1995, Sol. Phys., **162**, 233

Harrison R. A. and Lyons M., *A Spectroscopic Study of Coronal Dimming Associated with a Coronal Mass Ejection*, 2000, Astron. Astrophys., **358**, 1097

Hirayama T., *Theoretical Model of Flares and Prominences I: Evaporating Flare Model*, 1974, Sol. Phys., **34**, 323

Hood A. W. and Priest E. R., *Kink Instability of Solar Coronal Loops as the Cause of Solar Flares*, 1979, Sol. Phys., **64**, 303

Howard R. A., Michels D. J., Sheeley N. R. Jr. and Koomen M. J., *The Observation of a Coronal Transient Directed at Earth*, 1982, Astrophys. J., **263**, L101

Howard R. A., Sheeley N. R. Jr., Michels D. J. and Koomen M. J., *Coronal Mass Ejections – 1979-1981*, 1985, J. Geophys. Res., **90**, 8173

Howard R. A., Moses J. D. and Socker D. G., *Sun Earth Connection Coronal and Heliospheric Investigation*, 2000, Presented at 45th SPIE International Symposium on Optical Science and Technology in the Conference on Instrumentation for UV/EUV Astronomy and Solar Missions, August 2000 (available via http://projects.nrl.navy.mil/secchi/images/SPIE_4139-26.pdf).

Hudson H. S., *Solar Flares, Microflares, Nanoflares and Coronal Heating*, 1991, Sol. Phys., **133**, 357

Hudson H. S. and Webb D. F., *Soft X-Ray Signatures of Coronal Ejections*, 1997, in *Coronal Mass Ejections*, Geophys. Monogr. Ser., Vol. 99, Ed. N. Crooker, J.-A. Joselyn and J. Feynman, 27

Hudson H. S., Lemen J. R., St. Cyr O. C., Sterling A. C. and Webb D. F., *X-ray Changes During Halo CMEs*, 1998, Geophys. Res. Lett., **25**, 14, 2481

Hudson H. S., Acton L. W., Harvey K. L. and McKenzie D. E., *A Stable Filament Cavity with a Hot Core*, 1999, Astrophys. J., **513**, 1, L83

Hudson H. S. and Cliver E. W., *Observing coronal mass ejections without coronagraphs,* 2001, J. Geophys. Res., **106**, 25199

Hundhausen A. J., *Sizes and Locations of Coronal Mass Ejections – SMM Observations from 1980 and 1984-1989*, 1993, J. Geophys. Res., **98**, 13,177

Hundhausen A., *Coronal Mass Ejections*, 1999, In *The Many Faces of the Sun: A Summary of the Results from NASA's Solar Maximum Mission.* ed. K. T. Strong, J. L. R. Saba, B. M. Haisch and J. T. Schmelz, New York, Springer, 143

Illing R. M. E. and Hundhausen A. J., *Observation of a Coronal Transient from 1.2 to 6 Solar Radii*, 1985, J. Geophys. Res., **90**, 275

Joselyn J. A. and McIntosh P. S., *Disappearing Solar Filaments – A Useful Predictor of Geomagnetic Activity*, 1981, J. Geophys. Res., **86**, 4555

Kano R., *The Time Evolution of X-Ray Structure during Filament Eruption,* 1994, in *X-Ray Solar Physics from Yohkoh*, Tokyo: Universal Academy Press, Ed. Y. Uchida, T. Watanabe, K. Shibata and H. S. Hudson, 273

Khan J. I. and Hudson H. S., *Homologous Sudden Disappearances of Transequatorial Interconnecting Loops in the Solar Corona*, 2000, Geophys. Res. Lett., **27**, 8, 1083

Kippenhahn R. and Schlüter A., *Theory for Solar Filaments, with 7 Tables*, 1957, Magazine for Astrophysics, **43**, 36

Klassen A., Aurass H., Mann G., and Thompson B. J., *Catalogue of the 1997 SOHO-EIT Coronal Transient Waves and Associated Type II Radio Burst Spectra*, 2000, Astron. Astrophys. S., **141**, 357

Kopp R. A. and Pneuman G. W., *Magnetic Reconnection in the Corona and the Loop Prominence Phenomenon*, 1976, Sol. Phys., **50**, 85

Kumar A. and Rust D. M., *Interplanetary Magnetic Clouds, Helicity Conservation and Current-Core Flux-Ropes*, 1996, J. Geophys. Res., **101**, 15,667

Kuperus M. and Raadu M. A., *The Support of Prominences Formed in Neutral Sheets*, 1974, Astron. Astrophys., **31**, 189

Lawrence G. R., 2002, Private Communication

Lawrence G. R. and Young C. A., *A Study of Measurement Errors in Tracking Coronal Mass Ejections Using Coronagraph Data,* 2001, AGU Spring Meeting 2001, abstract #SH22C-02

Leka K. D., Canfield R. C., McClymont A. N. and van Driel-Gesztelyi L., *Evidence for Current-Carrying Emerging Flux*, 1996, Astrophys. J., **462**, 547

Low, B. C., *Magnetohydrodynamic Processes in the Solar Corona: Flares, Coronal Mass Ejections and Helicity,* 1994, Plasma Phys., **1**, 1684

Low, B. C., *Solar Activity in the Corona*, 1996, Sol. Phys., **167**, 217

Low B. C., *The Role of Coronal Mass Ejections in Solar Activity,* 1997 in *Coronal Mass Ejections*, Geophys. Monogr. Ser., Vol. 99, Ed. N. Crooker, J.-A. Joselyn and J. Feynman, 39

MacQueen R. M., Eddy J. A., Gosling J. T., Hildner E., Munro R. H., Newkirk G. A. Jr. and Poland A. I., Ross C. L., *The Outer Solar Corona as Observed from Skylab: Preliminary Results*, 1974, Astrophys. J. Lett., **187**, L85

MacQueen R. M., Csoeke-Poeckh A., Hildner E., House L., Reynolds R., Stanger A., Tepoel H. and Wagner W., *The High Altitude Observatory Coronagraph/ Polarimeter on the Solar Maximum Mission*, 1980, Sol. Phys., **65**, 91

Manoharan P. K., van Driel-Gesztelyi L., Pick M. and Demoulin P., *Evidence for Large Scale Solar Magnetic Reconnection from Radio and X-ray Measurements*, 1996, Astrophys. J. Lett., **468**, L73

Martin S. F., *Conditions for the formation and Maintenance of Filaments – (Invited Review)*, 1998, Sol. Phys., **182**, 1, 107

Masuda S., Kosugi T., Hara H., Tsuneta S. and Ogawara Y., *A Loop-top Hard X-ray source in a Compact Solar Flare as Evidence for Magnetic Reconnection*, 1994, Nature, **371**, No 6497, 495

Maunder E. W., *The Sun and Sun-Spots, 1820-1920*, 1922, Mon. Not. Roy. Astro. Soc., **82**, 534

Meunier N., *Fractal Analysis of Michelson Doppler Imager Magnetograms: A Contribution to the Study of the Formation of Solar Active Regions,* 1999, Astrophys. J, **515**, 801

Miller J. A., Cargill P. J., Emslie A. G., Holman G. D., Dennis B. R., LaRosa T. N., Winglee R. M., Benka S. G. and Tsuneta S., *Critical Issues for Understanding Particle Acceleration in Impulsive Solar Flares,* 1997, J. Geophys. Res., **102**, 14,631

Moore R. L., Sterling A. S., Hudson H. S. and Lemen J. R., *Onset of the Magnetic Explosion in Solar Flares and Coronal Mass Ejections*, 2001, Astrophys. J., **552**, 2, 833

Moreno-Insertis F., *Nonlinear Time-Evolution of Kink-Unstable Magnetic Flux Tubes in the Convective Zone of the Sun*, 1986, Sol. Phys., **166**, 1/2, 291

Moreton G. E., *Hα Observations of Flare-Initiated Disturbances with Velocities ~1000km/sec*, 1960, Astrophys. J., **65**, 495

Munro R. H., Gosling J. T., Hildner E., MacQueen R. M., Poland A. I. and Ross C. L., *The Association of Coronal Mass Ejection Transients with Other Forms of Solar Activity*, 1979, Sol. Phys., **61**, 201

Neupert W. M., *Comparison of Solar X-ray Line Emission with Microwave Emission During Flares*, 1968, Astrophys. J. Lett., **153**, L59

Newton H. W. and Nunn M. L., *The Sun's Rotation derives from Sunspots 1934-1944 and Additional Results*, 1951, Mon. Not. Roy. Astro. Soc., **111**, 413

Ogawara Y., Takano T., Kosugi T., Tsuneta S., Watanabe T., Kondo I. and Uchida Y., *The Solar-A Mission – An Overview*, 1991, Sol. Phys., **136**, 1

Parker E. N., *Sweet's Mechanism for Merging Magnetic Fields in Conducting Fluids,* 1957, J. Geophys. Res., **62**, 509

Parker E. N., *Sudden Expansion of the Corona Following a Large Solar Flare and the Attendant Magnetic Field and Cosmic Ray Effects,* 1961, Astrophys. J., **133**, 1014

Parker E. N., *Nanoflares and the Solar X-ray Corona*, 1988, Astrophys. J., **330**, 474

Petschek, H. E., *Magnetic Field Annihilation*, 1964, in AAS-NASA Symp. on *The Physics of Solar Flares*, NSA SP-50, 425

Pevtsov A. A., Canfield R. C. and Metcalf T. R., *Latitudinal Variation of Helicity of Photospheric Magnetic Fields*, 1995, Astrophys. J. Lett., **440**, 2, L109

Pevtsov A. A., Canfield R. C. and Zirin H., *Reconnection and Helicity in a Solar Flare*, 1996, Astrophys. J., **473**, 533

Pevtsov A. A., Canfield R. C. and McClymont A. N., *On the Subphotospheric Origin of Coronal Electric Currents*, 1997, Astrophys. J., **481**, 373

Pevtsov A. A., *Transequatorial Loops in the Solar Corona*, 2000, Astrophys. J., **531**, 533

Phillips K. J. H., *Guide to the Sun*, 1992, Cam. Univ. Press.

Plunkett S. P., Thompson B. J., Howard R. A., Michels D. J., St. Cyr O. C., Tappin S. J., Schwenn R. and Lamy P. L., *LASCO Observations of an Earth Directed Coronal Mass Ejection on May 12, 1997*, 1998, Geophys. Res. Lett., **25**, 14, 2477

Plunkett S. P., Vourlidas A., Simberova S., Karlicky M., Kotrc P., Heinzel P., Kupryakov Y. A., Guo W. P. and Wu S. T., *Simultaneous SOHO and Ground-Based Observations of a Large Eruptive Prominence and Coronal Mass Ejection*, 2000, Sol. Phys., **194**, 371

Porter L. J. and Klimchuk J. A., *Soft X-ray Loops and Coronal Heating*, 1995, Astrophys. J., **454**, 499

Priest E. R., *Solar Magnetohydrodynamics*, 1982, Dordrecht, D. Reidel

Priest E. R., *Solar Flare Theory and the Status of solar Flare Understanding,* 2000, in *High Energy Solar Physics: Anticipating HESSI*, ASP Conference Series.

Rust D. M., *Spawning and Shedding Helical Magnetic Fields in the Solar Atmosphere*, 1994, Geophys. Res. Lett., **21**, 4, 241

Rust D. M. and Kumar A., *Evidence for Helically Kinked Magnetic Flux Ropes in Solar Eruptions*, 1996, Astrophys. J. Lett., **464**, L199

Rust D. M., *Helicity Conservation*, 1997, in *Coronal Mass Ejections*, Geophys. Monogr. Ser., Vol. 99, Ed. N. Crooker, J.-A. Joselyn, J. Feynman, 119

Sakurai T., Shibata K., Ichimoto K., Tsuneta S. and Acton L. W., *Flare-related Relaxation of Magnetic Shear as observed with the Soft X-ray Telescope of Yohkoh and with Vector Magnetographs*, 1992, Pub. Astro. Soc. Jap., **44**, 5, L123

Scherrer P. H., Bogart R. S., Bush R. I., Hoeksema J. T., Kosovichev A. G., Schou J., Rosenberg W., Springer L., Tarbell T. D., Title A., Wolfson C. J., Zayer I., Akin D., Carvalho B., Chevalier R., Duncan D., Edwards C., Katz N., Levay M., Lindgren R., Mathur D., Morrison S., Pope T., Rehse R. and Torgerson D., *The Solar Oscillations Investigation – Michelson Doppler Imager*, 1995, Sol. Phys., **162**, 129

Schrijver C. J., Title A. M., Berger T. E., Fletcher L., Hurlburt N. E., Nightingale R. W., Shine R. A., Tarbell T. D., Wolfson J., Golub L., Bookbinder J. A., Deluca E. E., McMullen R. A., Warren H. P., Kankelborg C. C., Handy B. N. and de Pontieu B., *A new view of the solar outer atmosphere by the Transition Region and Coronal Explorer*, 1999, Sol. Phys., **187**, 2, 261

Sheeley N. R. Jr., Howard R. A., Koomen M. J., Michels D. J., Harvey K. and Harvey J., *Observations of Coronal Structure During Solar Maximum*,1982, Sp. Sci. Rev, **33**, 219

Sheeley N. R. Jr., Walters J. H., Wang Y.-M. and Howard R. A., *Continuous Tracking of Coronal Outflows: Two Kinds of Coronal Mass Ejections*, 1999, J. Geophys. Res., **104**, 24,739

Shibata K., *New Observational Facts about Solar Flares from Yohkoh Studies – Evidence of Magnetic Reconnection and a Unified Model of Flares*, 1996, Adv. Sp. Res., **17**, 4/5, 9

Shibata K., *Reconnection Models of Flares*, 1999, in Nobeyama Symposium, Oct, 1998 Ed. T. S Bastian, N. Gopalswamy and K. Shibasaki, NRO Report No. 479, 381

Srivastava N., Schwenn R., Inhester B., Martin S. F. and Hanaoka Y., *Factors Related to the Origin of a Gradual Coronal Mass Ejection Associated with an Eruptive Prominence on 1998 June 21-22*, 2000, Astrophys. J., **534**, 1, 468

Sterling A. C., and Hudson H. S., *Yohkoh/SXT Observations of X-Ray "Dimming" Associated with a Halo Coronal Mass Ejection*, 1997, Astrophys. J. Lett., **491**, L55

Sterling A. C., Hudson H. S., Thompson B. J. and Zarro D. M., *Yohkoh/SXT and SOHO/EIT Observations of Sigmoid-to-Arcade Evolution of Structures Associated with Halo Coronal Mass Ejections*, 2000, Astrophys. J, **532**, 1, 628

Sterling A. C. and Moore R. L., *Internal and External Reconnection in a Series of Homologous Solar Flares*, 2001, J. Geophys. Res., **106**, 25, 227

Sturrock P. A., *A Model of Solar Flares,* 1968, in IAU Symposium No. 35, *Structure and Development of Active Regions*, Ed. K. O. Kiepenheuer, Dordrecht, Reidel, 471

Sturrock P. A., *Maximum Energy of Semi-Infinite Magnetic Field Configurations*, 1991, Astrophys. J., 380, 655

Sturrock P. A. and Woodbury E. T., *Force-Free Magnetic Fields and Solar Filaments*, 1967, in Proc. Int. School of Physics Enrico Fermi, *Plasma Astrophysics*, Ed. P. A. Sturrock, New York: Academic, 155

Sudan R. N. and Spicer D. S., *Are the Fundamental Assumptions of Conventional Solar Flare Theory Valid?,* 1996, Comments Plasma Phys. Controlled Fusion, 17, 2, 77

Svestka Z., Kreiger A. S., Chase R. C. and Howard R., *Transequatorial Loops Interconnecting McMath Regions 12472 and 12474*, 1977, Sol. Phys., **52**, 69

Svestka Z. and Howard R., *Transient Brightenings if Interconnecting Loops II – Dynamics of the Brightened Loops*, 1981, Sol. Phys., **71**, 349

Sweet P. A., *The Production of High Energy Particles in Solar Flares*, 1958, Nuovo Ciemto Suppl., **8**, 188

Tandberg-Hanssen E. A. and Emslie A. G., *The Physics of Solar Flares,* 1988, Cam. Univ. Press

Thompson B. J., Plunkett S. P., Gurman J. B., Newmark J. S., St. Cyr O. C. and Michels D. J., *SOHO/EIT Observations of an Earth-Directed Coronal Mass Ejection on May 12, 1997,* 1998, Geophys. Res. Lett., **25**, 14, 2465

Thompson B. J., Gurman J. B., Neupert W. M., Newmark J. S., Delaboudiniere, J.-P., St. Cyr O. C., Stezelberger S., Dere K. P., Howard R. A. and Michels D. J., *SOHO/EIT Observations of the 1997 April 7 Coronal Transient: Possible Evidence of Coronal Moreton Waves*, 1999, Astrophys. J. Lett., **517**, 2, L151

Thompson B. J., Cliver E. W., Nitta N., Delannee C. and Delaboudiniere J. –P., *Coronal Dimmings and Energetic CMEs in April-May 1998*, 2000, Geophys. Res. Lett., **27**, 10, 1431

Titov V. S. and Demoulin P., *Basic Topology of Twisted Magnetic Field Configurations in Solar Flares*, 1999, Astron. Astrophys., **351**, 707

Tousey R., *The Solar Corona*, 1973, Adv. Sp. Res., **13**, 713

Tsuneta S., Acton L., Bruner M., Lemen J., Brown W., Caravalho R., Catura R., Freeland S., Jurcevich B. and Owens J., *The Soft X-ray Telescope for the Solar-A Mission*, 1991, Sol. Phys., **136**, 37

Tsuneta S., Hara H., Shimizu T., Acton L. W., Strong K. T., Hudson H. S. and Ogawara Y., *Observation of a Solar Flare at the Limb with the Yohkoh Soft X-ray Telescope*, 1992, Pub. Astro. Soc. Jap., **44**, 5, L63

Tsuneta S., *Interacting Active Regions in the Solar Corona*, 1996, Astrophys. J. Lett., **456**, L63

Tsuneta S., Masuda S., Kosugi T. and Sato J., *Hot and Super-hot Plasmas Above an Impulsive Flare Loop*, 1997, Astrophys. J., **478**, 787

Uchida Y., *Propagation of Hydromagnetic Disturbances in the Solar Corona and Moreton's Wave Phenomenon*, 1968, Sol. Phys., **4**, 30

Vaiana G. S., Davis J. M., Giacconi R., Krieger A. S., Silk J. K., Timothy A. F. and Zombeck M., *X-Ray observations of Characteristic Structures and Time Variations from the Solar Corona. Preliminary Results from SKYLAB.*, 1973, Astrophys. J. Lett., **185**, L47

Wang H., Goods P. R., Denker C., Yang G., Yurchishin V., Nitta N., Gurman J. B., St. Cyr O. C. and Kosovichev A. G., *Comparison of the 1998 April 29 M6.8 and 1998 November 5 M8.4 Flares*, 2000, Astrophys. J., **536**, 2, 971

Wang T., Yan Y., Wang J., Kurokawa H. and Shibata K., *The Large Scale Coronal Field Structure and Source Region Features for a Halo CME*, 2002, Astrophys. J., **572**, 580

Warmuth A., Hanslmeier A., Messerotti M., Cacciani A., Moretti P. F. and Otruba W., *NOAA AR 8210: Evolution and Flares from Multi-band Diagnostics*, 2000, Sol. Phys., **194**, 1, 103

Webb D. F. and Hundhausen A. J., *Activity Associated with the Solar Origin of Coronal Mass Ejections*, 1987, Sol. Phys., **108**, 2, 383

Webb D. F., *Solar sources of Coronal Mass Ejections*, 1992, in *Eruptive Solar Flares* Ed. Z. Svestka, B. V. Jackson and M. E. Machado, (New York: Springer), 234

Webb D. F., Cliver E. W., Gopalswamy N., Hudson H. S. and St. Cyr O. C., *The Solar Origin of the January 1997 Coronal Mass Ejection, Magnetic Cloud and Geomagnetic Storm*, 1998, Geophys. Res. Lett., **25**, 15, 2469

Wills-Davey M. J. and Thompson B. J., *Observations of a Propagating Disturbance in TRACE*, 1999, Sol. Phys., **190**, 467

Wood B. E., Karovska M., Chen J., Brueckner G. E., Cook J. W. and Howard R. A., *Comparison of Two Coronal Mass Ejections Observed by EIT and LASCO with a model of an Erupting Magnetic Flux Rope*, 1999, Astrophys. J., **512**, 1, 484

Yokoyama T. and Shibata K., *Magnetic Reconnection as the Origin of X-ray Jets and H-alpha Surges on the Sun*, 1995, Nature, **375**, 42

Zarro D. M., Sterling A. C., Thompson B. J., Hudson H. S. and Nitta N., *SOHO/EIT Observations of Extreme-Ultraviolet "Dimming" Associated with a Halo Coronal Mass Ejection*, 1999, Astrophys. J., **520**, 2, L139

Glossary:

Active Region.

This is a collective term given to bipolar regions seen in magnetograms of the solar disk. The term can be used to refer to emerging flux groups, sunspot groups and decaying spot groups. Active regions are confined to latitudes between about 35° north and south and extend tens of thousands of kilometres into the solar atmosphere above sunspots. They have a distinctive appearance in the transition region, corona and chromosphere where enhanced emission is observed over a broad spectral range. SGD defines an active region only if sunspots are present or if it gives rise to a flare. This is the NOAA classification referred to in this thesis.

Alfvén speed

The Alfvén speed is a fundamental parameter of MHD plasmas. An Alfvén wave (travelling at the Alfvén speed) will not change the plasma density, pressure or field magnitude. It is characterised by oscillating perturbations of the magnetic field, the electric field, the plasma velocity and the current density. Theory indicates that reconnected field lines will move away from the reconnection site at the Alfvén speed.

Cadence

The cadence of an observation sequence is defined as the time interval between successive observations.

Coronal Mass Ejection (CME)

CMEs are eruptions of magnetised plasma from the Sun seen as bright features expanding outwards from the corona in coronagraph images. The simplest form has 3 parts: (1) bright outer shell encompassing (2) a dark cavity and (3) embedded prominence material. CMEs are ejected from the Sun with speeds of up to 2000 kms^{-1}. A typical CME mass estimate is 10^{15} g.

Cusp

Cusp shaped features are thought to arise following reconnection during a solar flare. High energy particles spiral downwards along newly reconnected field lines to the chromosphere. Here they transfer energy to the chromospheric material causing heating. This drives material upwards along the reconnected field lines where it emits thermally at soft X-ray temperatures, leading to a cusp-shaped appearance.

Dark Current

Background counts in a CCD image caused by the creation of unwanted electron-hole pairs by thermal radiation from the instrument (thermal noise). Operation at low temperatures thus reduces dark current.

Emission Measure

A measure of the amount of emitting material contained within a specific volume. $EM=\int n_e^2(V)dV$. Where n_e is the electron/proton density for an ionised plasma. Emission measure is defined in this thesis as emission measure along line-of-sight, thus the above expression becomes: $EM_{los}=\int n_e^2(l)dl$.

Emissivity

The emissivity of a spectral line, also known as the contribution function or G(T), is the collective name given to the temperature dependent terms contributing to the line intensity. The emissivity thus describes the temperature dependence of the line's intensity.

Filament

Filaments appear in Hα images of the chromosphere as long dark channels of material an order of magnitude denser than the surrounding corona at approximately $10^{11\text{-}12}$ cm^{-3}. This material is suspended in the corona above a neutral line by the action of surrounding magnetic fields although the exact nature of this suspension and the origin of the prominence material is still a subject of debate.

Filament Layer Eruption

A filament layer eruption takes place when a filament partially erupts, leading to the formation of bright Hα ribbons being observed at the same time as the dark filament. In this case, the filament does not disappear as a result of activity in the region.

Flat Field Correction

The correction applied to telescope images to account for systematic errors caused by instrumental effects such as CCD damage.

Flux Breakout Model

Developed by Antiochos, DeVore and Klimchuk [1998], the flux breakout model considers that the shear buildup within the erupting region is concentrated near a neutral line, such that the stressed field near the neutral line provides the free energy and upwards push. In contrast, the overlying field will provide a downward pull in order to restrain expansion of the core field. The key feature of this model is that additional, nearby flux systems are present making it possible for overlying flux to reconnect with these nearby systems. This reconnection transfers the overlying unsheared flux to neighbouring systems and thus removes, or reduces, the overlying restraining pull. Therefore, reconnection allows the underlying field to "break out" to infinity without opening the overlying field and thus violating the Aly-Sturrock open field energy limit [Aly, 1991, Sturrock, 1991]

Flux tube/rope

Flux rope is the name given to a twisted flux tube. Sigmoids are referred to as twisted flux tubes or flux ropes.

Forbidden Transitions

Term given to radiative atomic transitions that break the normal transition rules e.g. a transition between two 3p states of an atom. Such transitions are observed in the solar corona as a result of the low densities. In this scenario, the usually high probability of collisional de-excitation is greatly reduced and the excited state can persist for many hours. Spectral lines originating from such transitions can be used, in combination with other lines, for density diagnostics due to the variation of the intensity of these lines with the collisional de-excitation rate.

Fraunhöfer Lines

This term refers to absorption lines in the solar visible spectrum first catalogued by Josef van Fraunhöfer.

Frozen-in-flux

Most coronal structures are assumed to be in the perfectly conducting limit. In this case, the process of diffusion can be ignored and magnetic field lines will behave as if they move with the plasma. The frozen in flux condition implies that all particles initially tied to a flux tube will remain linked along that flux tube unless another process, such as reconnection, acts to change the field line connectivity.

Glancing Incidence

Normal focussing techniques cannot be used to detect very short wavelength radiation with energies of 0.1 keV and above. In the case of soft X-ray radiation 0.1-10 keV, optical elements making use of the principle of total external reflection are used to bring the radiation to a focus. Reflection from an X-ray mirror surface may take place at angles smaller than a "critical angle" of a few degrees. The critical angle is determined by the wavelength of the incoming radiation and the atomic number (Z) of the mirror coating. Higher energy radiation will lead to a smaller critical angle.

Hα

This term refers to the first transition of the Hydrogen Balmer series: N=3 to N=2. This transition emits radiation centred at a wavelength of 6563 Å. Hα is partly formed in the chromosphere, thus Hα images of the Sun provide information about the structure of the chromosphere. Prominences appear dark in Hα images of the solar disk and bright when observed in emission at the limb.

Helioseismology

The technique of helioseismology is the use of solar oscillations to determine the properties of the Sun's interior. The SOHO/MDI instrument is sensitive to two principle classes of oscillation: acoustic and gravity waves. Each mode will be trapped in a particular region of the Sun and the nature of the observed oscillation will depend mainly on the nature of the Sun in that region. Acoustic waves are confined within spherical shells by upward refraction caused by the gradient in sound speed in the convection zone and downward reflection caused by the steep density gradient just beneath the photosphere. By combining information about two modes with slightly different radii of refraction but the same radius of reflection near the photosphere, it is possible to infer conditions in the narrow region between the two radii of refraction.

Helmet streamer

Helmet streamers comprise a high density dome above which open field lines extend into the corona forming the bright radial streamers seen in coronagraph images. Below the dome, a low density cavity, and often an embedded prominence, are observed in a manner analogous to the three part CME structure. This structure has also been interpreted as evidence for the existence of a magnetic flux rope in the corona prior to eruption.

Homologous

Used during this thesis in the context of solar activity, the term "homologous" refers to a sequence of events that show many similar characteristics and where the system returns to a state approximating that of its initial configuration following each event.

Long Duration Event (LDE)

The term long duration event was coined historically to describe solar flares that lasted for several hours. These flares often showed Hα ribbons and were also referred to as "2-ribbon flares". It is now thought that the same reconnection process is involved. LDEs, as distinct from impulsive flares, show evidence of cusp formation since reconnection is thought to take place over a longer period. Also the likelihood of association with CME onset is higher.

Magnetic Cloud

A magnetic cloud is defined as a transient ejection of magnetised plasma into the solar wind exhibiting relatively strong fields, a large and smooth rotation of the magnetic field direction over approximately 0.25 AU and a low proton temperature [Burlaga, 1981].

Magnetic Helicity

Magnetic helicity is defined in 3-D as the extent to which magnetic field lines wrap and coil around one another. If space is divided into a collection of flux tubes, the total helicity contains contributions from internal structure within a flux tube, such as twist and writhe, and from external relations between flux tubes, such as knotting and linking.

Moreton wave

A wave-like disturbance originating from the vicinity of a solar flare seen in Hα observations of the solar disk. Moreton waves appear as either a bright front in the Hα centreline or a dark front in the Hα wing. They are seen to form an arc with angular extent $\leq 160°$ and travel across the solar disk with speeds within the range 330-4200Kms^{-1}.

Multilayers

Multilayer coatings are applied to the reflecting surfaces of telescopes in order to capture short wavelength radiation. Best suited to detecting radiation of EUV wavelengths, this technique makes use of Bragg's law of reflection. A multilayer coating is made of several pairs of alternating layers of a high and low Z material e.g. Molybdenum and Silicon. Reflection takes place at the high Z surface whereas the low Z layers act as spacers. The width of 1 layer pair is equivalent to half the wavelength of the light to be measured.

Neutral/Inversion Line

The locus of points where the measured line-of-sight component of the photospheric magnetic field passes through zero.

Point Spread Function (PSF)

If a telescope had perfect optics, the image of a single point of light reaching the CCD plane would be identical to the original point of light. However, in most cases, this situation does not arise. The point spread function represents the illumination of the surrounding pixels that would result from imaging of a point source.

Potential field

In the potential field case, **curl B** = 0. This represents the simplest case of the force free field assumption which states that currents can only flow along field lines. In the potential field case, no currents flow.

Prominence

A prominence is the term given to filament material viewed in emission above the solar limb.

Shear

The magnetic shear of a coronal region is defined as the tendency of field lines to lie obliquely across the neutral line. A measure of the shear angle gives a measure of the magnetic non-potentiality of the region.

Sigmoid

An S- (or reverse-S) shaped feature most frequently observed in soft X-ray observations of the corona. Sigmoids also appear in EUV observations, but less frequently and are often brightest during flaring events.

Sigmoid Expansion Model

This model, proposed by van Driel-Gesztelyi et al. [2000], considers reconnection of two j-shaped loops observed in the corona. Reconnection of the outer edes of these loops occurs to create a longer helical field line and reconnection of the shorter loops below. The upper loop rises to create current sheet below and reconnection takes place, leading to the observation of flare loops.

Solar Flare:

A sudden, rapid release of magnetic energy in the solar atmosphere. During a solar flare, energy is released in various forms including particle acceleration, plasma heating, bulk acceleration of plasma and enhanced radiation fields. The amount of energy released is of the order of 10^{25} J.

Solar wind

Constant expansion of the Sun's magnetic field and coronal plasma into interplanetary space gives rise to the solar wind. The solar wind consists of high and slow speed solar wind streams. The high speed streams originate from coronal holes where unipolar magnetic field lines extend into space. Slow speed streams are thought to originate from the quiet corona. Interactions between these two types of stream leads to interplanetary shock formation and recurrent geomagnetic activity at the Earth.

Sunspot

A region where bipolar field breaks through the Sun's visible surface. See Active Region.

Thomson scattering

The process by which the energy of an electromagnetic wave is partially scattered in various directions by a free electron. The electric field of the incident wave puts the electron into oscillatory motion and the electron emits a small fraction of the incident energy as dipole radiation. The same process affects ions, but due to their larger mass, the energy scattered is negligible.

Transequatorial Loop

A coronal loop observed to connect regions of the solar corona in different hemispheres. Transequatorial loops are observed in soft X-ray and EUV observations of the corona.

Vector Magnetograph

A telescope used to measure vertical and horizontal components of the photospheric magnetic field making use of the unshifted π component of polarised radiation. c.f. line-of-sight techniques which use a combination of right and left hand polarised light to produce line-of-sight magnetic field measurements.

Vignetting

The fringe pattern formed where imaging element obscures the telescope field of view. Vignetting leads to characteristic distortion of the image.

X-point

A magnetic X-point is a 2-D representation of the theoretical site at which magnetic reconnection takes place.

Appendix A: List of Sigmoidal and Eruptive Active Regions (from Canfield, [1999]).

The following table lists the active regions classified both *sigmoidal* and *eruptive* by Canfield, Hudson and McKenzie [1999] in their study of sigmoidal morphology and eruptive solar activity. All regions were observed on the disk during 1997 and form the latter half of the Canfield, Hudson and McKenzie survey data.

Key:

LPS/A:	Loop prominence system → cusp
LPS/C:	Loop prominence system → arcade
TCH:	Formation of Transient Coronal Hole
MLSB:	Associated moving large scale brightenings
/:	Denotes information not available

Active region eruptions are defined in accordance with their NOAA active region number (Column 1), time of eruption (Column 2) and event nature (Column 3). Canfield et al classified the nature of each event in terms of four possible scenarios. These are described in the above key.

NOAA AR Number	Date and Time of apparent Eruption	Nature of Event
plage	5-Jan 15:56 UT	TCH/MLSB
8015	4-Feb 09:07 UT	LPS/C,A
8020	9-Mar 15:50 UT	LPS/C
8026	/	/
8027	/	/
8032	/	/
8038	/	/
8048	/	/

8056	/	/
8059	/	/
8064	2-Aug 07:29 UT	LPS/C
8065	25-Jul 21:27 UT	LPS/C,A
8066	29-Jul 19:13 UT	LPS/A
8066	1-Aug 21:44 UT	MLSB
8071	12-Aug 10:45 UT	LPS/C
8071	14-Aug 01:23 UT	LPS/C, A MLSB
8074	21-Aug 17:47 UT	LPS/C
8074	22-Aug 20:01 UT	LPS/C
8076	27-Aug 19:39 UT	LPS/A,C
8076	30-Aug 02:50 UT	LPS/A,C
8083	8-Sep 22:58 UT	LPS/A
8083	13-Sep 22:58UT	LPS/A
8084	15-Sep 04:30 UT	LPS/C
8085	7-Sep 19:46 UT	LPS/C
8086	13-Sep 13:38 UT	LPS/C
8088	24-Sep 05:44 UT	LPS/C
8090	5-Oct 15:30 UT	LPS/A TCH
8091	4-Oct 01:46 UT	LPS/C
8092	11-Oct 09:01 UT	LPS/A,C
8096	20-Oct 07:04 UT	LPS/A,C
8097	21-Oct 19:55 UT	LPS/A,C
8098	21-Oct 02:22 UT	LPS/C
8100	28-Oct 04:03 UT	LPS/C
8108	19-Nov 21:59 UT	LPS/C,A MLSB

Appendix B: List of Transequatorial Loop Systems 1996-1999. (from Pevtsov, [2000])

This list forms part of a comprehensive list of transequatorial loops published by Pevtsov [2000]. These dates coincide with the operation of the SOHO spacecraft and so were used as a starting point for the study described in Chapter 6. Transequatorial loops marked with a star (*) occurred during the period of 1998 when SOHO was non-operational and so were not included in the survey described in Chapter 6. Examples marked with a (♠) appeared too faint in Yohkoh/SXT data to allow study of morphology changes in association with CME onset.

Number (from Pevtsov list)	**Date & Time (Clearest observation)**	**NOAA AR (North)**	**NOAA AR (South)**
63...	1996 Feb 02 00:28:03 UT	None	None
64...	1996 Dec 18 18:53:34 UT	8004	None
65...	1997 Jan 31 09:40:05 UT	8015	None
66...	1997 May 23 22:03:06 UT	8045	None
67...	1997 Sep 10 14:37:42 UT	8084	8085
68...	1997 Oct 21 23:27:11 UT	8097	None
69...	1997 Dec 28 02:55:36 UT	8126	8124
♠70...	1998 Jan 25 07:47:38 UT	None	8142

*71...	1998 Apr 14 04:32:14 UT	None	8202
72...	1998 May 03 22:54:40 UT	8214	8210
73...	1998 May 13 00:31:24 UT	none	8218
74...	1998 May 29 11:23:19 UT	8227	8228
75...	1998 Jun 16 17:40:13 UT	None	None
*76...	1998 Jul 02 03:04:11 UT	None	8258
*77...	1998 Jul 07 17:16:16 UT	8264	None
*78...	1998 Aug 15 00:23:04 UT	8299	8301
*79...	1998 Aug 29 03:21:39	None	None
*80...	1998 Sep 09 06:47:16 UT	8329	8328
*81...	1998 Sep 24 00:17:44 UT	8342	None
*82...	1998 Oct 09 16:00:32 UT	8350	8354
83...	1998 Oct 15 06:56:57 UT	8358	8355
84...	1998 Nov 04 07:02:01 UT	8375	8373
85...	1998 Nov 15 11:58:45 UT	None	8383

86...	1998 Nov 30 14:14:10 UT	8935	8393
87...	1998 Dec 05 16:34:33 UT	8402	None

Publication List

The following publications appearing in refereed journals were written by the author and are based on the results described in this thesis.

Glover A., Ranns N. D. R., Harra L. K., Matthews S. A., Culhane J. L., *The Onset and Association of CMEs with Sigmoidal Active Regions*, 2000, Geophys. Res. Lett., **27**, 13, 2161

Glover A., Harra L. K., Matthews S. A., Hori K., Culhane J. L., *Long Term Evolution of a Non-Active Region Sigmoid and its CME activity*, 2001, Astron. Astrophys., **378**, 239

Glover, A., Ranns N. D. R., Brown D. S., Harra L. K., Matthews S. A., Culhane J. L., *The Magnetic Topology of a Sigmoid*, 2002, J. Atmos. Sol. Terr. Phys., **64 (5/6)**, 497

Glover A., Harra L. K., Matthews S. A., *The Association of Transequatorial Loops in the Solar Corona with Coronal Mass Ejection Onset*, 2003, Astron. Astrophys., **400**,759